NTNU – Trondheim
Norwegian University of
Science and Technology

Ice Abrasion on Fiber Reinforced Concrete

A Study on the Effects of Various Types of Fiber and the Reliability of the Laboratory Measurements

Kristian Sætre

Civil and Environmental Engineering
Submission date: June 2014
Supervisor: Stefan Jacobsen, KT
Co-supervisor: Kjell Tore Fosså, Kværner

Norwegian University of Science and Technology
Department of Structural Engineering

Abstract

The purpose of this study has been to compare how fiber reinforced concretes, using different amounts and types of fiber, behave compared to standard offshore concretes without fiber in regard to ice abrasion. The effect of fiber addition on the freeze-thaw resistance has also been studied. Due to various observations during testing, a large part of this study has gradually come to deal with the accuracy and the reliability of the measurement equipment and methods used during these ice abrasion tests.

A literature review has been done on the effect of various parameters on the ice abrasion of concrete. Previous studies have shown the beneficial effect of the use of fiber reinforcement on both the abrasion resistance and freeze-thaw resistance of concrete. Studies have also shown that a decreased abrasion rate can be expected with an increase in flexural and compressive strength, and that the surface topography has an effect on the abrasion rate. Few studies, though, have specifically looked into the ice abrasion resistance of fiber reinforced concrete.

Ice abrasion tests have been performed at the NTNU ice abrasion laboratory on five different concrete mixes. These mixes include a B70 reference concrete and concretes with the following fiber additions: 0.5% steel fiber, 1.5% steel fiber, 1.5% polypropylene fiber and 1.5% basalt fiber. Freeze-thaw testing, according to ASTM C666 Procedure A, and air void analysis using fresh concrete, the PF-test and image analysis, have also been performed on the different concrete mixes.

It has been observed that all of the fiber additions, except for the 1.5% steel addition, have improved the ice abrasion resistance of the concrete. The ranking of these different fiber concretes in regard to their ice abrasion resistance has been found to be difficult, due to the fact that the abrasion rates are all lower than the average deviation of the measurements. Therefore, the mixes showing a better ice abrasion resistance than the others may just as well be due to the inaccuracy of the measurements than to the actual ice abrasion resistant properties of the material.

However, the abrasion rates observed in this study are generally very low. The maximum abrasion rate found is 0.011 mm/km, and the abrasion rates here are on average 11 times lower than the rates found in similar tests done by (Kirkhaug 2013). Correlations showing the positive effect on ice abrasion resistance with increasing *Surface Average Roughness* and *Root Mean Square Roughness* parameters have also been observed.

All concrete mixes failed the freeze-thaw testing requirements and the addition of fiber reinforcement has not given the expected improvement in freeze-thaw durability. Through air void analysis, it has been shown that the reason for this low concrete quality, in regard to freeze-thaw resistance, has been due to a poor air void content and structure in all of the mixes.

The accuracy of both the abrasion and roughness values has been questioned, and the average deviation of the measurements has been found to be large compared to the abrasion rates. This is due to, among other factors, the large distances between measuring points, systematical irregularities on the specimen surfaces, and an inaccuracy in the measuring equipment and procedures used. This doubt on the reliability of these results has been backed up by the poor correlation found between abrasion rates on specimens of the same product type and tested under the same conditions.

A more thorough discussion is recommended on the accuracy and reliability of the measuring equipment and procedures at the NTNU ice abrasion laboratory when testing materials with very low ice abrasion, such as those tested here. Also, further research on the effect of different fiber types and dosages on concrete ice abrasion, and the correlation between surface roughness parameters and the abrasion rate, is recommended.

Sammendrag

Hensikten med denne oppgaven har vært å studere effekten av fiberarmert betong på isabrasjon, med bruk av forskjellige typer og doseringer av fiber, sammenlignet med en standard offshore betongtype uten fiber. Effekten av å tilsette fiber i forhold til frostbestandigheten av betongen har også blitt studert. På grunn av diverse observasjoner under forsøkene, har en stor del av oppgaven etterhvert omhandlet nøyaktigheten og påliteligheten av måleutstyret og de målemetodene som har blitt brukt.

Et litteraturstudie har blitt gjort angående effekten av diverse parametere på isabrasjonen av betong. Tidligere studier har vist en positiv effekt når det gjelder bruken av fiberarmering på abrasjonsmotstanden og frostbestandigheten av betong. Tidligere studier har også vist at en minkende abrasjonsrate kan forventes med en økning i bøynings- og trykkstyrke, og at betongoverflatens topografi har en effekt på abrasjonsraten. Et fåtall studier, derimot, har sett spesifikt på isabrasjonsmotstanden til fiberarmert betong.

Isabrasjonsforsøk har blitt gjort på fem forskjellige betongblandinger ved isabrasjonslaboratoriet på NTNU. Disse blandingene inkluderer en B70 referansebetong og betonger med følgende fibertilsetninger: 0.5% stålfiber, 1.5% stålfiber, 1.5% polypropylen fiber og 1.5% basaltfiber. Fryse-tine prøver, i henhold til ASTM C666 Prosedyre A, og luftporeanalyser med bruk av fersk betong, PF-metoden og bildeanalyser, har blitt gjort på alle disse betongblandingene.

Det har blitt observert at alle fibertilsetningene, utenom tilsetningen av 1.5% stålfiber, har forbedret isabrasjonsmotstanden til betongen. Å rangere disse fiberbetongene i forhold til sine isabrasjonsmotstander er likevel vanskelig. Dette er fordi alle abrasjonsratene er lavere enn det gjennomsnittlige avviket til målingene. Således, fiberbetongene som viser bedre isabrasjonsegenskaper enn de andre kan like så godt skyldes usikkerheten i målingene enn de egentlige isabrasjonsegenskapene av materialene.

Abrasjonsratene observert i dette studiet er generelt veldig lave. Den største abrasjonsraten funnet her er på 0.011 mm/km, og abrasjonsratene her er gjennomsnittlig 11 ganger lavere enn de abrasjonsratene som er observert i lignende forsøk gjort av (Kirkhaug 2013). Korrelasjoner som viser den positive effekten på isabrasjonsmotstand med økende gjennomsnittsruhet og rotmiddelkvadratsruhet på betongoverflaten har også blitt observert.

Alle betongblandingene har mislykkes med å innfri de kravene som er satt til frostbestandighet, og tilsetningen av fiberarmering har ikke gitt den forventede forbedringen i frostbestandighet. Ved bruk av luftporeanalyser har det blitt påvist at denne manglende frostbestandigheten skyldes et dårlig poreinnhold og porestruktur i samtlige betongblandinger.

Nøyaktigheten og påliteligheten av både abrasjons- og ruhetsverdiene har, derimot, blitt lagt under tvil. Dette er på grunn av, blant annet, store avstander mellom målepunkter, systematiske uregelmessigheter på betongoverflatene, og en unøyaktighet i måleutstyret og måleprosedyrene. Denne tvilen på påliteligheten av disse resultatene har blitt underbygget av den svake korrelasjonen som er funnet mellom abrasjonsratene på prøver av samme type, som er testet under de samme forholdene.

En grundigere gjennomgang av nøyaktigheten og påliteligheten av måleutstyret og prosedyrene ved isabrasjonslaboratoriet ved NTNU er anbefalt. Videre forskning innenfor effekten av ulike fibertyper og doseringer på isabrasjon, og korrelasjonen mellom overflatetopografien og abrasjonsraten er også anbefalt.

Preface

This Master thesis was written at the Department of Structural Engineering at the Norwegian University of Science and Technology in Trondheim, during the spring of 2014. The thesis is a continuation of my project thesis from the previous semester. The purpose of this thesis, in collaboration with Kvaerner Concrete Solutions, has been to investigate the effect of fiber reinforcement and various other parameters, such as sliding velocity and surface roughness, on the ice abrasion of concrete. This is a relevant topic as offshore structures are to be built in arctic, ice-exposed sea areas in the near future. Due to various observations during testing, a large part of this thesis has gradually come to deal with the accuracy and the reliability of the measurement methods used during these ice abrasion tests.

I chose this assignment in order to be able to perform some practical experiments. In addition, fiber reinforcement is a relatively new and innovative technology, especially when it comes to its effect on ice abrasion, which makes it both interesting and exciting. It has been an educational experience working with this topic, where most of the time has been spent doing experimental work in the concrete ice abrasion laboratory at NTNU. Over 400 hours have been spent in total in the laboratory, including time-consuming repairs to the ice abrasion rig due to unforeseen problems with the equipment.

Acknowledgements

I would like to thank my supervisor at NTNU, Professor Stefan Jacobsen, for all his guidance, enthusiastic ideas and constructive feedback. I would also like to thank my contact at Kvaerner Concrete Solutions, Kjell Tore Fosså, for giving me the opportunity of writing this thesis on such an interesting topic and for his close follow-up and valuable inputs. Thanks also to Nicolai Segaard Greaker for his collaboration in the writing of this thesis. Plenty of good ideas and useful observations were reached during our many discussions.

Due to the many problems that occurred with the ice abrasion rig during testing, the technical staff at the NTNU concrete laboratory spent many hours helping me solve these issues. Thank you to Steinar Seehus, Gøran Loraas and Ove Loraas. Without their help, the experiments done for this thesis would never have been completed in time. In this regard, I would also like to thank Joakim Rydningen Kirkhaug who has been of great help in solving the many problems that have occurred with the ice abrasion rig. A final thanks goes to SINTEF for casting and carrying out freeze-thaw tests on the concrete specimens used in this thesis.

Table of Contents

List of Figures

Appendix Figures

List of Tables

Appendix Tables

List of Equations

Appendix Equations

1 Introduction

1.1 Introduction

The arctic regions are becoming more and more sought after when it comes to the extraction of natural resources. The harsh environments in these regions bring many new challenges in regard to the performance of the structures that are to be built. In areas near for example Sakhalin, Russia one of the new challenges to be faced is the occurrence of drifting sea ice, which has both a mechanical and an abrasive effect on the concrete structure. Structures such as bridges, piers, lighthouses and oil-platforms in arctic regions can be exposed to these conditions. Figure 1 shows the passage of such ice, which can drift with velocities up to 2.5 m/s (Jacobsen, Bekker et al. 2012) creating large mechanical forces and local stress concentrations when interacting with a structure. During the lifetime of such a concrete structure the cumulative distance of drifted sea ice past the structure can be up to four times the earth´s circumference, about 40,000 km (Rognlien 2013).

Figure 1 Sea of Okhotsk, picture taken from the Kvaerner Concrete Solutions brochure (2013)

Prolonged abrasive actions from ice on these structures may endanger the structural integrity of the concrete, as well as the functionality of the structure. Abrasive-erosive protection of such structures made of concrete requires durable concrete mixtures resistant to abrasion-erosion. Ice abrasion of concrete is therefore a subject that has to be taken into account in the design process of these structures. It is also a relatively new subject that requires further studies. To prepare and design for eventual damages due to ice abrasion, a better understanding of the interaction between ice and concrete is essential.

Field investigations of the effect of ice abrasion on concrete will give the best results in terms of understanding the actual effects. The downside here is that these types of investigations are very expensive and time consuming. Therefore, laboratory tests and experiments are often performed instead. These tests can give valuable results in terms of understanding the process of ice abrasion and which parameters of both the concrete and the ice that are affecting this process. Compressive/tensile strength, ductility, maximum aggregate size, surface roughness, average ice pressure, fiber content and temperature are some of the many parameters that may influence this phenomenon. Improved knowledge on how and in what degree these different parameters affect the ice abrasion of concrete will make it possible to predict the life expectancy of these structures more accurately. It will also result in a better understanding of which concrete types are most suitable for these conditions.

Research on ice abrasion of concrete has escalated the last couple of decades, especially in countries like Norway, Russia, Canada, Finland and Japan. Different research has focused on different parameters believed to have the largest influence on the abrasion rate. This can make it difficult to compare the results from these different studies, and further research is necessary to get a better understanding of the subject area.

1.2 Purpose and Scope

Kvaerner, being the worlds leading contractor for delivering onshore and offshore facilities to Arctic conditions (Kvaerner 2014), supports a number of projects related to material development through Concrete Innovation Centre (COIN). A special focus is on concrete structures exposed to ice abrasion, and the R&D includes fiber

reinforced concrete. Kvaerner Concrete Solutions has therefore initiated this study to improve the knowledge on the effect of fiber additions to concrete in regard to ice abrasion and freeze-thaw resistance.

The purpose of this study has been to compare how fiber reinforced concrete specimens, using different amounts and types of fiber, behave compared to standard offshore concretes without fiber, in regard to ice abrasion. Due to various observations during testing, a large part of this study has gradually come to deal with the accuracy and the reliability of the measurement methods used during these ice abrasion tests. The emphasis of this thesis is therefore laid on both the abrasion resistance of the fiber reinforced concrete and the accuracy of the measurements, but the effect of fiber addition in regard to the freeze-thaw resistance has also been studied. It has also been of interest to evaluate how parameters such as sliding velocity and surface roughness affect the abrasion resistance of the concrete.

The results of this study should give Kvaerner an indication of which concrete types that are most appropriate to use when delivering concrete oil rig sub-structures for arctic environments in the future. It should also provide them with ideas on how to improve these concrete ice abrasion tests, especially in regard to the accuracy of the measurements.

The concrete ice abrasion test rig is self-built at NTNU and there is little research on how results from this rig are compared to actual field conditions. In this study the abrasion rate is tested for the different concrete products for a given set of test conditions, which are meant to represent actual field conditions as best as possible. Nevertheless, comparison of results from this study to real field abrasion is limited.

1.3 Methodology

The results of this thesis are based on laboratory work done using the self-built ice abrasion test rig at NTNU, and a literature review. A literature review was performed to increase the understanding and knowledge of concrete ice abrasion in order to deliver a state of the art presentation of this research area in this work. Information was mostly gathered from journal articles, but also from the Internet,

textbooks and previous dissertations. Search engines such as Science Direct, Scopus, Compendex and BIBSYS were all used in order to find the most relevant journal articles relating to ice abrasion of concrete and specifically fiber reinforced concrete. The literature review is presented in Chapter 2, while the setup and results from the laboratory work are presented in Chapters 3 and 4.

2 Background

2.1 Fiber Reinforced Concrete

Fiber reinforced concrete is concrete containing fibrous material, which increases its structural integrity. It may contain either short or long fibers that are uniformly distributed and randomly oriented. These fibers can be made of different materials such as steel, glass, basalt, natural or synthetic materials, for each of which affect the concrete properties in their own way. In this paper there are used steel, polypropylene and basalt fibers. Therefore, a short look at these fibers effect on concrete properties will be taken in this chapter. Many different studies are discussed, so for a more detailed description of the concrete compositions, refer to these studies.

2.1.1 Fiber Reinforced Concrete Properties

The addition of fibers to concrete affects a number of characteristics for both fresh and hardened concrete. The addition of fibers has a positive effect, because in the early phase, approximately 2-6 hours upon the placing of concrete, they contribute to the reduction of both size and frequency of cracks due to early drying and plastic shrinkage. This is because they allow concrete to endure higher internal stresses. Also, addition of fibers to concrete improves the hydration of cement by reducing the separation of water from the fresh concrete. In a later period, in a more mature concrete, the fibers bind the potential cracks and reduce the risk of concrete destruction (Grdic, Curcic et al. 2012). In the following, a literature review on the effect of fiber on fresh and hardened properties of concrete is presented.

Workability

The addition of fibers, especially steel fibers, and the increase of fiber content cause a decrease in the workability because the fibers hinder the flowability of the fresh concrete. This has been shown in studies done by (Atis and Karahan 2007) and (Topcu and Canbaz 2006) where a decrease of the workability of up to 8% has been observed based on slump tests on fly ash concrete with addition of 0.05% polypropylene fibers. This was also experienced in the process of

mixing the concrete for the specimens used in this thesis, where the specimens with 1.5% addition of steel fibers showed a considerably lower workability than the rest.

Compressive Strength

Previous studies show various results when it comes to the effect of the addition of fibers on the compressive strength of the concrete. (Topcu and Canbaz 2006) found that the compressive strength increased with the addition of both steel and polypropylene fibers between 18-95% at different fiber dosages. This can be due to the fact that under axial loads, cracks occur in the microstructure of the concrete and fibers reduce the crack formation and development. Thus, compressive strength of concrete is increased. On the other hand, both (Atis and Karahan 2007) and (Olivito and Zuccarello 2007) found that the addition of steel fibers did not improve the compressive strength. Only a minimal increase in compressive strength was observed with the increase of steel fiber content. The addition of basalt fiber also showed no remarkable improvement in compressive strength in a study done by (Li and Xu 2009). Based on these various studies, the effect of fibers on the compressive strength of concrete is not clear and is a topic that requires further research.

Tensile Strength

The studies done by (Atis and Karahan 2007), (Olivito and Zuccarello 2007) and (Topcu and Canbaz 2006) all show an increase in splitting tensile strength with the addition of fibers. Fibers, especially steel fibers, make the concrete less brittle and more ductile, which in turn results in an increased tensile strength. Topcu´s study reported an increase between 22-54% when introducing steel fibers. Atis´s study reported an increase in splitting tensile strength varying from 1% to 5%, 1% to 3%, 21% to 32% and 44% to 71% for concrete mixes having 0.25%, 0.5%, 1.0% and 1.5% volume fractions of steel fibers, respectively. These concrete mixes had a compressive strength after 28 days in the range 60-80 MPa. (Grdic, Curcic et al. 2012) observed the same trend. Using polypropylene fibers, a 9.5-13.4% increase in tensile strength in concretes with water/cement ratio 0.5 was reported.

Bending Strength

The use of fiber addition in concrete has been shown to have a positive effect on its bending strength. (Topcu and Canbaz 2006) found that the bending strength increased with up to 100% with the use of steel and polypropylene fibers. Under bending loads, tensile stresses occur in the microstructure of the concrete and fibers withstand this tensile stress, thus, bending strength of concrete increased. (Sun and Xu 2009) found an increase of up to 15% on the flexural strength with the use of polypropylene fibers between 0.45-1.35 kg/m^3. A flexural strength increase was also found with the additions of steel fibers in studies done by (Olivito and Zuccarello 2007) and (Atis and Karahan 2007). Atis´s study showed no significant effects on flexural tensile strength at 0.25% and 0.5% volume fractions. But, the improvement started from 0% to 15% at 1.0% volume fraction and expanded to 30–66% increment at 1.5% volume fraction.

Freeze-thaw Resistance

In (Atis and Karahan 2007) it is found that the strength loss of concrete due to freeze-thaw testing is reduced up to 5% with the use of steel fibers. Due to the freezing of water in the concrete pores, the concrete may expand, if not properly air-entrained, which in turn induces tensile stresses in the concrete. These tensile stresses will disintegrate the concrete when they exceed the tensile strength of concrete. However, randomly distributed fibers in the concrete mixture will help restrain these expansions and in this way reduce the freeze-thaw damage to concrete.

(Richardson, Coventry et al. 2012) examined the effect of polypropylene fibers on the air void content and structure in the concrete, which is closely related to the freeze-thaw resistance. Using a fiber dosage of 0.9 kg/m^3, an additional 1.5% air voids were found compared to plain concrete, and the voids were closer together. This improvement in air void content results in a better freeze-thaw resistance.

2.1.2 Effect of Fiber Reinforcement on Abrasion Resistance

Few previous studies have been done on the effect of fiber addition when it comes to ice abrasion of concrete. There have been, though,

many studies on the effect of fiber addition when it comes to general abrasion resistance. In the following literature study, different methods have been used for testing the general abrasion resistance. In the underwater method (ASTM-C1138), the concrete specimen is immersed and rotated in water filled with steel grinding balls. In the ball bearings abrasion test (ASTM-C779), the ball bearing machine operates under high-contact stresses, impact and sliding friction from steel balls. The abrasive action is applied by rapidly rotating ball bearing under load on a wet specimen test surface (Febrillet, Kido et al. 2000). The final method used in the following literature study is the Bőhme test method. In this method the test specimen is placed on the test track of a 750 mm diameter cast iron disc. Standard abrasive is strewn on this track, and with a contact force of 294±3 N the disc is rotated at 30 rpm for a given number of cycles. The abrasive wear is determined as the loss in the sample volume (Pettit 2003).

Figure 2 shows the comparison of the abrasion resistance test results of nine high strength concretes using the underwater method and the Böhme´s disc method. Concrete mixes C1-C3 have no fiber additions, mixes C4-C8 have additions of steel fiber, whereas mix C8 also has a latex addition of 25% of the cement mass, and mix C9 has an addition of PVC fiber. The Böhme disc method shows a wear of 1.5-1.8 mm- similar for all the concrete mixes, while the underwater method shows a larger difference in abrasion rates between the different concrete mixes. In this regard, it is important to have in mind the substantial difference of these two abrasion methods, as explained above. According to (Horszczaruk 2005), the underwater method simulates the natural conditions of abrasive concrete wear and seems to be a better method for comparative analysis of abrasive resistance of standard and high-strength concrete. Concrete mix C9 shows the least amount of wear based on the underwater method, possibly pointing towards a positive effect from PVC fibers on abrasive wear.

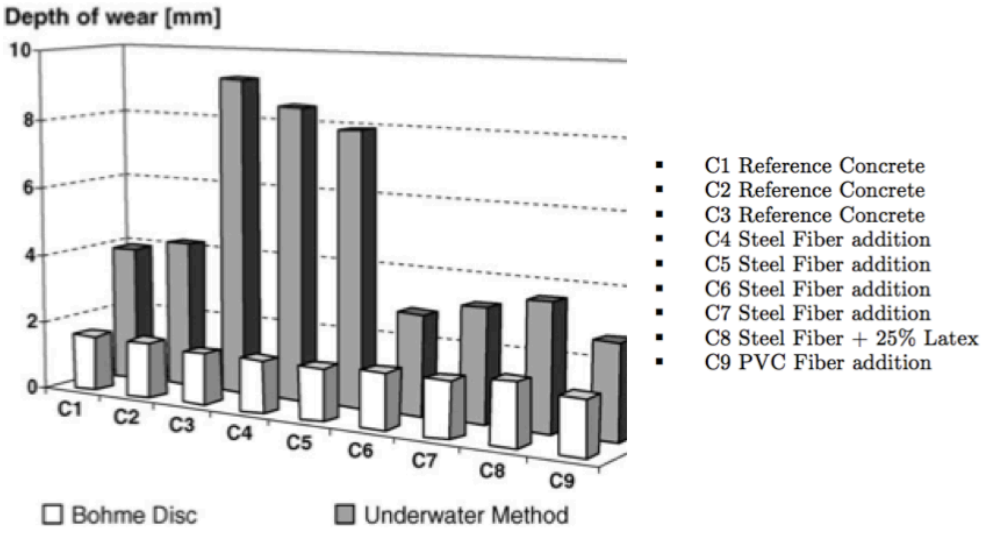

Figure 2 Comparison of abrasion rates using the underwater method and the Böhme disc method (Horszczaruk 2005)

Many studies have been done to assess the effect of steel fiber addition to abrasion resistance. (Febrillet, Kido et al. 2000) carried out abrasion tests using the ball bearing test and found that the addition of steel fibers has a positive effect on the abrasion resistance. The same results were found in both (Atis, Karahan et al. 2009) and (Horszczaruk 2009) in which abrasion resistance was measured by the use of the Böhme test method and the underwater method, respectively. Abrasion resistance was also found to increase with an increasing volume fraction of steel fiber.

(Nanni 1989) studied the abrasion resistance of roller compacted concrete using the ball bearings abrasion test, and found that neither the addition of steel nor polypropylene fibers affect the abrasion resistance. (Kabay 2014) used the Böhme test to study the abrasion resistance of basalt fiber reinforced concrete. It was found that, even at low contents, basalt fiber improved abrasion resistance. Increased amount of fiber content and fiber length were both found to improve the abrasion resistance.

(Maage 1977) studied the effects of steel fiber content in concrete in regard to abrasion. It is found that small amounts, up to 1% volume fraction, of steel fiber gives a reduced abrasion resistance, while larger amounts, up to 2%, gives an increased abrasion resistance. It is found

that the steel fibers increase the ductility of the concrete, which in turn makes it harder for parts of the concrete to be pulled off. Also mentioned, is the effect of protruding steel fibers, which form a type shelter for the concrete in the "shadow area" behind the protruding fiber. On the other hand, these protruding fibers can also have a negative effect as they can act as crowbars and pull out parts of the concrete. This crowbar effect is reported to mostly be applicable to lower quality concretes with small volume fractions of fiber.

Many previous studies have shown a positive effect on abrasion resistance with the use of polypropylene fibers. (Sun and Xu 2009), (Siddique, Kapoor et al. 2012), (Felekoglu, Türkel et al. 2007) and (Grdic, Curcic et al. 2012) all report results showing that the use of polypropylene fibers give a higher abrasive resistance. Grdic´s study found an increase in abrasion resistance between 7-15% in concretes with a water/cement ratio 0.5 and added polypropylene fibers compared to a reference concrete without fiber addition. Sun and Xu found that 0.9 kg/m^3 addition of polypropylene fiber on concrete mixes, all with a water/cement ratio of 0.42 and compressive strength approximately 50 MPa, resulted in a 37.4% decrease in abrasion mass loss. Felekoglu et al. found that steel fiber (156 kg/m^3) addition decreased weight loss of concrete due to abrasion by 42% on concrete mixes with a water/cement ratio 0.5 and 28-day compressive strength approximately 50 MPa. On the other hand, (Atis, Karahan et al. 2009) found no evidence of polypropylene fibers improving the abrasion resistance on concrete mixes with water/cement ratio 0.35 and compressive strength in the range 60-80 MPa.

The general conclusion from these various studies is that the use of steel, polypropylene and basalt fibers in concrete will increase the abrasion resistance. This is partly due to their effect of increasing the ductility of the concrete. The abrasion resistance also tends to increase with increasing amounts of fiber.

2.1.3 Effect of Fiber Reinforcement on Freeze-Thaw Resistance

The long-term durability of fiber reinforced concrete structures under freeze-thaw cycling is crucial to the safety of structures in cold climates (Yun and Wu 2011). The effect of fiber additions on the freeze-thaw durability of concrete has been researched in various studies. (Sun, Zhang et al. 1999), (Mu, Sun et al. 2002) and

(Richardson, Coventry et al. 2012) have all executed freeze-thaw testing, the first two in accordance with ASTM C666 Procedure A and the last one in accordance with ASTM C666 Procedure B. Procedure A consists of rapid freezing and thawing in water, while Procedure B consists of rapid freezing in air and thawing in water. The first two mentioned studies report positive effects on freeze-thaw resistance using steel fibers. The crack-growth resistance effect from steel fiber may inhibit the damage of concrete incorporated with steel fiber from freeze-thaw testing. Richardson´s study observes the same positive effect in regard to freeze-thaw durability, but with the use of polypropylene fibers. This positive effect was believed to be because of the fibers ability to entrain air in the concrete.

Richardson has also compared concretes with and without polypropylene fibers to the durability factor (ASTM-C666 2008). This factor relates to the relative dynamic modulus between the original reading taken prior to the freeze-thaw cycles and the final reading as a percentage. Further it is factored as a fraction of the actual numbered cycles completed over the full test divided by the specified number of cycles for the test.

A durability factor of 100, after freeze-thaw testing, is indicative of a sample for which no structural alteration in the material has occurred. If the durability factor has decreased it means that structural damage has occurred. Failure to the concrete is deemed to have occurred when the relative dynamic modulus reaches 60% of the initial modulus (Richardson, Coventry et al. 2012).

Using the durability factor, Richardson found that concrete with polypropylene fibers at 0.9 kg/m^3 is 88 times more effective than plain concrete in regard to freeze-thaw durability. In other words, the durability factor was 88 times larger for the concrete with polypropylene fibers than for the plain concrete. Concrete with 1.8 kg/m^3 polypropylene fibers was found to be 85 times more effective in the same regard as plain concrete.

In (Cavdar 2014), fiber reinforced mortar properties under repetitive freeze-thaw effects were studied. These mortars had a water/cement ratio of 0.5 and 28-day compressive strengths of approximately 50 MPa. After 100 freeze-thaw cycles, flexural strength, compressive strength and modulus of dynamic elasticity of the control samples without fiber addition decreased 23%, 14% and 9%, respectively.

These decreases for fiber reinforced mortars were on average 12%, 10% and 8%, respectively.
Based on these various studies, fiber reinforcement is expected to improve the freeze-thaw resistance of concrete by improving the ductility, increasing the crack growth resistance, and increasing the entrainment of air in the concrete.

2.2 Ice

When it comes to ice abrasion of concrete, it is not only the properties of the concrete that are important to look at, but also the properties of the ice. In this chapter a brief description of ice and it´s properties are presented.

2.2.1 Physical Properties

Ice is basically water frozen into a solid state. Ice can be split up into two main groups, sea ice and freshwater ice. Freshwater ice can consist of solid ice, gas and other material that has been trapped within the ice. Sea ice can also consist of brine and depending upon the temperature, various types of solid salts(Timco and Weeks 2009). When water freezes, it expands with approximately 9%, which makes the theoretical density of freshwater ice 0.917 kg/m^3. However, the actual density of freshwater ice differs from the theoretical density due to parameters such as air content, thermal history and age.

The density of sea ice is a complicated issue due to, among others things, the presence of salts. A general conclusion has been drawn in (Bergdahl 1977) that sea ice is weaker than freshwater ice. (Timco and Frederking 1996) did density measurements on first year and multi-year sea ice. They found that the density of first year sea ice ranges from 840 to 910 kg/m^3 for the ice above the waterline, and from 900 to 940 kg/m^3 for the ice below the waterline. It was also found that the density of multi-year sea ice is a bit lower, but similar to first year sea ice. For a more detailed description of the effect of growth-history and salinity on the density of sea ice, refer to (Timco and Weeks 2009).

2.2.2 Mechanical Properties

The mechanical properties of ice are of most interest when studying concrete ice abrasion. Important parameters are compressive and tensile strength, shear strength, fracture toughness and hardness. According to (Timco and Weeks 2009) and (Petrovic 2003) the strength of ice depends on variables such as temperature, strain rate, density, salinity, ice type and loading direction.

In the temperature range -10 to -20°C, the average tensile strength of ice is in the range 0.7 MPa to 3.1 MPa, with an average tensile strength from published investigations of 1.43 MPa. The compressive strength in this same temperature range varies between 5-25 MPa(Petrovic 2003). The strength of ice generally increases with decreasing temperature in compression and also slightly in tension, as shown in Figure 3. The effect of strain rate on the compressive and tensile strength of ice can be seen in Figure 4. The strain rate has a large effect on the compressive strength, but nearly no effect on the tensile strength.

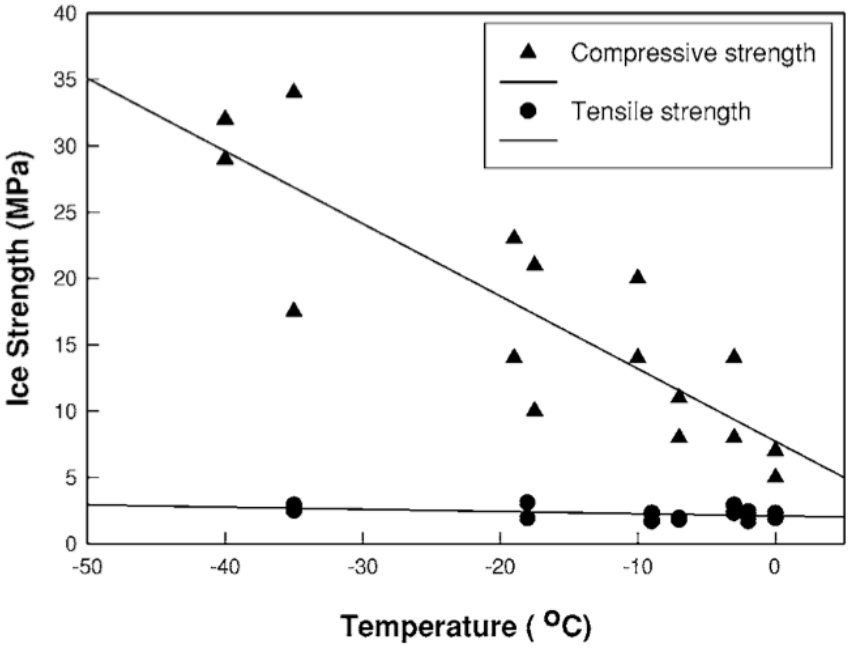

Figure 3 Relationship between ice temperature and strength (Petrovic 2003)

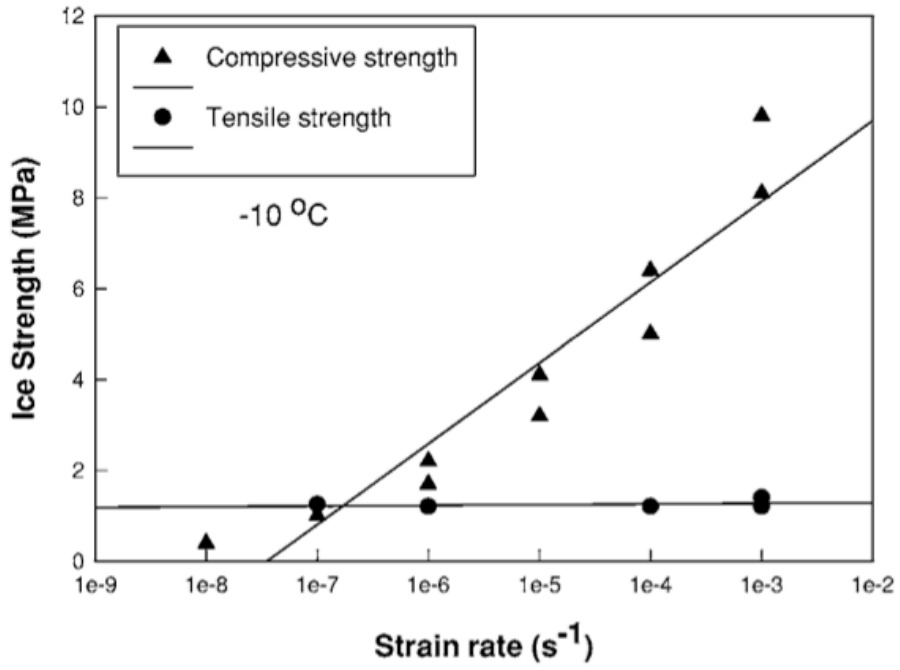

Figure 4 Relationship between strain rate and ice strength (Petrovic 2003)

The fracture toughness of ice, which describes the stress required to make a crack propagate, is generally in the range of 50-150 kPa $m^{1/2}$(Petrovic 2003). The average shear strength is reported to be in the range of 550±120 kPa and tends to increase when the temperature decreases (Timco and Weeks 2009). The hardness of ice is also very closely related to the temperature. Figure 5, replotted from (Barnes and Tabor 1966) by (Jacobsen, Scherer et al. 2013), clearly shows how the hardness of the ice varies with the temperature and how the hardness drops sharply close to the melting point.

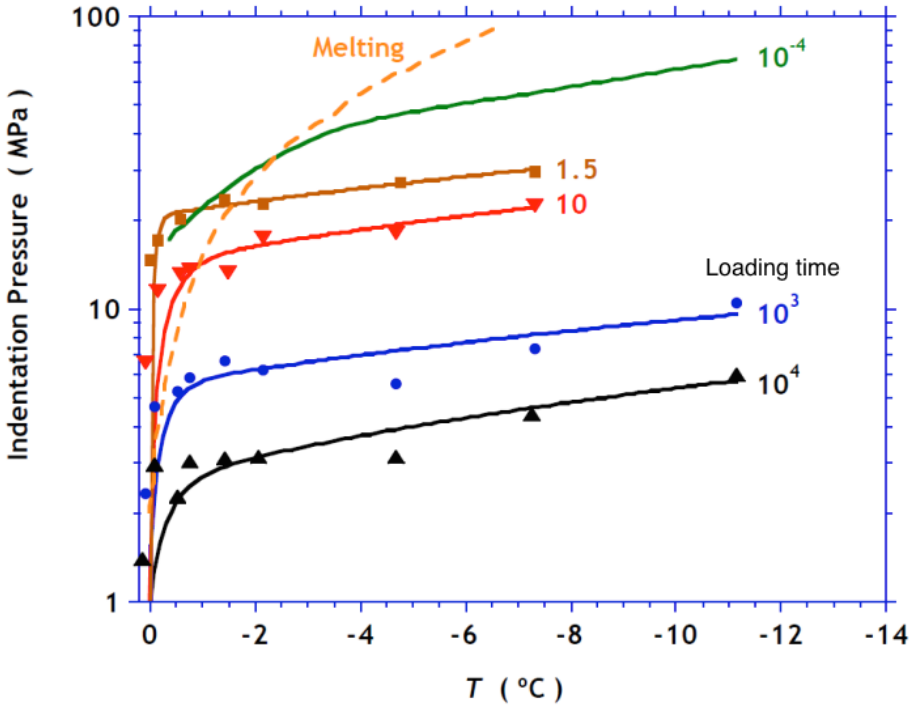

Figure 5 Relationship between temperature and hardness of ice, replotted from (Barnes and Tabor 1966) by (Jacobsen, Scherer et al. 2013)

2.3 Concrete Ice Abrasion

In areas with drifting ice, like the arctic seas, ice abrasion is a likely wear mechanism that can occur on concrete structures. Even though concrete is harder than ice, over time the friction induced forces between concrete and ice can become so large that the concrete begins to wear. This, in turn, leads to reduced capacity and reduction of reinforcement cover depth, which can decrease the lifetime of the structure or require costly and challenging repair of the structure.

2.3.1 Mechanism

The fundamental mechanism behind the ice abrasion of a concrete structure is more complex than barely the force of friction between moving ice and concrete. Field investigations and laboratory tests suggest that the observed abrasion is a result of the combination of

environmental causes together with the ice impact forces. Concrete ice abrasion can occur, though, without any freeze-thaw deterioration. This is clearly seen in the icebreaker tests done in (Huovinen 1993) where concrete specimens were fastened onto the bow of the icebreaker at water level. Mean values of abrasion between 2-15 mm were measured during these experiments, without there being time for any freeze-thaw deterioration to occur. On structures in cold environments, on the other hand, freeze-thaw deterioration may play a part in the abrasion due to weakening of the concrete. The environmental deterioration is a result of cyclic freezing and thawing and is known to cause a gradually weakening of the matrix and the aggregate bond interface. In some areas, for example in rivers, the ice might contain grit and hence induce an even more severe abrasion condition, known as the sandpaper effect (Møen, Jacobsen et al. 2007).

One way to measure concrete ice abrasion is as an abrasion rate, the wear in millimeter per kilometer of ice sliding (mm/km). This abrasion rate depends on different properties of both the ice and the concrete. The sliding velocity, average ice pressure and temperature are all decisive parameters. According to (Huovinen 1993) the abrasion mechanism due to crushing ice sheets against the concrete surface is of three kinds; abrasion of cement paste (Figure 6a), abrasion of cement paste + loosening of protruding aggregate particles (Figure 6b), and abrasion of cement paste when the bond strength between larger aggregate particles and the cement paste is so weak that the particles loosen during the first ice impact (Figure 6c).

The mechanism behind the abrasion of cement paste is studied in (Jacobsen, Sætre et al. 2013). In brief, the Hertzian contact stress (Hertz 1881) causes tensile fracture at the rim of a point contact between an asperity and a surface of ice and concrete. The maximum tensile stress in the concrete surface during ice abrasion depends on the maximum contact stress. (Jacobsen, Scherer et al. 2013) has shown that for ice crystals this is sufficient to fracture concrete since the maximum tensile stress in the concrete is further intensified under sliding contact. Then, a tensile component resulting from the frictional shear can cause additional tensile stress to the Hertzian effect at the rim of the point contact (Hamilton and Goodman 1966).

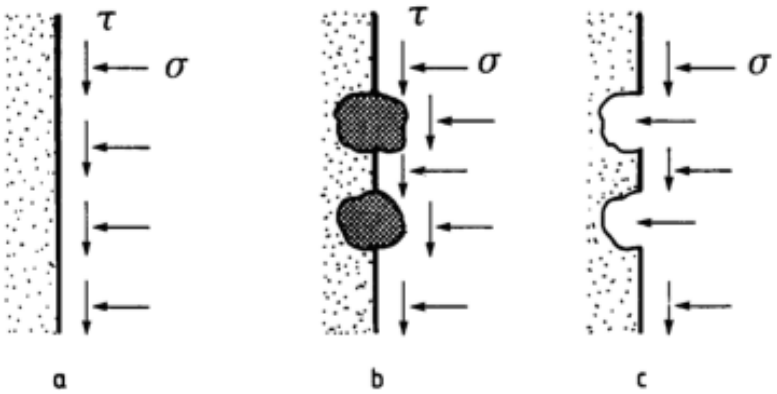

Figure 6 The sequence of events in the abrasion of concrete by ice (Huovinen 1993)

(Fiorio 2005) has a similar way of explaining ice-abrasion of concrete. Fiorio found that concrete wear due to ice appeared to be a result of two general phenomena. A gradual and uniformly distributed general wear, and a much faster time and space localized catastrophic wear. General wear corresponds to the mechanical wear of the cement paste, whereas catastrophic wear corresponds to the pulling out of coarse sand particles from the surface layer of the plate. This happens when the particle-cement paste bond has been sufficiently embrittled by the abrasion of the cement paste. Thus, catastrophic wear appears as a consequence of the mechanism of general wear. Figure 7 illustrates general and catastrophic wear.

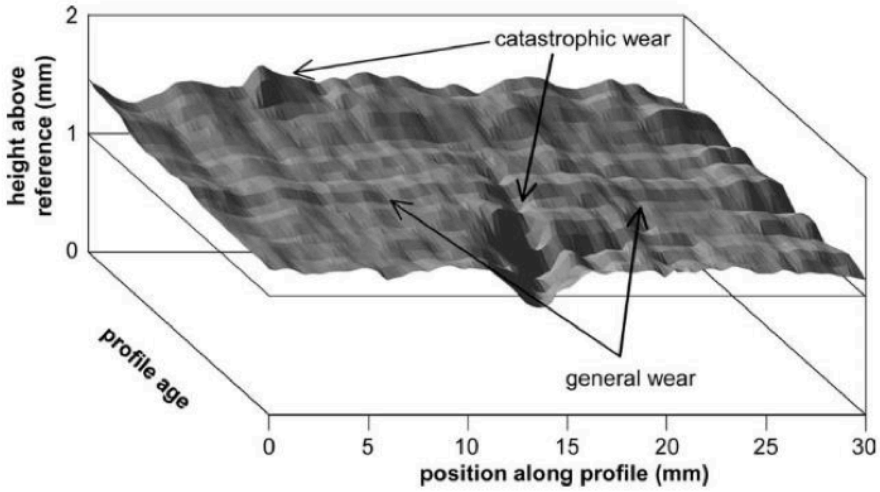

Figure 7 Illustration of the effect of general and catastrophic wear (Fiorio 2005)

2.3.2 Effect of Concrete Properties on Abrasion Resistance

There are many concrete properties, other than fiber content as discussed in section 2.1.2, that have an influence on the abrasion resistance of concrete. Compressive strength, tensile strength, flexural strength, ductility, maximum aggregate size and surface roughness are some of the many properties that may influence this phenomenon. Few studies have been done on the effect of these properties on the ice abrasion of concrete. However, many studies have looked at the effect of various concrete properties on the general abrasion resistance. The results of some of these studies are presented in this section.

Compressive strength is generally reported as the most important factor that influences the abrasion resistance of concrete. However, in concretes with fibers, it seems that abrasive wear is mainly influenced by the flexural strength rather than the compressive strength (Kabay 2014). The relationship found in Kabay´s studies between flexural strength and abrasive wear can be seen in Figure 8. Various papers report observations supporting this trend, among others (Grdic, Curcic et al. 2012) and (Atis, Karahan et al. 2009).

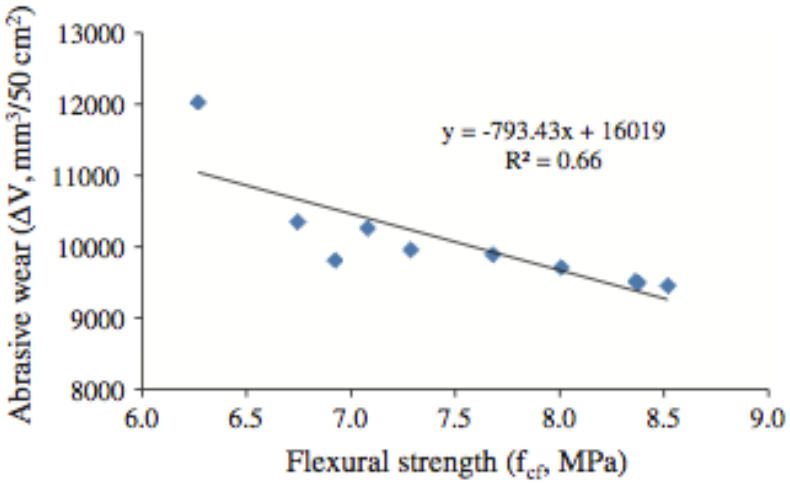

Figure 8 Relationship between flexural strength and abrasive wear (Kabay 2014)

In (Maage 1977), (Dhir, Hewlett et al. 1991) and (Grdic, Curcic et al. 2012), the water/cement ratio is shown to have a large influence for the abrasion resistance of concrete, the trend being that a lower

water/cement ratio results in a lower abrasion rate. This is in line with the studies showing that the concrete strength affects the abrasion rate, seeing that as the w/c ratio decreases, the concrete strength increases. The results from Grdic´s study on the effect of water/cement ratio can be seen in Figure 9 with the Benchmark being concrete without fiber reinforcement and the F120 and S120 being concretes with different types of polypropylene fiber reinforcement.

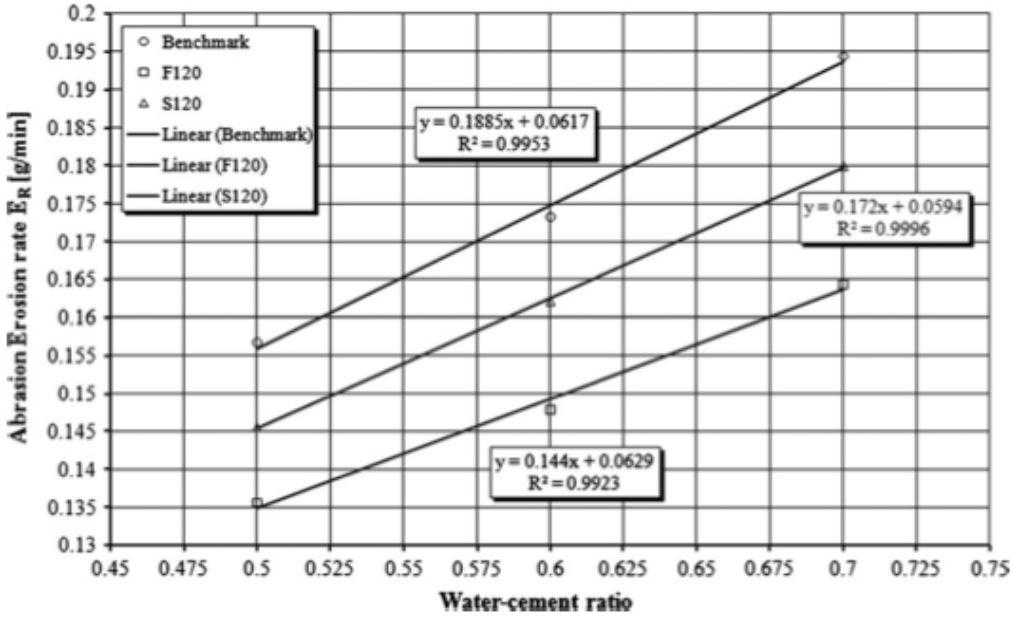

Figure 9 Relationship between water-cement ratio and abrasion rate (Grdic, Curcic et al. 2012)

(Dhir, Hewlett et al. 1991) used an accelerated test machine and found several other factors affecting the abrasion resistance. The test machine, of rolling wheel type, abrades the surface of concrete by means of a combined rolling, sliding and light impact action. Among other findings, the maximum aggregate size was found to have an effect on the abrasion rate, as could be seen in Figure 10.

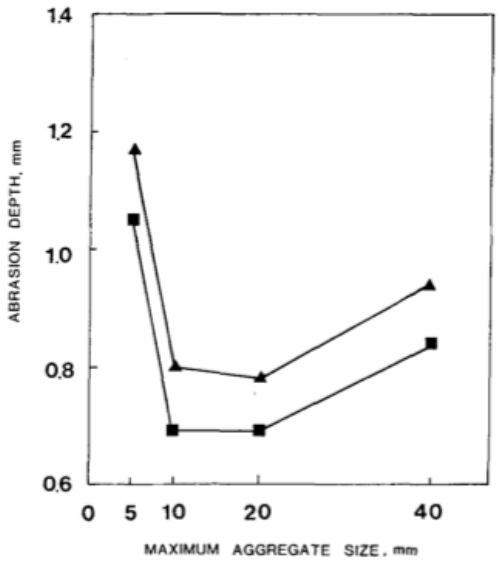

Figure 10 Relationship between maximum aggregate size and abrasion rate (Dhir, Hewlett et al. 1991)

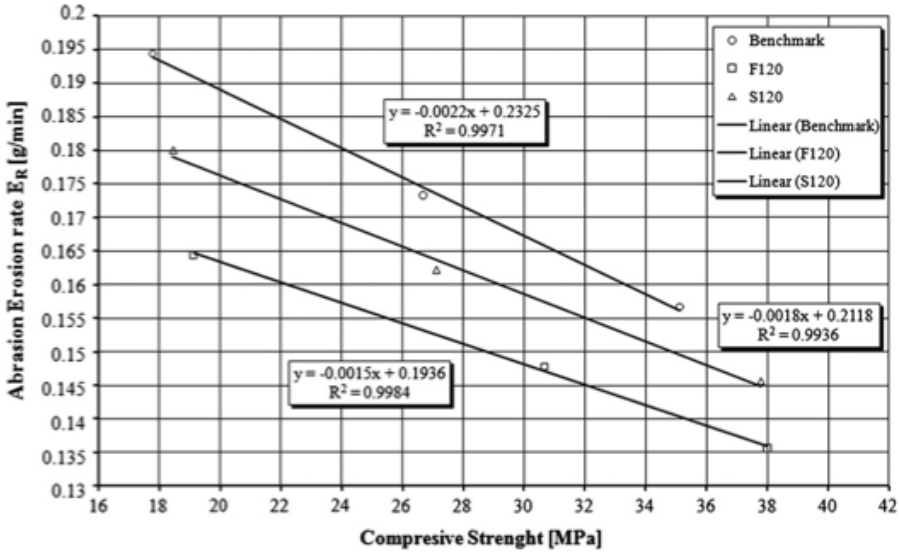

Figure 11 Relationship between compressive strength and abrasion rate (Grdic, Curcic et al. 2012)

Both (Grdic, Curcic et al. 2012) and (Siddique, Kapoor et al. 2012) also find a stronger relationship between compressive strength and abrasive wear than what was reported in Kabay´s studies. The effect

found in Grdic´s studies, being that increased compressive strength minimizes abrasive wear, can be seen in Figure 11.

The studies in this section have shown that a decreased abrasion rate can be expected with an increase in flexural and compressive strength, a decrease in water/cement ratio and a maximum aggregate size in the range 10-20 mm.

2.3.3 Wear Profile

(Itoh, Yoshida et al. 1988) studied the ice abrasion of lightweight concrete made with normal density fine aggregate and lightweight coarse aggregate. A 10 cm wide concrete specimen was slid back and forth on an 8 cm wide block of sea ice for 5 km at 5 cm/s, a temperature of -20°C and an average ice pressure of 1 MPa. Figure 12 shows the wear profile at 0 and 5 km wear distance along different sections of the specimen. The surface profile at the wear distance of 5 km is a U-shaped distribution in which the wear depth at the center is larger than at either side. Presumably the pressure (ice and/or water) was varying across the surface. Itoh´s concrete specimen was a bit wider than the ice. Due to the varying degree of restraint there might have been less of a three-dimensional stress state close to the edge of the ice block compared to along the central line of the movement path on the same ice block. At NTNU´s laboratory the ice is confined within a steel cylinder, presumably producing a more homogeneous stress state in the ice (Jacobsen, Sætre et al. 2013).

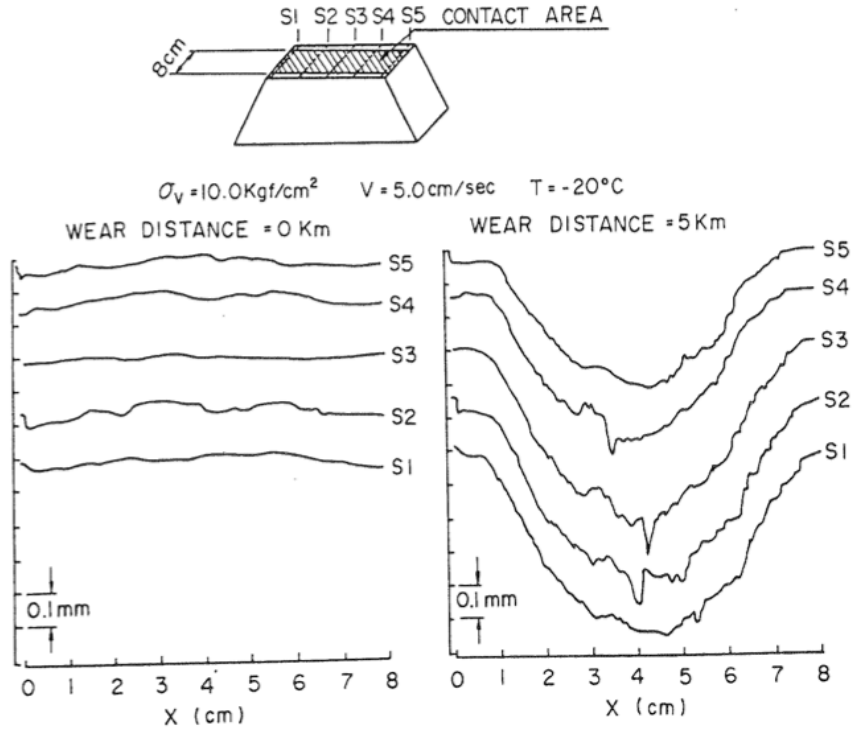

Figure 12 Wear profile at 0 and 5 km wear distance along different sections (Itoh, Yoshida et al. 1988)

2.4 Freeze-Thaw Resistance

In cold environments, freeze-thaw cycles can be harmful to a porous and brittle material such as concrete. When water begins to freeze in a capillary cavity, the increase in volume accompanying the freezing of water requires a dilation of the cavity equal to 9% of the volume of frozen water, or forcing of the amount of excess water out through the boundaries of the specimen, or a combination of both these effects. Parameters such as the permeability of the cement paste, the degree of saturation, the distance to the nearest unfilled void and the rate of freezing all affect the magnitude of this hydraulic pressure. If this pressure exceeds the tensile strength of the paste at any point, it will cause local cracking. In repeated cycles of freezing and thawing in a wet environment, water will enter the cracks during the thawing portion of the cycle, only to freeze again later and there will be

progressive deterioration with each freeze-thaw cycle. Eventually, this may decrease the strength of the concrete (Cavdar 2014).

When it comes to the freeze-thaw resistance of concrete, we are interested in the air/macro pores. A 4-6% air/macro pores content by volume of concrete usually leads to a frost resistant concrete. The pore protection factor, PF, is the air content as a percentage of the total porosity, and is used to assess the frost resistance of concrete. The PF should be above 25% for frost resistant concrete in the presence of salts (Jacobsen 2009). Another way of characterizing the air voids is to use the spacing factor, which gives an average of the maximum distance from any point in the cement paste to an air-void boundary. The specific surface, which is the ratio of the surface area of the air voids to their volume, is also useful. In general, a good quality, frost resistant concrete requires a spacing factor < 0.20 mm and a specific surface greater than 25 mm^{-1} (ASTM-C457).

2.5 Surface Measurement Techniques

2.5.1 Standard Digital Indicator

A standard digital indicator is an example of a stylus instrument and is classified as a contact measuring method. It is based on the principle of running a probe across a surface in order to detect variations in height as a function of distance (Thomas 1999). The digital indicator is moved on a grid over the surface and deviations are measured at the grid points. An error source can be the size and the shape of the tip/stylus interacting with the surface. The effect of stylus size is illustrated in Figure 13, which is a schematic comparison of an actual profile against the traced profile.

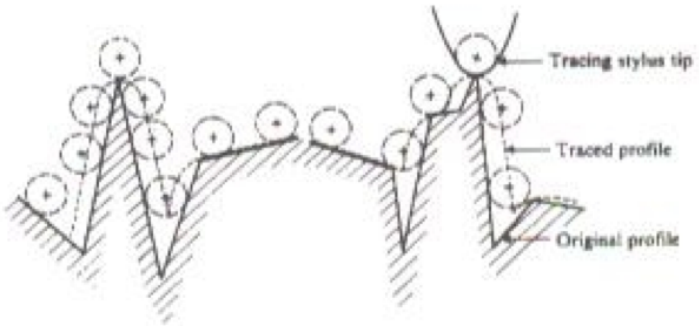

Figure 13 Illustration of the effect of stylus size (Kobrick, Klaus et al. 2011)

2.5.2 3D Optical Scanning

3D Optical Scanning is an example of a non-contact measuring method. It consists of creating a virtual three-dimensional image of the test surface by scanning it with a 3D optical scanner. The resulting image is a cloud of points with known positions (named coordinates *x, y and z* in the adopted coordinate system) on which smallest possible triangles are drawn to create a dimensional approximation of the scanned surface (Siewczynska 2012).

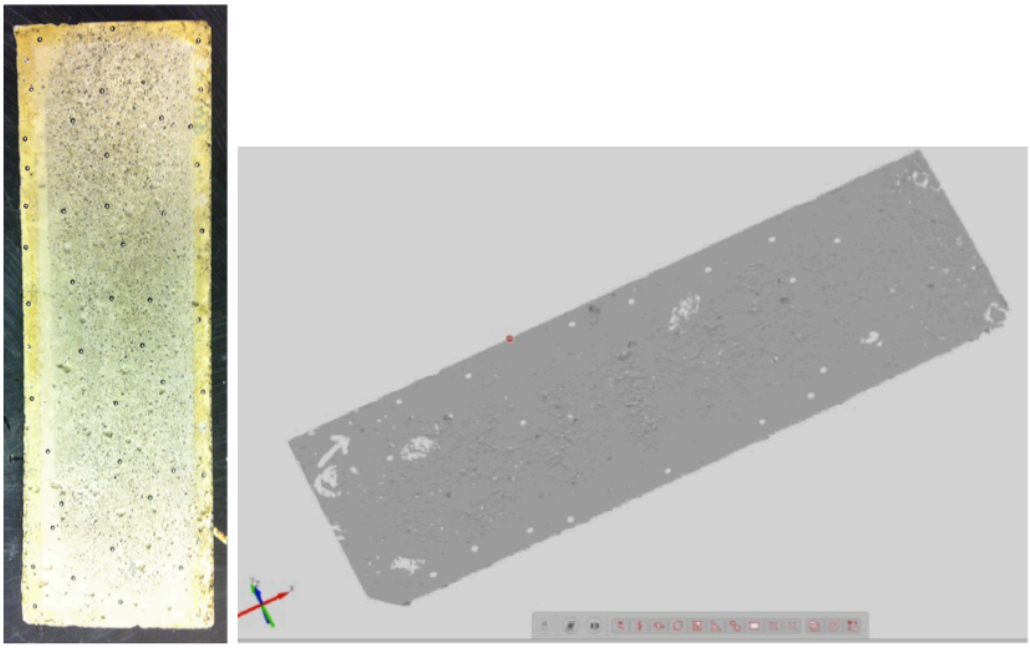

Figure 14 Comparison of an image obtained by 3D scanning with a real image, 300x100 mm (GOM 2013)

The accuracy of this image approximation is determined by the resolution of the scanner used. An ATOS III 600 scanner is available at NTNU, which gives a scan of nearly one million points on a 300x100 mm concrete surface. The exact accuracy of the ATOS III 600 is difficult to specify as it depends on the surface being measured, how it is prepared, how the measurements are performed, and which scanning parameters that are used. However, an accuracy of 0.01 mm should be able to be reached if the measurements are performed correctly.

The result of a three-dimensional surface scan is a spatial image, consisting of triangles with known coordinates of the vertices. Several scans have to be performed to cover the entire surface and a certain number of reference points (black dots in Figure 14) from one of the previous scans have to be visible for the scanner to be able to fit the scans properly together. After the entire surface is scanned, the images are ready to be polygonized, resulting in the scan of the surface seen in Figure 14. Using a compatible program, for example GOM Inspect, data can be extracted from these scans and used for abrasion and surface roughness analysis.

2.6 Surface Roughness

It is well known that different surfaces reflect different tribological properties, with roughness having a major impact on friction (Sedlacek, Podgornik et al. 2012). The roughness of a surface may help predict how materials interact with each other (Archard 1953). To be able to characterize and classify different surfaces, roughness parameters have been developed. Roughness is a characteristic of the surface that identifies its inequality (elevations and depressions), which is nothing less than the order of magnitude smaller than the size of the element (Siewczynska 2012). Roughness parameters can be calculated in either two-dimensional (profile roughness) or three-dimensional forms (surface roughness). 2D profile analysis has been widely used in science and engineering for more than half a century. In recent years, though, there has been an increased need for 3D surface analysis. 3D roughness parameters are calculated for an area of the surface instead of a single line, and may therefore represent the surface characteristics more accurately and be more useful when studying the wear/abrasion rate of concrete. The following sections

introduce some of the most commonly used profile and surface roughness parameters.

2.6.1 Profile Roughness Parameters

Average Roughness (R_a)

The *Average Roughness (R_a)* parameter is the most universally used roughness parameter for general quality control (Gadelmawla, Koura et al. 2002). It is defined as the average absolute deviation of the roughness irregularities from the mean line over a sampling length, as shown in Figure 15. Simply put, R_a is the average of a set of individual measurements of a surfaces peaks and valleys.

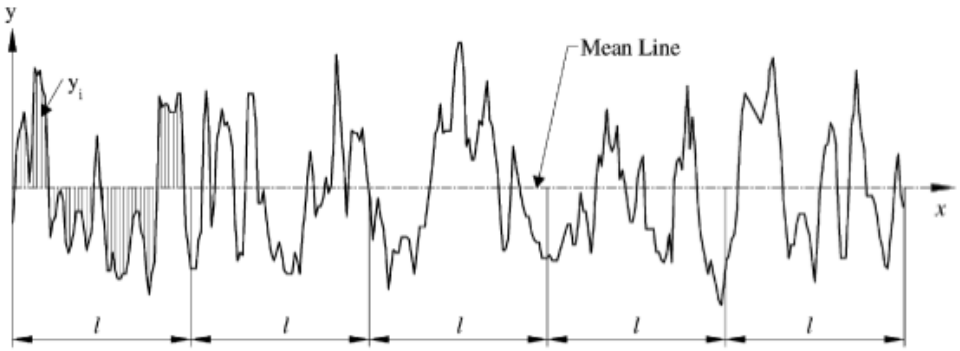

Figure 15 Definition of the arithmetic average roughness (Ra) (Gadelmawla, Koura et al. 2002)

This parameter is easy to define, easy to measure and gives a good general description of height variations. The mathematical and numerical formulas for the average height parameter are presented in Equations 2.1 and 2.2, where *l* is the evaluation length, *y(x)* is the profile height function, and y_i is the deviation from the mean line for *n* measuring points:

$$\boldsymbol{R_a = \frac{1}{l}\int_0^l |y(x)|dx} \tag{2.1}$$

$$\boldsymbol{R_a = \frac{1}{n}\sum_{i=1}^{n} |y_i|} \tag{2.2}$$

Root Mean Square Roughness (R_q)

This parameter represents the standard deviation of the distribution of surface heights from the mean line and is more sensitive to large deviations from the mean line compared to the *Average Roughness (R_a)*. The mathematical and numerical formulas for this parameter are presented in Equations 2.3 and 2.4, where *l* is the evaluation length, *y(x)* is the profile height function, and y_i is the deviation from the mean line for *n* measuring points:

$$R_q = \sqrt{\frac{1}{l}\int_0^l \{y(x)\}^2 dx} \tag{2.3}$$

$$R_q = \sqrt{\frac{1}{n}\sum_{i=1}^{n} {y_i}^2} \tag{2.4}$$

The mean line here is the line that divides the profile so that the sum of the squares of the deviations of the profile height from the mean line, is equal to zero.

A disadvantage of the *Average Roughness (R_a)* and the *Root Mean Square Roughness (R_q)* is that they do not provide any type of information on the local variability of the surface profile (Santos and Julio 2013). Therefore, quite different profiles can represent the same average roughness or root mean square roughness, as seen in Figure 16 and Figure 17, respectively.

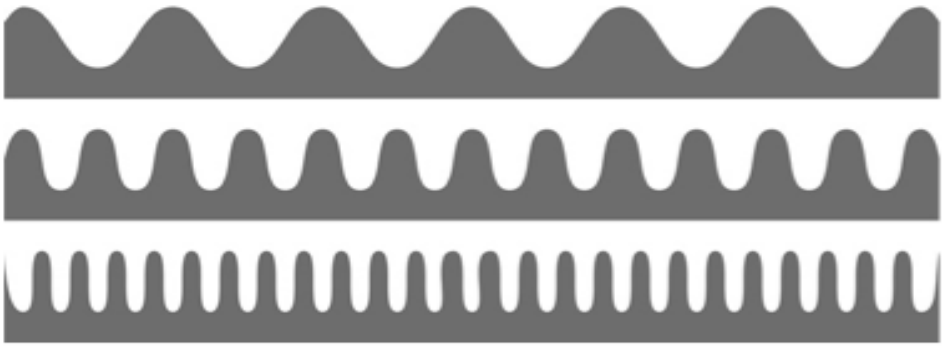

Figure 16 Different roughness profiles with the same average roughness (Santos and Julio 2013)

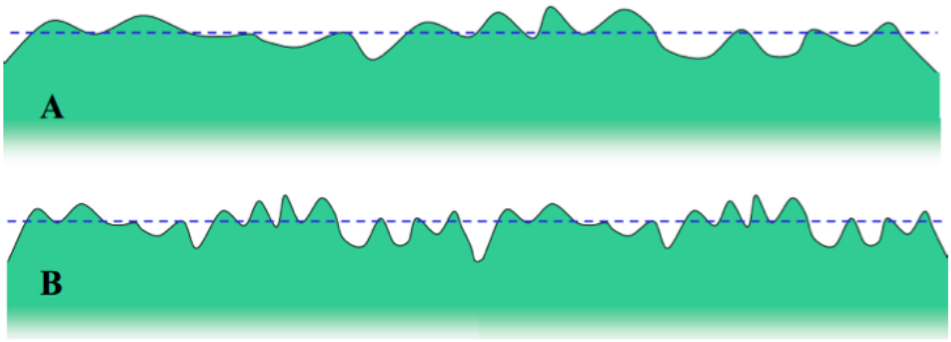

Figure 17 Different roughness profiles with the same root mean square (Rq) roughness (Bloomfield 2006)

This implies the fact that other roughness parameters are needed to characterize the surface properly. Two more profile roughness parameters, which provide a better surface description, are presented here. These are shown to have an effect on, among other factors, the contact force and the resulting abrasion rates (Tayebi and Polycarpou 2004).

Skewness (R_{sk})

The *Skewness (R_{sk})* parameter is used to measure the symmetry of the profile about the mean line. It is sensitive to occasional deep valleys or high peaks (Gadelmawla, Koura et al. 2002). Zero skewness reflects a symmetrical height distribution, i.e. with as many peaks as valleys. A positive skewness indicates a surface with a lot of peaks on a plane, while a negative skewness indicates that the surface is composed of mainly one plateau with deep and fine valleys. This is shown in Figure 18.

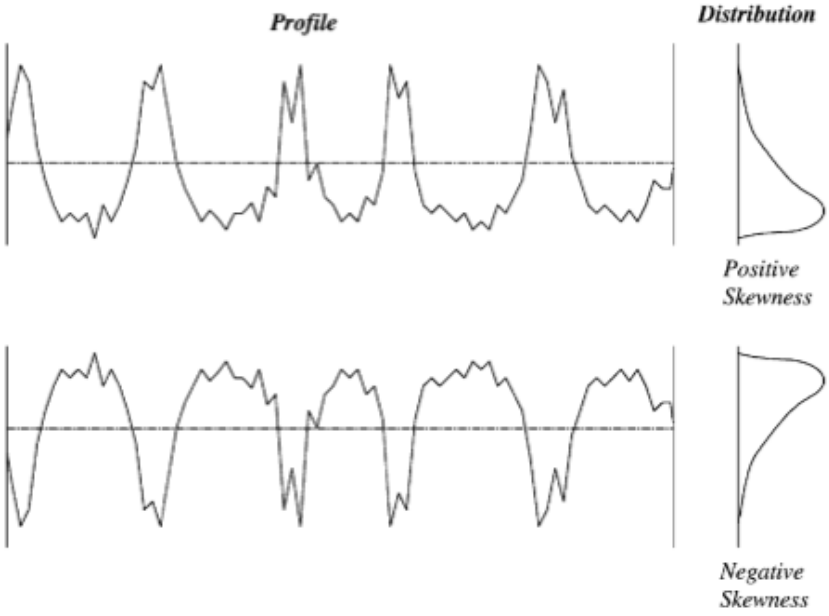

Figure 18 Definition of skewness (Rsk) on two profiles with the same average roughness (Ra) value (Gadelmawla, Koura et al. 2002)

The mathematical and numerical formulas used to calculate the skewness of a profile are presented in Equations 2.5 and 2.6, where R_q is the *Root Mean Square Roughness* and y_i is the deviation from the mean line for N measuring points:

$$R_{sk} = \frac{1}{R_q^3} \int_{-\infty}^{\infty} y^3 p(y) dy \tag{2.5}$$

$$R_{sk} = \frac{1}{N R_q^3} \left(\sum_{i=1}^{N} {y_i}^3 \right) \tag{2.6}$$

Kurtosis (R_{ku})

The *Kurtosis (R_{ku})* parameter describes the flatness of the height distribution (Leising 2010). If $R_{ku} < 3$ the surfaces will have few high peaks and low valleys, while an $R_{ku} > 3$ reflects surfaces with many high peaks and low valleys. Figure 19 illustrates these two types of kurtosis.

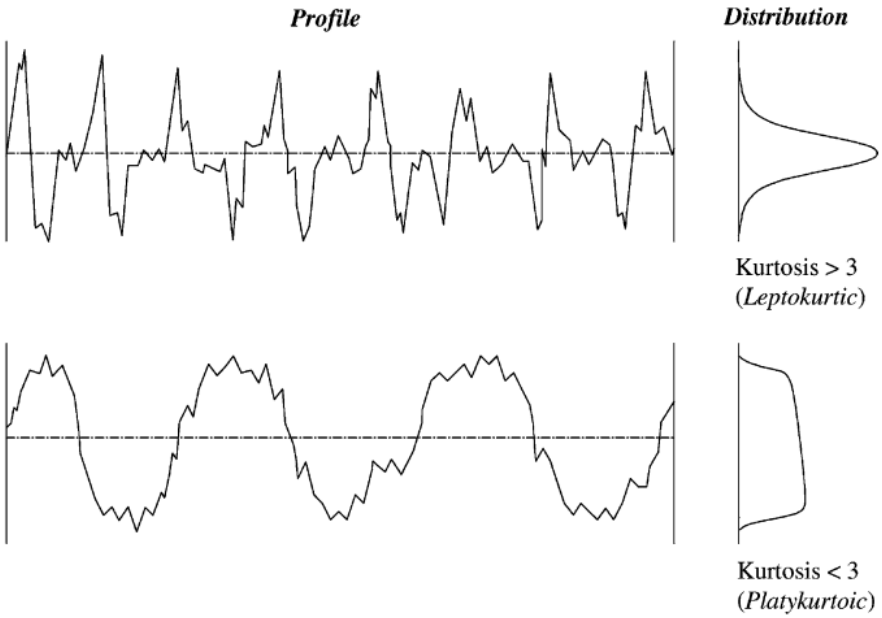

Figure 19 Illustration of the kurtosis (Rku) parameter (Gadelmawla, Koura et al. 2002)

The mathematical and numerical formulas used to calculate the kurtosis of a profile are presented in Equations 2.7 and 2.8, where R_q is the *Root Mean Square Roughness* and y_i is the deviation from the mean line for N measuring points:

$$R_{ku} = \frac{1}{R_q^4} \int_{-\infty}^{\infty} y^4 p(y) dy \qquad (2.7)$$

$$R_{ku} = \frac{1}{N R_q^4} \left(\sum_{i=1}^{N} {y_i}^4 \right) \qquad (2.8)$$

The *Skewness (R_{sk})* and *Kurtosis (R_{ku})* parameters can be used to distinguish between surfaces which have the same *Average Roughness (Ra)* value but have different shapes (Gadelmawla, Koura et al. 2002).

2.6.2 Surface Roughness Parameters

Studies have been done on the comparison of the results for roughness parameters obtained with the help of 2D profilometry and 3D profilometry. (Deleanu, Georgescu et al. 2012) did measurements on blocks of polymeric material and on external rings of tapered rolling bearings. It was found that for the parameters R_a-S_a, R_q-S_q, and R_{sk}-S_{sk}, where a capital S denotes the surface roughness (3D) value, the average values are close, but all 3D values are greater by 5-15%. Greater differences were found for R_{ku}-S_{ku}, where the 3D values were almost twice the value obtained for their 2D homologs. The conclusion of the study was that 3D parameters reflect better the topography reality than 2D parameters.

In tribology, the extreme values are important. A material like concrete, which consists of both paste and a large range of various aggregate sizes, will exhibit a large amount of extreme values. Thus, the author of this paper suggests that a 3D investigation will be more appropriate for evaluating the surface of concrete. The most common surface roughness parameters are presented in Equations 2.9-2.12. These are the *Surface Roughness Average, S_a*, the *Surface Root Mean Square Height, S_q*, the *Surface Skewness, S_{sk}*, and the *Surface Kurtosis, S_{ku}*. They are 3D parameters expanded from the profile roughness (2D) parameters. Thus, for explanations of the parameters, refer to the profile roughness parameter explanations in section 2.6.1. M and N are the number of points used for deviation measurements along the x and y-axis, and z is the deviation in height at a given point from the mean plane.

$$S_a = \frac{1}{MN}\sum_{k=0}^{M-1}\sum_{l=0}^{N-1}|z(x_k, y_l)| \tag{2.9}$$

$$S_q = \sqrt{\frac{1}{MN}\sum_{k=0}^{M-1}\sum_{l=0}^{N-1}[z(x_k, y_l)]^2} \tag{2.10}$$

$$S_{sk} = \frac{1}{MNS_q^3}\sum_{k=0}^{M-1}\sum_{l=0}^{N-1}[z(x_k, y_l)]^3 \tag{2.11}$$

$$S_{ku} = \frac{1}{MNS_q^4}\sum_{k=0}^{M-1}\sum_{l=0}^{N-1}[z(x_k, y_l)]^4 \tag{2.12}$$

2.6.3 Relationship Between Surface Roughness and Friction/Abrasion

This section includes a short review of studies that have been done regarding abrasion and the correlation between surface roughness parameters and resulting friction coefficients. The general correlation is of interest, so different materials, apart from concrete, have been included.

Although a lot of experimental work has been done in the field of surface roughness and topography of contact surfaces, the correlation between surface roughness and friction is not yet clearly defined (Sedlacek, Podgornik et al. 2009).

(Tayebi and Polycarpou 2004) relate the surface roughness parameters to the resulting contact force and static friction coefficients. They found that positive skewness values predict higher contact force, real area of contact and number of contacting asperities compared to negative skewness values. It was also found that surfaces with kurtosis values higher than three predict higher contact and friction parameters compared to kurtosis values lower than three. This is backed up by (Hertz 1881), who reported that sharper tips cause higher contact stress. Tayebi concluded that a positive skewness results in lower friction coefficient values.

(Sedlacek, Podgornik et al. 2009) studied the dry abrasion of steel and found that the sliding velocity had an influence on the coefficient of friction for the roughest steel surface. Higher sliding velocity was found to lower the friction coefficient. This might indicate that when it comes to concrete, which has a rough surface compared to steel, a higher sliding velocity will lower the friction.

In (Kirkhaug 2013), the correlation between profile roughness parameters and abrasion of concrete was studied, but no correlation was found. However, it is expected that the surface roughness parameters will give a more accurate characteristic of the concrete surface, due to the heterogeneous nature of the material. To the author´s knowledge, few or no studies have been done showing the correlation of surface skewness and kurtosis on concrete surfaces to the resulting friction coefficient and abrasion rate. This is an area that should be studied further.

These results indicate that the skewness and kurtosis values may play an important role in regard to friction and abrasion. However, the author of this paper sees a possible problem in comparing previous studies, done on other materials, on the correlation between skewness and kurtosis and abrasion rate, with concrete. Other materials, such as steel and polymers, have a more homogeneous nature than concrete, where the peaks and general surface will mainly constitute the same material. However, the peaks on a concrete surface will most likely be the aggregates, depending on their size. These, being stronger than the cement paste, can play an important role in concrete abrasion as a buffer layer between ice and cement paste. By limiting ice stress on the cement paste, this buffer layer slows down the general abrasion and reduces the mean abrasion rate (Fiorio 2005).

Keeping this in mind, one can expect that a positive skewness (many peaks) and a kurtosis value larger than three (high peaks) will have a beneficial effect on the abrasion rate of concrete.

3 Methods and Materials

This chapter describes the tested materials, test equipment, test conditions and how measurements and calculations have been performed.

3.1 Concrete Specimens and Test Program

3.1.1 Concrete Prescriptions

The concrete specimens used in this thesis were prepared in December, 2013 by SINTEF at NTNU. Test specimens were prepared from five batches of B70 concrete with different fiber additions. The following materials were used (Skjølsvold 2014):

- Norcem Anleggsement CEM I 52.5 N
- Elkem silica fume 940 U
- Årdal 0-8 mm natural sand and Årdal 8-16 mm crushed gravel (grading is given in Appendix A)
- Sika Viscocrete FB-2 water reducing agent
- Sika AER-S air entraining agent (diluted in water 1:9 before addition)

The concrete compositions are shown in Table 1. Mixing of the concrete was performed in a 100 liters Eirich forced action mixer according to the following procedure:

- One minute mixing of dry materials
- Addition of mixing water and air entrainer during one minute mixing
- Addition of water reducing admixture until approx. 100-120 mm slump measure during one minute mixing
- Two minutes rest
- One to two minutes mixing during addition of water reducing admixture until approx. 200-220 mm slump measure for Mix 1 (reference), and fiber for Mix 2-5

- Two minutes final mixing after fiber addition
- After final mixing, slump, density and air content were measured in the fresh concrete

Table 1 Concrete compositions for Mix 1-5

Mix		Mix 1	Mix 2	Mix 3	Mix 4	Mix 5
Mixing date		Dec 2nd		Dec 3rd		
Norcem	Materials in kg/m^3 concrete	427	431	431	426	424
Elkem silica fume		43	43	43	43	42
Årdal 0-8 mm sand		825	832	833	822	819
Årdal 8-16 mm gravel		894	898	889	891	888
Sika AER-S		0.030	0.031	0.031	0.030	0.030
Viscocrete FB-2		5.0	5.1	5.2	5.0	5.0
Free water[1)]		154	155	155	153	153
Dramix 3D 65/60 mm		-	39	116	-	-
Shogun BarChip 48		-	-	-	13	-
ReforceTech Minibar		-	-	-	-	28
w/c+2s		0.30	0.30	0.30	0.30	0.30
1) Including free water in the aggregates and 90% of the Viscocrete amount added						

For this thesis, steel, polypropylene and basalt fibers have been used. Mix 1 is a B70 reference concrete designed according to ISO 19906, Clause A.12.4.1.4.2, "Abrasion Tests", and is supposed to have acceptable abrasion properties. It is used as a reference concrete to evaluate the effects of the fiber additions in the other mixes. Mixes 2-5 are pretty much exactly the same as Mix 1 except that there have been fiber additions to them. Mix 2 has an addition of 0.5% volume fraction of Dramix 3D, which is a steel fiber. Mix 3 uses the same steel fiber, but with an addition of 1.5% volume fraction. Mix 4 has a 1.5% volume fraction addition of Shogun BarChip, a polypropylene fiber. The final mix, Mix 5, has a 1.5% volume fraction addition of ReforceTech Minibar 3G, a basalt fiber.

3.1.2 Fresh Concrete Properties and Casting

Density, air content and slump were all measured in the fresh concrete. The results are shown in Table 2 (Skjølsvold 2014).

Table 2 Density. air content and slump measure of concrete mixes 1-5

Mix	Mix 1 B70 reference	Mix 2 0.5% steel fibers	Mix 3 1.5% steel fibers	Mix 4 1.5% polyp. fibers	Mix 5 1.5% basalt fibers
Slump measure, mm	215	185	10	105	105
Density, kg/m^3	2355	2410	2480	2360	2365
Air content, %[1)]	5.5	3.6	1.5	3.9	4.4
1)Air content measurements for mixes with fibers(especially high steel fiber content) are probably misleading.					

3.1.3 Hardened Concrete Properties

Three cubes from each mix were tested for density and compressive strength according to EN 12390 at age 30-31 days. The results are shown in Table 3 (Skjølsvold 2014).

Table 3 Density and compressive strength of concrete mixes 1-5

Mix	Mix 1 Reference B70		Mix 2 0.5% Steel fiber		Mix 3 1.5% Steel fiber		Mix 4 1.5% Poly. fiber		Mix 5 1.5% Basalt fiber	
Density kg/m^3	2410	2410	2480	2480	2540	2560	2430	2420	2410	2420
	2410		2480		2560		2410		2420	
	2410		2490		2570		2420		2420	
Compr. strength MPa	103.4	105.7	105.1	108.7	119.4	119.8	100.9	100.4	104.8	102.4
	106.9		110.1		119.6		100.3		101.7	
	106.9		110.8		120.4		99.9		100.7	

3.1.4 Test Program and Procedures

There have been performed, in total, 20 concrete ice abrasion tests. Table 4 shows the setup and test conditions for these tests. All the tests are meant to have been performed at a temperature of -10°C and an average ice pressure of 1 MPa, although variations of these predefined values have occured, as seen in section 4.4.1. Other than that, the conditions that vary are the sliding velocity, which is either 16 cm/s or 25 cm/s, and the sliding distance, either 2500 or 5000 effective meters. Effective meters means the distance that the concrete specimen has been exposed to abrasion, and is not the same

as the distance that the abrasion rig runs. The effective distance needs to be divided by 0.37 in order to get the actual distance that the abrasion rig needs to run. This is explained in more detail in section 3.6.3.

All test specimens were stored in water at 20°C when not being tested or measured. A summary of the concrete ice abrasion test procedure and a more detailed description of how to use and operate the concrete ice abrasion rig, both taken and improved from (Kirkhaug 2013), can be found in Appendix B.

Table 4 Setup and test conditions

Setup and test conditions			
Temperature	-10°C		
Average ice pressure	1 MPa		
Sliding velocity	16 cm/s	25 cm/s	25 cm/s
Sliding distance	2500 m	2500 m	5000 m
Reference B70	2	1	1
0.5% Steel fibers	2	1	1
1.5% Steel fibers	2	1	1
1.5% Polyp. fibers	2	1	1
1.5% Basalt fibers	2	1	1
Total	10	5	5

3.1.5 Plane Cutting of Surfaces

All the concrete specimens were cut in double sizes (300*104*100 mm) and saw-cut in the NTNU laboratory, using the saw in Figure 20, to their final size, approximately 300*104*50 mm. The reason for casting them in double sizes and cutting them is to get a representative aggregate exposure on the test surface, which means that the abrasion tests were performed on the cut surfaces. If the tests were to be done on surfaces close to the molded surface, the paste content will likely be too high from what is representative for the concrete mix. After the specimens were saw-cut, they had to be plane cut, with the plane cutting equipment shown in Figure 20.

Figure 20 Saw and plane cutting equipment at NTNU

It is done by pulling a high speed rotating blade back and forth over the surface. The vertical position of the blade is manually adjusted using a handle, where one rotation of the handle equals a 0.4 mm height change. Plane cutting was performed to ensure that the top and the bottom of the specimens were parallel, as uneven specimens can give uneven abrasion over the surface. It was also done to ensure that the specimens were not too high for the ice abrasion rig. Most of the specimens were cut approximately 1-2 mm on each side, so that the final thickness of all the concrete specimens was in the range 45-47 mm.

3.2 Freeze-Thaw Testing

SINTEF carried out freeze-thaw testing according to ASTM C666 Procedure A (Rapid freezing in air and thawing in water) on separate concrete specimens. None of the specimens that went through the freeze-thaw testing were used for abrasion testing, and vice versa. This was started up after 14 days of curing in water at 20°C. The specimens were then stored in water at approximately 6°C for 3 hours prior to determination of the following initial values:

- diameter and length
- weight
- fundamental transverse frequency, according to ASTM C215, Fig 3a

The specimens were then placed in polypropylene pipes with fixed bottoms, and the pipes were filled with water. The pipe diameter was approximately 5 mm larger than the specimen diameter. The pipes were placed vertically in an automatic freeze-thaw cabinet, where the specimens were subjected to freeze- thaw cycles consisting of 3 hours in air of -22°C and 1 hour in water of 14°C. The specimens were removed from the cabinet after 160 cycles, stored for 1 hour in water at approximatey 6°C before determination of fundamental transverse frequency. The testing was terminated and the transverse frequency measured after 300 cycles.

According to ASTM C666 Procedure A, the transverse frequency is supposed to be measured at intervals not exceeding 36 cycles of freezing-and-thawing. This procedure was not followed properly due to lack of time, which is why the transverse frequency has only been measured after 160 and 300 cycles. The concrete temperature was recorded by thermocouples (cast in the specimen top and bottom mid section) on spare test specimens during exposure in the freeze-thaw cabinet (see Appendix C). The relative dynamic modulus of elasticity in percent of the initial value, is calculated from the fundamental transverse frequency according to ASTM C666 as $P_c = n^2/n_0^2$, where n_0 = initial fundamental transverse frequency and n = fundamental transverse frequency at a given number of cycles. The main results are given in section 4.2, while detailed results can be found in Appendix C (Skjølsvold 2014).

3.3 Air-void Measurements

The resistance of concrete to frost damage is largely controlled by the air void structure, including its volume, size, shape, and spacing (Fonseca and Scherer 2013). The air void content has already been measured in the fresh concrete mixes in section 3.1.2, but due to the use of fibers, these values may be misleading. Therefore, this section presents two additional methods of classifying the air void content

and structure in the hardened concrete; the PF-test and Image Analysis.

3.3.1 PF-test

Approximately 100x100x20 mm samples were saw-cut from the concrete cubes of each of the concrete mixes. Three samples were cut out from each concrete mix, resulting in 15 samples in total. The procedure is as follows, where W_x is the weight of the specimen at different stages and V is the volume (Sellevold 2008):

1. Dry the specimen at 105°C -W_1
2. Water suction > 2 days -W_2
3. Determine specimen volume -V
4. Pressure saturation, 5 MPa > 2 days -W_3

The following porosities are calculated:

$$\varepsilon_{tot} = \frac{W_3 - W_1}{V}, \quad \varepsilon_{suc} = \frac{W_2 - W_1}{V}, \quad \varepsilon_{air} = \frac{W_3 - W_2}{V}, \quad PF = \frac{\varepsilon_{air}}{\varepsilon_{air} + \varepsilon_{suc}} \tag{3.1}$$

ε_{tot} includes all pores, while ε_{suc} is assumed to include only gel- and capillary pores in the paste, i.e. those pores that can suck water directly, in contrast to the air/macro pores, ε_{air}, that only fill by overpressure. PF is the pore factor, which is the ratio between the air/macro pores and the total pores.

3.3.2 Image Analysis of Air Voids

Image analysis has been used to determine the air-void structure in the different concrete mixes. The percentage og air voids and the Powers spacing factor have been found. One sample of approximately 100x100x20 mm from each of the concrete mixes has been used for image analysis. These samples were initially plane cut using the same equipment as shown earlier in Figure 20. The samples were further polished using successively finer levels of silicon carbide powder, up to a level of 1200 grit, according to the guidelines in ASTM C457. The polishing process was finished off using a 4000 grit silicon carbide grinding paper. The quality of the polish was considered

acceptable if the reflectivity of the surface was uniform and there was an absence of striations from the grinding paper (Fonseca and Scherer 2013). The edges of the air voids are to be sharp, not rounded or crumbled. To remove eventual sand particles from the surface pores, the samples were placed in a UV pool for a duration of 2 hours.

The polished surfaces were then blackened using an Edding 850 permanent marker. The next step of the process was to fill the air voids with a barium sulfate powder with an average particle diameter of 1-4 micron. This was done by hand, basically using the fingers to press the powder into the air voids and to wipe the excess powder off of the surface. An example of a basalt fiber concrete surface, before and after preparation, can be seen in Figure 21. After this process, the surface needs to be studied using a stereoscopic microscope to make sure all the pores are filled with the barium sulfate powder, and that no excess powder is left on the surface. The final result is a black background with white air void profiles, as seen to the right in Figure 21.

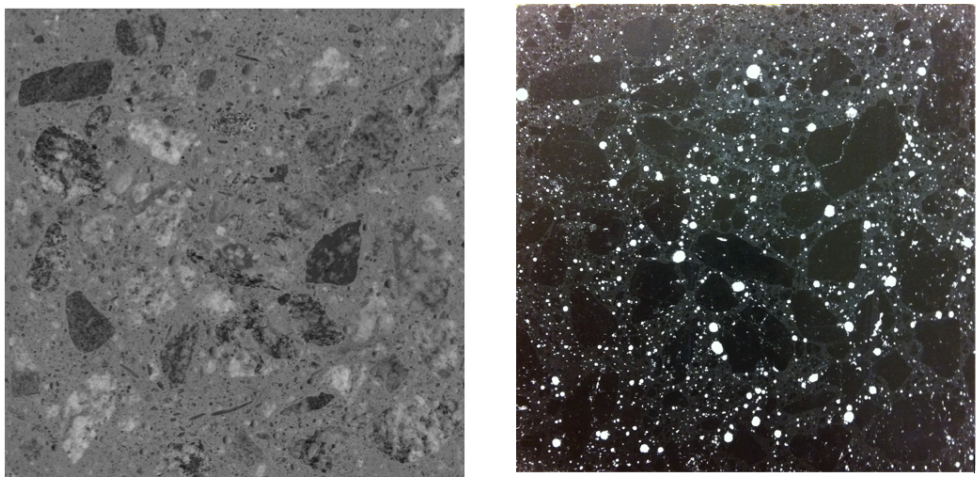

Figure 21 Basalt fiber concrete surface before and after preparation for image analysis

The samples are then scanned at 1200 dpi using an ordinary flatbed scanner. Using a MATLAB program developed by (Fonseca and Scherer 2013), these scans are processed into binary images, where black pixels represent background paste/aggregate and white pixels represent air voids. Using stereological methods, the program

approximates 3D quantities of interest from the 2D scans. The determined quantities are the total volumetric air content, the Powers spacing factor, $\bar{L}$, the specific surface and the approximate size distribution of the air voids.

3.4 NTNU Concrete Ice Abrasion Laboratory

The ice abrasion rig used for this study has been built at NTNU. A description of the rig and a short guide of how to operate it has been presented in (Kirkhaug 2013). This section offers an improved version of this description and guide, partly due to modifications performed to increase the stiffness of the base plate. A more detailed description, also taken and improved from (Kirkhaug 2013), is found in Appendix B.

The ice abrasion test rig is placed in a cold-storage chamber and consists of three main parts; the ice abrasion rig, a heating circulator and a control unit. Temperature of the storage room is regulated by a refrigerating system, controlled by a Pego 2000 Expert control unit, making temperatures as low as -20°C possible. Due to the test conditions for the tests done in this thesis, the temperature in the chamber was set at -10°C for the entire testing period.

In the ice abrasion rig, the concrete specimen is placed so that there is approximately 2 mm between the concrete specimen and the ice specimen cylinder. If the distance is larger, some steel plates with different thicknesses can be used to lift the concrete specimen a bit. The ice specimen cylinder can be seen in orange in Figure 22. Ice specimens are placed inside the cylinder before testing.

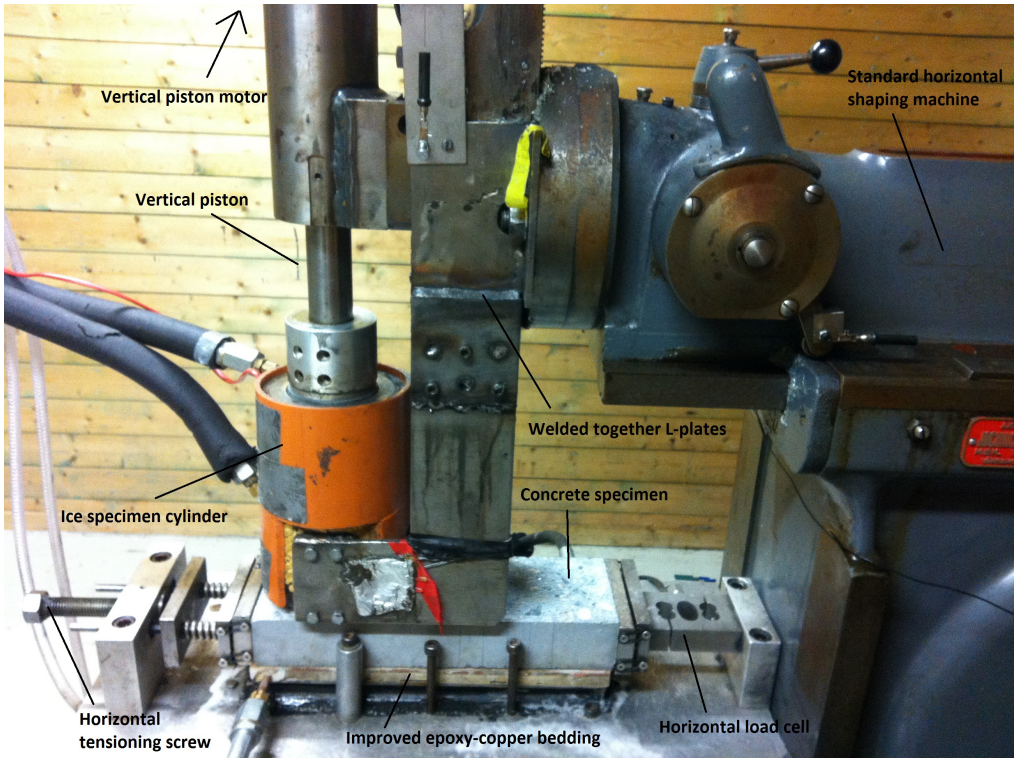

Figure 22 NTNU Concrete Ice Abrasion Rig

The rig applies the load in Newton, and the desired contact force is calculated by multiplying the surface area of the ice specimen with desired pressure. The original ice diameter is 70 mm, but when force is placed on the ice it expands to the diameter of the ice specimen cylinder, which is 74 mm. This expansion results in the surface area of the ice specimens being 4299 mm^2. Since all the tests in this thesis used an average ice pressure of 1 MPa, the load was constantly set at 4299 N.

The load is controlled by a vertical piston that pushes the ice down on the concrete surface. Two vertical load cells, underneath the copper bedding, record the load and send it to the Labview program on the laboratory computer. Then the Labview program automatically adjusts the vertical position of the piston to obtain and maintain the desired load on the concrete surface. The vertical gain and vertical speed control how quickly the piston is adjusted. All settings are controlled in Labview. For the tests in this study, the vertical speed was set to 600 rpm and vertical gain to 0.02 mm. The

vertical piston can be seen in Figure 22 just above the orange ice specimen cylinder.

A standard horizontal shaping machine with a stroke length of 200 mm carries out the horizontal movement. The concrete specimen is tensioned horizontally to keep it in place and in order to compute friction data. A horizontal load cell, seen to the bottom right in Figure 22, is used to register the horizontal load and calculate the friction between the ice and the concrete surface.

Between the concrete specimen and the vertical load cells is a copper plate. Improvements have been made to this copper plate since the abrasion rig was used by (Kirkhaug 2013). Kirkhaug experienced that some of his concrete specimens cracked before the desired abrasion distance was reached. It was concluded that this was due to a too high deformation caused by the bending moment applied on the concrete. The reason for this deformation was believed to be because of the copper plate being too soft. Therefore, improvements have been made to make the system stiffer, as explained in the following.

The copper parts in the abrasion rig are put together as a "sandwich". This "sandwich" consists of a copper plate, on which the concrete sample rests, a copper coil beneath the copper plate, and a steel plate at the bottom. The copper coil is soldered to both the copper and steel plate, and transfers heat from the flow of alcohol that is controlled by a heating circulator. The empty space between the coil tubes in the "sandwich" was believed to be the reason for why it was not stiff enough. During earlier measurements it was possible to actually see the concrete specimen bending due to the lack of stiffness in the system.

The solution to stiffen the system and, hopefully, at the same time maintain the same experimental conditions, was to fill the empty space in the "sandwich" with epoxy, shown in Figure 23 (Greaker 2013). Another measure that was carried out in order to stiffen up the system as a whole, was to weld together the L-plates holding the ice specimen cylinder. This improvement to the abrasion rig is seen as successful seeing that none of the concrete specimens cracked during the testing in this thesis.

Further improvements to the ice abrasion rig that have been carried out since Kirkhaug used it, are the installment of a motor for the

horizontal movement of the table on which the concrete specimen lies, and the replacement of a new motor for the vertical piston generating the vertical force from the ice on the concrete surface. This last motor was changed to a bit more powerful motor because of previous problems of it overheating.

Figure 23 Improved epoxy-copper bedding

The copper "sandwich" is placed on top of sliding bearings, which have the purpose of reducing friction in the system. Both the copper plate and the ice specimen cylinder are connected to a heating circulator, a Julabo 2000. This device circulates alcohol, when the gauges are opened, through either the copper plate or the ice specimen cylinder, or both. The temperature of the circulated alcohol is controlled manually. The reason for heat circulation through the copper plate is to keep the surface of the concrete specimen at a temperature that will prevent the freezing of ice on the surface. If ice freezes on the concrete surface it will have a protective effect, resulting in ice sliding against ice and minimized abrasion values (Nawwar and Malhotra 1988). The effect on the temperature variation in the concrete specimen due to the stiffening of the system with epoxy has been investigated and the results are presented in section 4.4.1.

The copper plate and ice specimen holder, with their connections to the heating circulator, and the heating circulator can be seen in Figure 24 and Figure 25, respectively. A temperature of 11°C from the heating circulator was found to be the correct temperature for the specimens used in this study. This resulted in a temperature on

the concrete surface just above 0°C, which prevented water from freezing on the surface. The reason why the heating circulator is also connected to the ice specimen cylinder is to make it easier to remove the ice after abrasion. A gauge can be opened when the time is in to remove the ice. It is important to close the gauge again when the ice has been removed in order to keep the temperature in the ice specimen cylinder as low as possible. Seeing that the heating circulator is connected to both the copper bedding and the ice specimen cylinder, it cannot be used to keep low temperatures in the ice specimen cylinder at the same time as it heats up the copper bedding. An extra heating circulator can be connected for this purpose if desired.

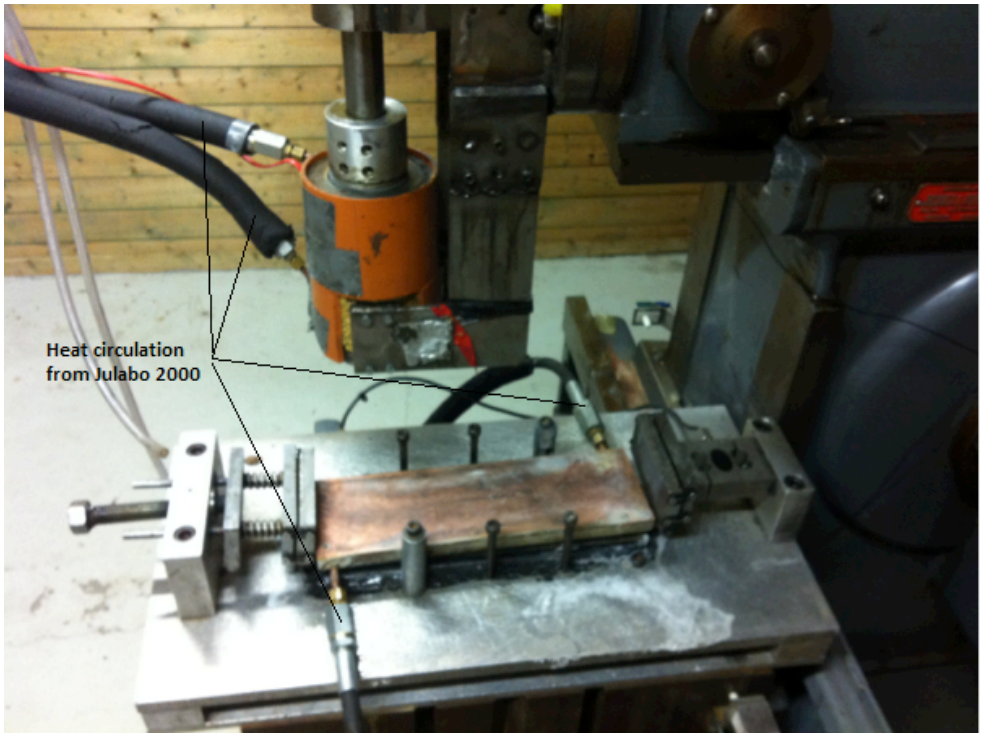

Figure 24 Copper plate and ice specimen holder with connections to the heating circulator

Figure 25 Julabo 2000 heating circulator

The Labview program constantly records data from the load cells during testing. How often Labview records data can be adjusted manually in the program, the options being either once per cycle or in the range 1-10 Hz. Table 5, taken from (Kirkhaug 2013), shows how parameters are controlled and what data that is logged by Labview.

Table 5 Parameters and data logged by Labview (Kirkhaug 2013)

Function	Controlled by	Logged by Labview
Horizontal sliding velocity	Labview	Yes
Vertical load (average ice pressure)	Labview	Yes
Velocity of vertical pressure adjustment	Labview	Yes
Automatic adjustment to keep constant pressure	Labview	Yes
Automatic stop when ice has to be changed	Labview	Yes
Ambivalent air temperature	Pego refrigerating control unit	Yes
Concrete surface temperature	Julabo 2000	Yes*
Ice cylinder temperature	Julabo 2000/Room temperature	No
Pretension of the concrete specimen	Manual	Yes
Horizontal force, friction	--	Yes
Automatic stop after given ice sliding distance	Labview	Yes
Horizontal position of the ice cylinder	Labview	Yes
***If temperature sensors are casted in the concrete specimen**		

The data files are automatically logged on the laboratory computer under E:Isabrasivmaskin-V3. The files from the experiments in this thesis are stored in the same location, in the folder "Kristian Sætre sin Masteroppgave", for potential future use.

3.5 Preparation of Ice Specimens

The ice that has been used in the abrasion tests is made of tap water, even though, realistically, concrete structures will most likely undergo abrasion by sea ice. (Hara F. 1995) and (Itoh, Tanak et al. 1994) both did studies where they found small differences in abrasion from sea ice and freshwater ice for temperatures larger than -10°C. Another argument for using freshwater ice instead of sea ice is to avoid unwanted maintenance due to corrosion on the ice abrasion rig.

The ice is made in plastic cylinders with an inner diameter of 70 mm and a height up to 180 mm, as shown in Figure 26. These are filled with tap water and placed in a cold storage chamber, the same room as the ice abrasion rig, where the temperature is -10°C. A minimum

of 24 hours in the room is necessary for the ice to freeze properly. When the ice has frozen properly, the plastic cylinders are placed in room temperature for approximately 45 minutes, until it is possible to slide the ice out of the cylinders. The ice specimen is then placed back in the ice abrasion laboratory. Using this method, the ice freezes from all directions simultaneously, resulting in what is classified as granular ice. The surface of the ice is the first to freeze, trapping in all the air bubbles that are in the water at that time. Then the ice freezes inwards, pressing all the air to the center of the cylinder. This results in a concentrated air pocket in the center of the cylinder, which can be seen clearly to the right in Figure 26.

Figure 26 Ice specimens used for the abrasion testing

Since the ice freezes without letting any air escape, it is expected to have a slightly lower density than the theoretical density of ice, which is 917 kg/m^3. (Kirkhaug 2013) used the same procedure of making ice and measured the density to be 913 $\pm$ 17 kg/m^3. His method of measuring the ice density, however, was based on submerging the ice specimens in water, which can lead to water freezing on the surface of the ice during the time that the measurements are being performed. (Greaker 2013) used a more accurate method of measuring the density of the ice specimens. Instead of submerging the specimens in water, they are submerged in a container filled with oil lamp kerosene that has been cooled down to a temperature below 0°C. The density of the kerosene was continuously measured with an aerometer, and the mass of the ice

was measured with a Kern 572 weighing scale with an accuracy of 0.01g. The mass of the ice was first measured hanging in the air and then submerged in the kerosene, using a custom-made holder. Equation 3.2 shows the formula used for the ice density calculations which is based on Archimedes law, but accounted for the added mass and volume from the holder.

$$\rho_{ice} = \frac{m_{ice+holder,air} - m_{holder,air}}{m_{ice+holder,air} - m_{ice+holder,ker} - \rho_{ker} V_{holder}} \rho_{ker} \qquad (3.2)$$

$M_{ice+holder,air}$ is the mass of the ice and the holder, $m_{holder,air}$ is the mass of just the holder, $m_{holder,ker}$ is the mass of the holder submerged into kerosene, ρ_{ker} is the kerosene density and V_{holder} is the volume of the holder. The derivation of Equation 3.2, done by (Greaker 2013), is presented in Appendix D. The ice porosities are also calculated using Equation 3.3.

$$P_{ice} = 1 - \frac{\rho_{ice,measured}}{\rho_{ice,theoretical}} \qquad (3.3)$$

3.6 Concrete Ice Abrasion Measurements

3.6.1 Measuring Equipment and Procedures

Due to lack of time, only one of the measuring methods explained in section 2.5 has been used for surface measurements. A Mitutoyo 543-250B digital indicator, shown in Figure 27, has been used for the abrasion measurements. This device has an accuracy of 0.003 mm and can measure deviations in the range of 0-12.7 mm with a load of 1.5 N (Mitutoyo 2005). Deviations on this digital indicator have to be recorded manually. The principal of this measuring method is described in section 2.5.1.

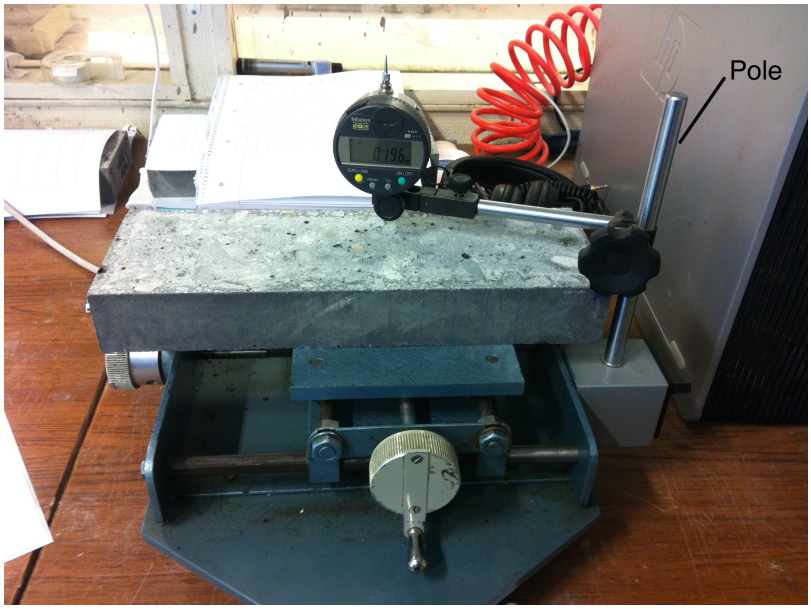

Figure 27 Mitutoyo 543-250B digital indicator

Abrasion measurements have been done before abrasion, after 1.25 km effective sliding distance, and after 2.5 km effective sliding distance. For the specimens that were tested 5 km, measurements were also taken after 3.75 km and after 5 km. Two measurements have been taken and averaged at each mentioned interval to increase the accuracy of the measurements. The measurements were done by placing the concrete specimen on a coordinate table, as shown in Figure 27. The coordinate table is originally made for manual point counting of air voids, according to ASTM C457, and is not made for such large specimens. However, a method was derived to make it possible to measure the entire surface, except for the center axis, y=0 on Figure 28.

It is very important that the specimens are aligned in exactly the same way for each measurement, so that the measuring points are the same each time. The specimens were always placed on the coordinate table with their back edge aligned with the back edge of the table. To be able to align them in the same way for each measurement in the other direction (along the y-axis in Figure 28), lines were drawn on the edges of the specimen, with one line being aligned with the edge of the table and another line where the measurements were to start (20 mm from the center). Half of the specimen was first measured, then rotated to measure the next half.

The reason for the specimen having to be rotated is because the pole that the digital indicator is connected to comes in the way of the specimen, as seen in Figure 27. This is also the reason why no measurements have been done in the y=0 axis. The coordinate table has two handles that either move the table back and forth, along the x-axis, or from side to side, along the y-axis. One rotation on either of the handles equals 1 mm movement. The measuring table needs to be greased every once in a while. If this is not done, vibrations can occur while rotating the handles which will result in movements of the concrete specimen on the table. The measuring grid with the used coordinate system can be seen in Figure 28, where the abraded zone of the concrete is colored blue.

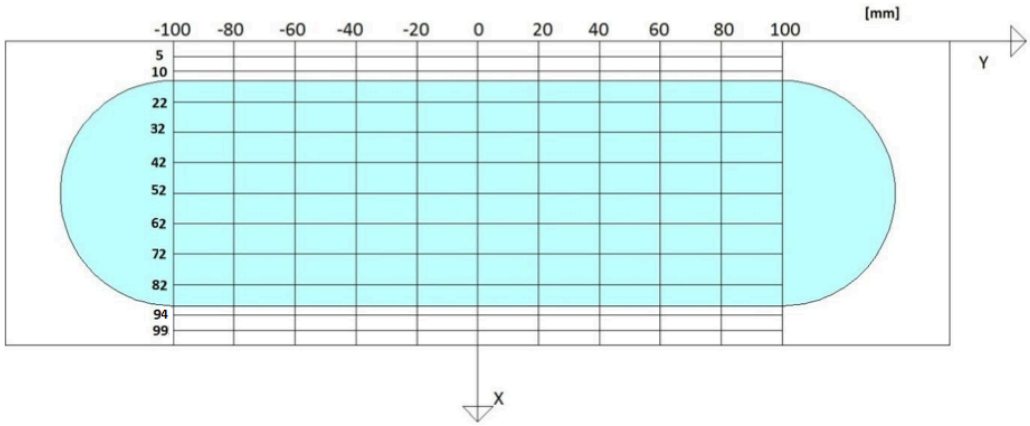

Figure 28 Measuring grid and coordinate system, modified from (Kirkhaug 2013)

As explained above, the concrete specimen was aligned with its back edge along the back edge of the coordinate table. This means that the entire concrete specimen in the x-direction is lying on the coordinate table. The first five specimens that were measured, specimens 1.1, 11.1, 21.1, 31.1 and 41.1, used a different method, referred to in this thesis as the old method. This method allowed the entire surface to be measured, including the y=0 axis, but it had part of the concrete specimen in the x-direction outside the coordinate table. In other words, the back edge of the concrete specimen was not aligned with the back edge of the coordinate table, but was moved a bit off of the table. This measuring method was found to be inaccurate as the concrete specimen would not lie flat on the coordinate table, but tended to tilt a bit off of the table. It was not possible to notice this effect with the naked eye, but the measurements showed this tendency clearly, resulting in very inaccurate measurements.

Therefore, it is important to keep in mind that the concrete specimen has to be placed fully on the measuring table along the x-axis, and as centered as possible, without the pole getting in the way during measurements, along the y-axis.

Figure 29 shows the scheme that was used for each individual surface measurement, with a total of 110 measuring points. For the first measurement of each of the halfs of the specimen, the digital indicator was reset to 0, as seen in the scheme. Since the specimens were 104 mm wide, the two measurements closest to each edge are both 5 mm from the edge. The next measuring point is 5 mm further in towards the center of the specimen. Both of these measuring points closest to the edge, colored in red and blue in Figure 29, are used as reference points when measuring the abrasion, since they are outside of the abrasion zone, as seen in Figure 28.

X/Y	-100	-80	-60	-40	-20	0	20	40	60	80	100
5					0.000						
10											
22											
32											
42											
52											
62											
72											
82											
94											
99							0.000				

Figure 29 Measuring scheme with coloured reference points

From these surface measurements, the abrasion was calculated using an Excel spreadsheet and four different calculation methods, Methods 1-4, presented in section 3.6.2. In order to explain these different methods in an understandable manner, an example is shown of the measurements done on one of the specimens before abrasion. Six measurements of specimen 2.2 were performed, all before any abrasion was undergone, in order to study the accuracy of the measuring equipment. The optimal result from these measurements would be that they were all exactly the same. Of course, due to an inaccuracy in the equipment and also an inaccuracy of the person

using the equipment, this was not the case. A standard deviation of 0.0059 mm was found as an average for each measuring point. Tables 6-8 show three of these measurements done on specimen 2.2.

Table 6 Measurement 1 on Specimen 2.2 (mm)

X/Y	-100	-80	-60	-40	-20	0	20	40	60	80	100
5	0.201	0.123	0.083	0.031	0.000		-0.024	-0.076	-0.091	-0.109	-0.096
10	0.253	0.164	0.119	0.054	0.026		-0.028	-0.037	-0.061	-0.083	-0.069
22	0.333	0.241	0.170	0.112	0.075		0.058	0.009	-0.008	-0.044	-0.023
32	0.383	0.285	0.219	0.155	0.101		0.097	0.044	0.016	-0.009	0.003
42	0.419	0.310	0.234	0.155	0.108		0.107	0.063	0.036	0.004	0.004
52	0.438	0.328	0.247	0.169	0.111		0.127	0.063	0.037	0.004	0.002
62	0.442	0.331	0.246	0.160	0.097		0.113	0.062	0.036	-0.003	-0.007
72	0.431	0.317	0.226	0.132	0.078		0.103	0.047	0.010	-0.033	-0.039
82	0.418	0.283	0.200	0.103	0.039		0.074	0.012	-0.044	-0.072	-0.086
94	0.367	0.244	0.156	0.051	-0.016		0.035	-0.046	-0.089	-0.136	-0.150
99	0.343	0.220	0.126	0.031	-0.041		0.000	-0.067	-0.135	-0.170	-0.192

Table 7 Measurement 2 on Specimen 2.2 (mm)

X/Y	-100	-80	-60	-40	-20	0	20	40	60	80	100
5	0.209	0.138	0.087	0.038	0.000		-0.009	-0.066	-0.080	-0.098	-0.081
10	0.264	0.184	0.127	0.064	0.032		-0.029	-0.026	-0.050	-0.070	-0.057
22	0.340	0.253	0.181	0.123	0.080		0.062	0.023	0.005	-0.031	-0.011
32	0.396	0.293	0.232	0.170	0.111		0.102	0.057	0.027	0.003	0.016
42	0.433	0.321	0.245	0.166	0.119		0.110	0.067	0.044	0.024	0.019
52	0.452	0.342	0.260	0.182	0.124		0.129	0.077	0.047	0.022	0.014
62	0.459	0.344	0.265	0.176	0.111		0.114	0.072	0.047	0.000	0.003
72	0.451	0.330	0.245	0.155	0.097		0.104	0.059	0.021	-0.030	-0.029
82	0.436	0.305	0.218	0.130	0.061		0.076	0.022	-0.036	-0.055	-0.076
94	0.389	0.265	0.177	0.072	0.003		0.038	-0.034	-0.078	-0.125	-0.139
99	0.367	0.245	0.149	0.053	-0.024		0.000	-0.054	-0.123	-0.159	-0.179

Table 8 Measurement 3 on Specimen 2.2 (mm)

X/Y	-100	-80	-60	-40	-20	0	20	40	60	80	100
5	0.216	0.143	0.093	0.039	0.000		-0.024	-0.072	-0.090	-0.105	-0.093
10	0.267	0.181	0.131	0.062	0.037		-0.015	-0.034	-0.060	-0.082	-0.066
22	0.346	0.250	0.185	0.122	0.088		0.059	0.011	-0.005	-0.043	-0.022
32	0.395	0.300	0.235	0.170	0.117		0.099	0.051	0.018	-0.004	0.005
42	0.436	0.322	0.251	0.163	0.121		0.111	0.060	0.039	0.004	0.009
52	0.457	0.344	0.256	0.181	0.126		0.124	0.068	0.042	0.007	0.004
62	0.466	0.351	0.261	0.179	0.119		0.115	0.064	0.039	0.001	-0.007
72	0.457	0.336	0.245	0.157	0.101		0.106	0.046	0.011	-0.030	-0.037
82	0.441	0.314	0.221	0.135	0.064		0.078	0.014	-0.043	-0.068	-0.082
94	0.391	0.269	0.179	0.079	0.009		0.038	-0.042	-0.085	-0.135	-0.150
99	0.370	0.251	0.153	0.065	-0.012		0.000	-0.065	-0.131	-0.170	-0.189

3.6.2 Abrasion Calculation Methods

A systematical error in the measuring equipment was discovered after doing these measurements of specimen 2.2. It was found that if the reference point increased in one measurement compared to the previous, then the other points in the same axis as the reference point also tend to increase with approximately the same amount. Take axis y=-100 in measurements 1 (Table 6) and 2 (Table 7) for example. The points in axes x=5 and x=99 both increase from measurement 1 to measurement 2. The first point has an increase of 0.008 mm while the last point has an increase of 0.024 mm. Further, the points in axes x=10 and x=94 have increases of 0.011 mm and 0.022 mm, respectively. These differences seem to close in on each other towards the center, axis x=52, where the difference is 0.014 mm between measurement 1 and 2. This trend is seen on just about every axis in each measurement, and is therefore classified as a systematical error. Because of this systematical error, the calculation of the abrasion becomes a bit complicated, and four different methods have therefore been established.

In Method 1 (which is the same as Method 2 in (Greaker 2014)), the difference is found from each point in the abrasion zone to its nearest reference point colored in red in Figure 29. This means that the points in axes x=22,32,42 and 52 (Figure 28) all are subtracted from the reference points in axis x=5, while the points in axes x=62,72 and 82 are subtracted from the reference points in axis x=99. This is done separately for each y-axis and these measurements are done before, during and after abrasion. The difference in these differences

before and after abrasion for each point is the abrasion depth. The abrasion depth of all the measuring points is averaged over the entire specimen and this results in the abrasion value of the specimen. This value is then divided by the effective sliding distance to give the abrasion rate (mm/km).

Method 2 is exactly the same as Method 1, except that this time the blue reference points in Figure 29 are used instead of the red ones.

Method 3 uses both the red and blue reference points. In this method an average of all of the reference points is found. Then the difference from this average and each of the points in the abrasion zone is calculated. This is done before, during and after abrasion, and the difference in these differences for each point between measurements is the abrasion.

Method 4 is the method used in (Kirkhaug 2013) to calculate the abrasion. This method is similar to Method 1 and 2, just that only the reference points in axis x=5 are used. The difference between each point in the abrasion zone and the point in the same y-axis and in axis x=5 is calculated. This is done before, during and after abrasion, and the difference in these differences for each point between measurements is the abrasion.

These calculation methods all give different abrasion values and it is hard to know which one is the most accurate. The correlation between some of these different methods is shown in Figures 32-34. In section 0, the abrasion rate is presented for each method in Table 13 and Figure 31, but for the rest of the results, except for the wear profiles in section 4.4.3, an average of the abrasion rates calculated using methods 1 and 2 is used. These are believed to give the most accurate abrasion results due to the systematic error in the measuring equipment mentioned above.

3.6.3 Measurement Adjustments

Due to the fact that the diameter of the ice cylinder is 74 mm, while the stroke length of the abrasion rig is 200 mm, it is necessary to adjust the accumulated horizontal distance values given in Labview to obtain the effective sliding distance. By dividing the ice cylinder diameter with the stroke length of the rig, the effective ice exposure at a given point of the surface is found: $\frac{D}{l} = \frac{74}{200} = 0.37$. This means

that for each meter the abrasion rig runs, each point on the concrete surface is just experiencing 37 cm of abrasion. So for the specimen to be subject to, for example, 2500 effective meters, the abrasion rig has to run a total of 2500/0.37=6757 meters.

This adjustment is only valid for the center of the concrete specimen, at x=52 mm, where the diameter of the ice is 74 mm. Due to the fact that the ice specimen is cylindrical, not all of the surface of the concrete will experience the same amount of abrasion. The rest of the measuring points have to be further calibrated for the minimizing chord length the further they are from the center. (Kirkhaug 2013) has calculated the chord length at each of the measuring points using the theorem of Pythagoras. As an example, 30 mm from the center the chord has just 58% of the length as in the center(diameter). Figure 30, taken from (Kirkhaug 2013), illustrates the calculations of the chord length, where R=radius, D=diameter, d(x)=distance from the centerline to the chord, k=length of half of the chord, and C(d)=cord length as a function of d(x). Table 9 shows the chord adjustment factors. Multiplying these factors with the effective sliding distance at the concrete center (x=52 mm), gives the effective sliding distance at each measuring point, depending on which x-axis the measuring is located on.

$$R = Radius = \frac{Diameter}{2} = \frac{74}{2} = 37\ mm$$

$$k = \sqrt{R^2 - d(x)^2}$$

$$C(d) = 2 * k = 2 * \sqrt{R^2 - d(x)^2} = 2 * \sqrt{37^2 - d(x)^2}$$

$$Calibration\ parameter, chord = \frac{C(d)}{D}$$

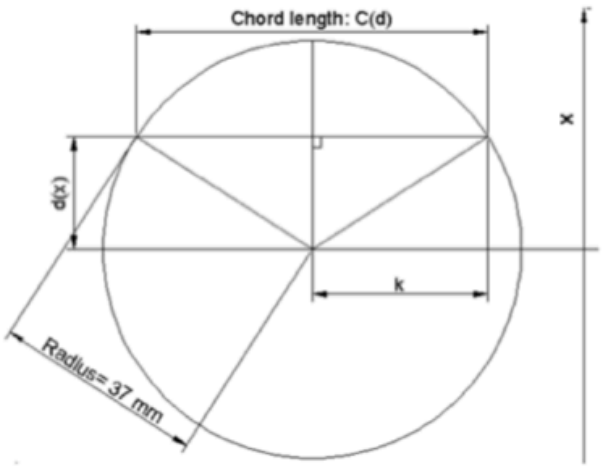

Figure 30 Calculations of the chord length (Kirkhaug 2013)

Table 9 Chord adjustment factors

X-coordinate	Distance from	Chord adjustment
5	47	0
10	42	0
22	30	0.59
32	20	0.84
42	10	0.96
52	0	1.00
62	-10	0.96
72	-20	0.84
82	-30	0.59
94	-42	0
99	-47	0

3.6.4 Roughness Calculations

The *Surface Roughness Parameters,* presented in Equations 2.9-2.12, are calculated for each of the specimens, before and after abrasion. This is done manually in Microsoft Excel using the measuring points in the abraded area of the concrete specimen. The same measurement data is used for roughness calculations as for the abrasion calculations. The average of all the points is first calculated, and then the differences between each point and this average is determined. This gives us the deviations from the mean plane, the z-values in the surface roughness equations. Using these z-values, the parameters S_a, S_q, S_{sk} and S_{ku} are calculated.

4 Results

4.1 Ice Densities

The densities and porosities of 10 different ice specimens that have been calculated using Equations 3.2 and 3.3 are shown in Table 10. The data for these calculations are presented in Appendix E.

Table 10 Ice specimen densities

Sample #	Density (kg/m^3)	Porosity (%)
1	904.83	1.43
2	904.38	1.48
3	903.31	1.61
4	904.69	1.45
5	902.96	1.64
6	904.07	1.52
7	901.97	1.75
8	903.64	1.57
9	903.71	1.56
10	903.15	1.62

These measurements give an average ice density of 903.7 kg/m^3 with a standard deviation of 0.9 kg/m^3 and an average porosity of 1.56%. Compared to the theoretical density of ice, 917 kg/m^3, this indicates that the ice used in these experiments is a bit weaker than natural freshwater ice.

4.2 Freeze-Thaw Testing

Table 11 shows the results from the freeze-thaw testing done by SINTEF. The relative dynamic modulus of elasticity has been reduced to less than 60% after 300 cycles for all of the concrete mixes, which means that none of the concrete mixes have survived the freeze-thaw exposure. Photos taken by SINTEF of the different concrete mixes after 300 freeze-thaw cycles can be seen in Appendix F.

Table 11 Relative dynamic modulus results from freeze-thaw testing

Transverse frequency measured after n cycles	Mix 1	Mix 2	Mix 3	Mix 4	Mix 5
	Relative dynamic modulus, $(n^2/n_0^2) \cdot 100$ (%)				
n=0	100	100	100	100	100
n=160	33	32*	45	42*	51
n=300	20*	38*	48	45*	19*

*One specimen only, no result for the second specimen.

4.3 Air-void Measurements

Air-void measurements in the fresh concrete and in the hardened concrete, using both the PF-method and image analysis, have been performed. Table 12 presents the results from these tests, including the PF value, Powers spacing factor, $\bar{L}$, and the specific surface, α. Refer to Appendix G for the detailed PF-test data.

Table 12 Air-void measurement results

Product type	% air measured in fresh concrete	% air from PF-method	PF-value (%)	% air from image analysis	Spacing factor $\bar{L}$ (mm)	Specific surface α (mm^{-1})
1. B70 reference	5.5	3.1	22.1	4.1	0.30	18.3
2. 0.5% steel	3.6	2.4	17.6	3.7	0.28	20.9
3. 1.5% steel	1.5	1.8	13.6	3.8	0.22	27.5
4. 1.5% poly.	3.9	2.7	19.1	3.7	0.33	18.0
5. 1.5% basalt	4.4	3.7	24.4	4.6	0.32	16.6

4.4 Concrete Ice Abrasion Testing

In total, 20 specimens, water cured for 2-3 months and not exposed to freeze-thaw tests, have undergone the concrete ice abrasion testing. Due to a large amount of data from these experiments, only the most relevant and important results are presented here.

Abrasion Rate.

Table 13 and Figure 31 present the average abrasion rates using Methods 1-4. This is just to give an idea of the differences in abrasion rates calculated using the different calculation methods presented in section 3.6.2. All of the results presented in this chapter, except for the wear profiles in section 4.4.3, will be using an average of Methods 1 and 2.

Table 13 Average abrasion rates using Methods 1-4

Product type	Specimen number	Sliding velocity (cm/s)	Abrasion rate(mm/km) Method 1	Abrasion rate(mm/km) Method 2	Abrasion rate(mm/km) Method 3	Abrasion rate(mm/km) Method 4
B70 Reference	1.1*	16	-0.003	-0.004	-0.003	-0.002
	1.2	16	0.006	0.004	0.006	0.001
	2.1	25	0.013	0.009	0.011	0.013
	2.2	25	0.002	0.001	0.002	0.000
0.50% Steel	11.1*	16	0.001	0.001	0.000	0.010
	11.2	16	0.007	0.004	0.006	0.002
	12.1	25	0.003	0.001	0.002	0.003
	12.2	25	0.004	0.002	0.002	0.006
1.50% Steel	21.1*	16	-0.004	0.000	-0.002	-0.003
	21.2	16	0.007	0.006	0.007	0.003
	22.1	25	0.009	0.009	0.010	-0.005
	22.2	25	0.007	0.006	0.006	0.010
1.50% Polypr.	31.1*	16	0.005	0.002	0.003	0.005
	31.2	16	0.011	0.000	0.005	0.007
	32.1	25	0.008	0.005	0.007	0.001
	32.2	25	0.003	0.004	0.004	0.003
1.50% Basalt	41.1*	16	-0.002	-0.002	-0.002	0.002
	41.2	16	0.005	0.004	0.004	0.004
	42.1	25	-0.006	-0.006	0.001	-0.059
	42.2	25	0.004	0.002	0.003	0.001

*Specimens measured using the old measuring method.

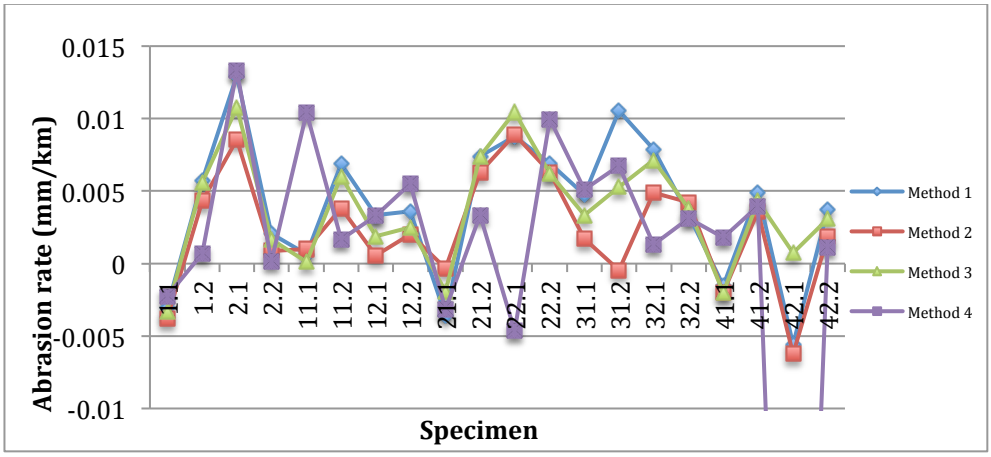

Figure 31 Abrasion rates for calculation methods 1-4

To get a better idea of how these different calculation methods are correlated to each other, the correlation between some of the methods have been plotted, as seen in Figures 32-34.

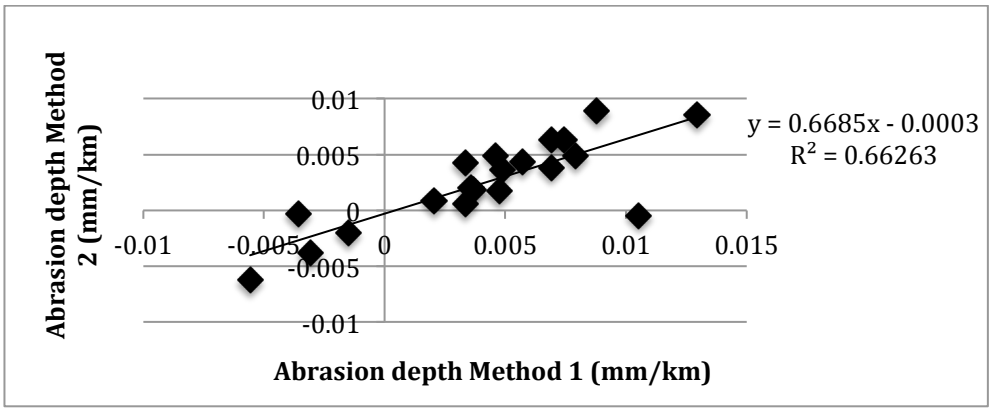

Figure 32 Correlation between calculation method 1 and 2

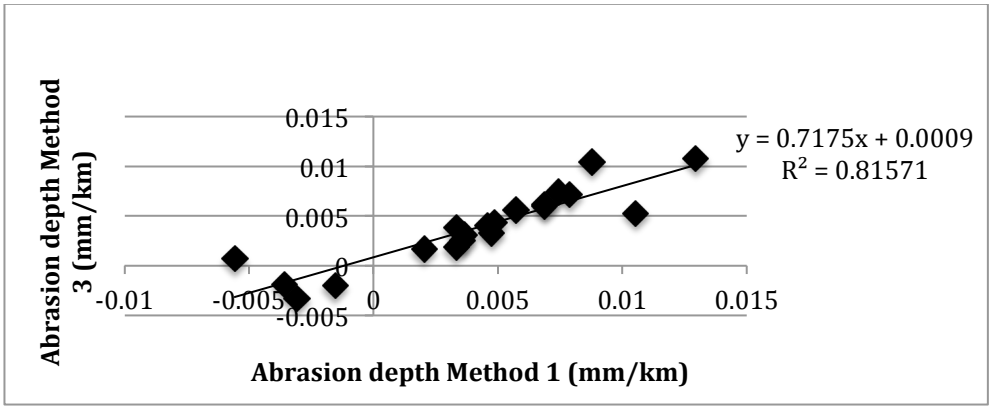

Figure 33 Correlation between calculation method 1 and 3

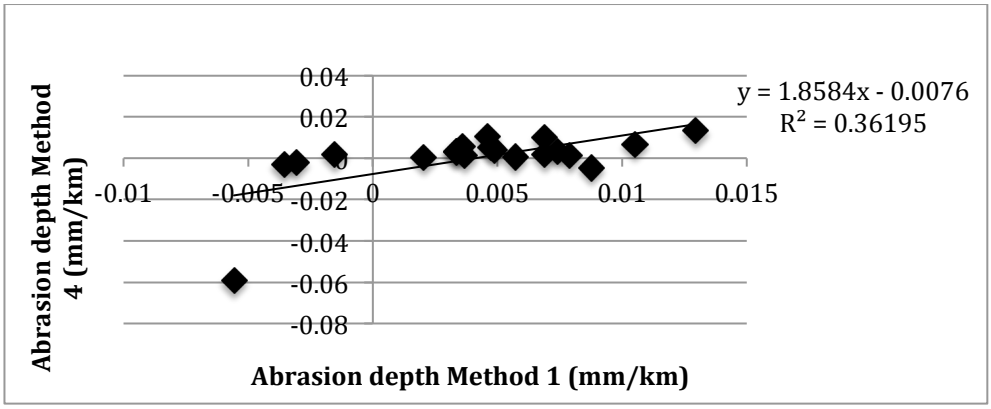

Figure 34 Correlation between calculation method 1 and 4

As mentioned earlier, the rest of the results presented in this chapter, except for the wear profiles in section 4.4.3, will be using an average of the abrasion rates calculated from methods 1 and 2, presented in Table 14. These are believed to give the most accurate abrasion results due to the systematic error in the measuring equipment mentioned in section 3.6.

Table 14 Abrasion rates calculated using the average of Method 1 and 2

Product type	Specimen number	Sliding velocity (cm/s)	Abrasion rate (mm/km) Average of Method 1 and 2	Overall Average for each Product Type (mm/km)*
B70 Reference	1.1*	16	-0.004	0.006
	1.2	16	0.005	
	2.1	25	0.011	
	2.2	25	0.002	
0.50% Steel	11.1*	16	0.001	0.003
	11.2	16	0.006	
	12.1	25	0.002	
	12.2	25	0.003	
1.50% Steel	21.1*	16	-0.002	0.007
	21.2	16	0.007	
	22.1	25	0.009	
	22.2	25	0.007	
1.50% Polypr.	31.1*	16	0.004	0.005
	31.2	16	0.006	
	32.1	25	0.007	
	32.2	25	0.004	
1.50% Basalt	41.1*	16	-0.002	0.001
	41.2	16	0.005	
	42.1	25	-0.006	
	42.2	25	0.003	

*Specimens measured using the old measuring method which are disregarded in the

One of the main purposes of this thesis is to study the effect of different fibers on the abrasion resistance of concrete. Therefore, the following figures are split up into product type groups using the following color-code:

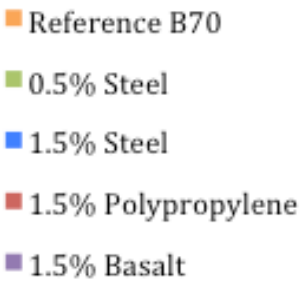

Figure 35 shows the average abrasion rate for each of the specimens in micrometers per kilometer. As seen in the figure, some of the specimens have a negative abrasion rate. Section 3.6 mentioned an old measuring method that was very inaccurate and used on

specimens 1.1, 11.1, 21.1, 31.1 and 41.1. Three of the four specimens showing this negative abrasion are ones that have used this old measuring method. This clearly indicates the inaccuracy of this method and the abrasion measurements done on the specimens using this old method may be misleading.

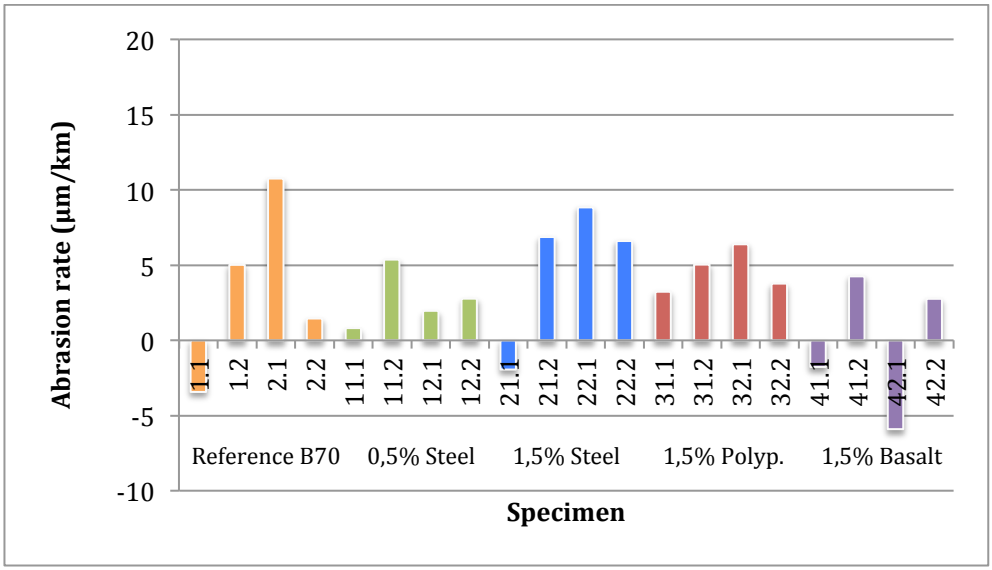

Figure 35 Total abrasion rate (µm/km) for each specimen

Figure 36 sums up the abrasion rate for the different test conditions and shows an average overall abrasion rate for the respective product types, disregarding the specimens that were measured using the old method. As an overall average, the specimens with 1.5% steel fiber addition seem to have the highest abrasion rate, while the specimens with 1.5% basalt fiber addition seem to have the lowest abrasion rate. Figure 37 shows the effect of sliding velocity on the abrasion rate, although no clear trends can be observed.

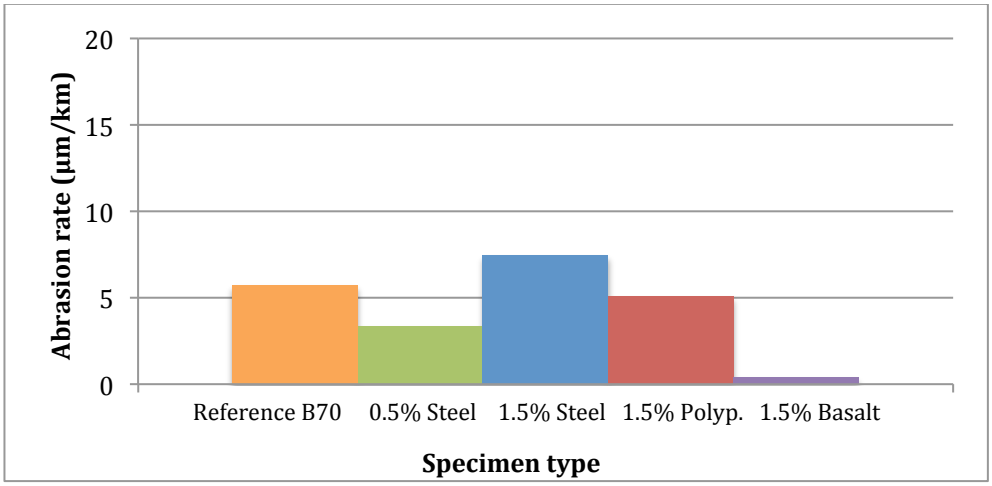

Figure 36 Average abrasion rates for the different product types, disregarding specimens 1.1, 11.1, 21.1, 31.1 and 41.1

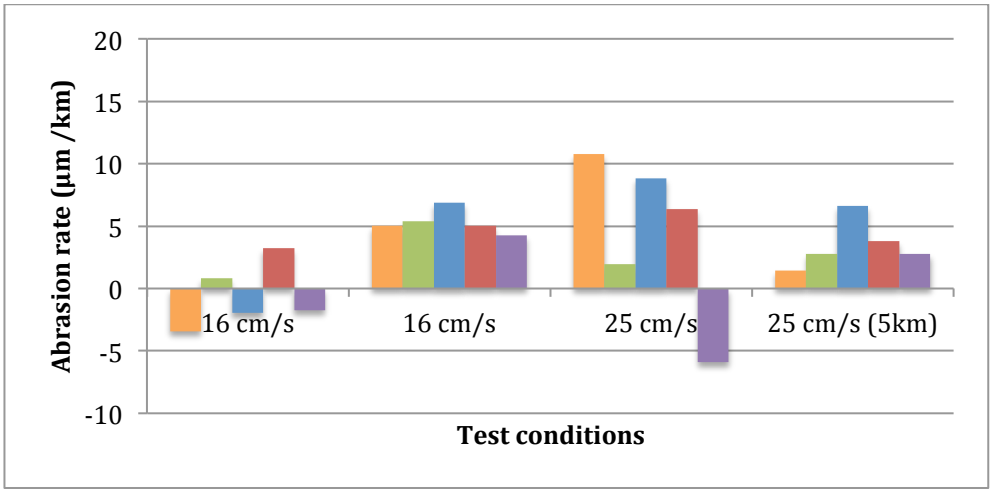

Figure 37 Abrasion rate for each specimen

Figures 38-40 split up the measurements according to effective abraded distance to see if there is any correlation in abrasion rates at different distances. Overall, the abrasion rate the first 1.25 km seems to be higher than for the rest of the abraded distance. The abrasion rate data used in these graphs can be found in Appendix H.

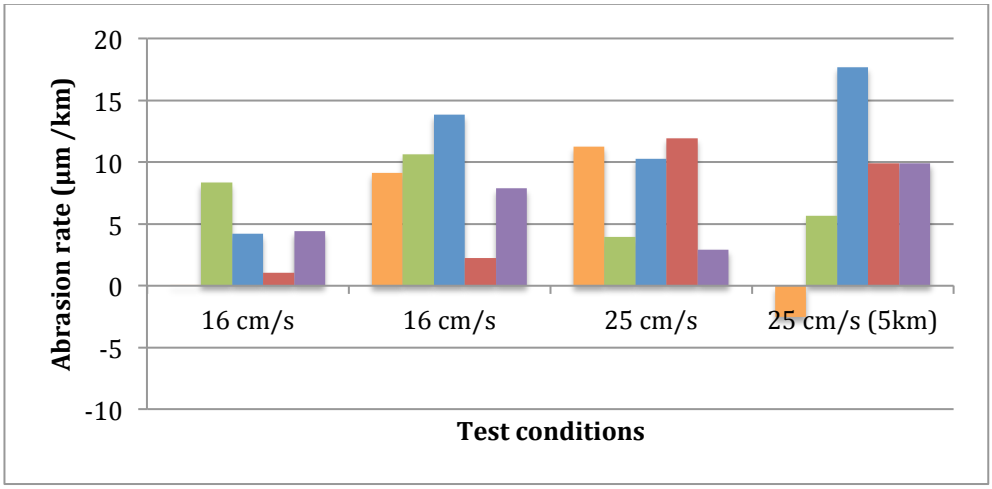

Figure 38 Abrasion rate between 0-1.25 km effective sliding distance

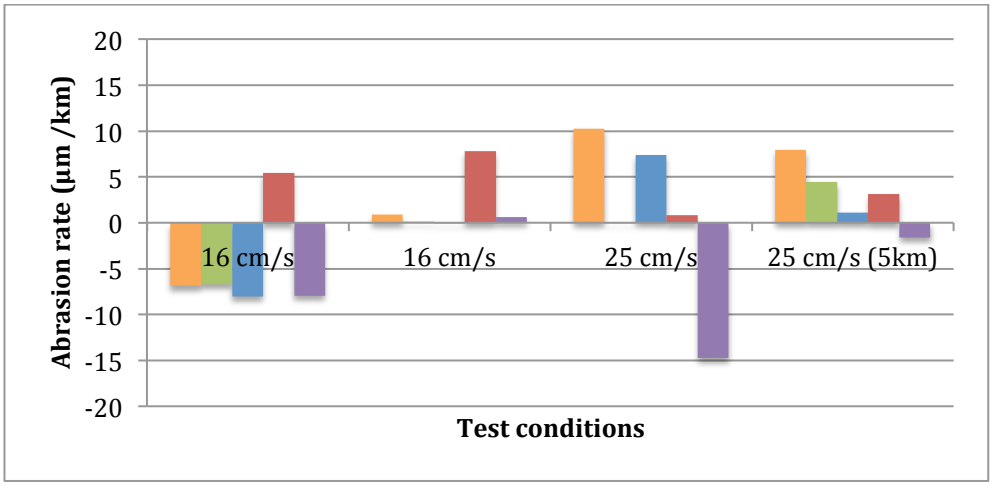

Figure 39 Abrasion rate between 1.25-2.5 km effective sliding distance

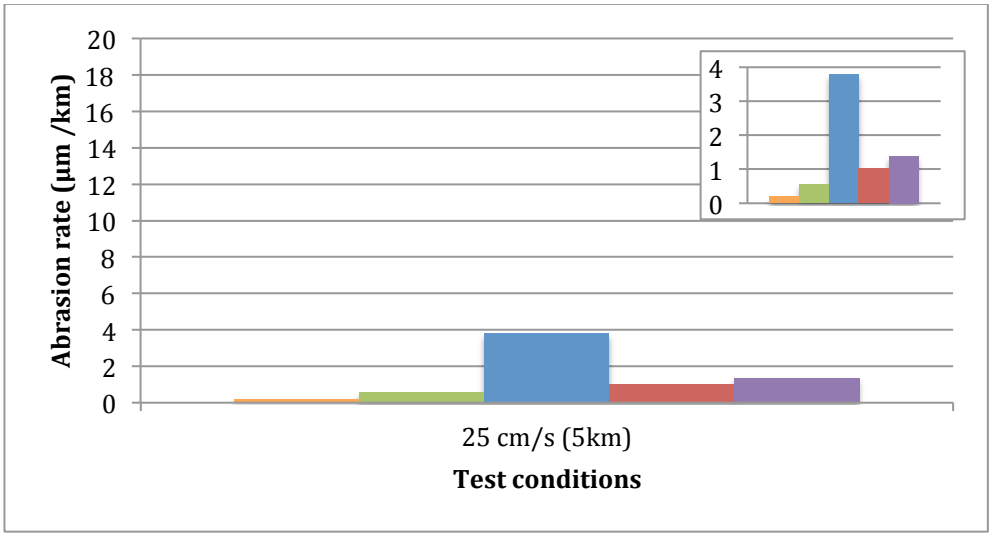

Figure 40 Abrasion rate between 2.5-5 km effective sliding distance

Figure 41 and Figure 42 show the abrasion rates at given abraded distances for specimens run at 16 cm/s and 25 cm/s, respectively. The abrasion rate data used in these graphs can be found in Appendix H.

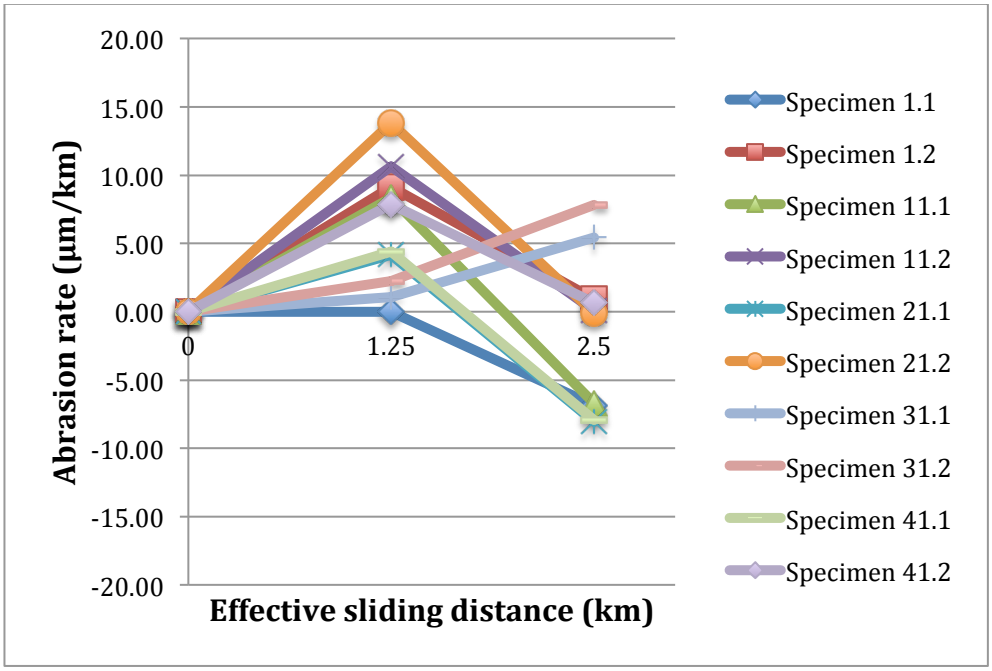

Figure 41 Abrasion rate for specimens run at 16 cm/s

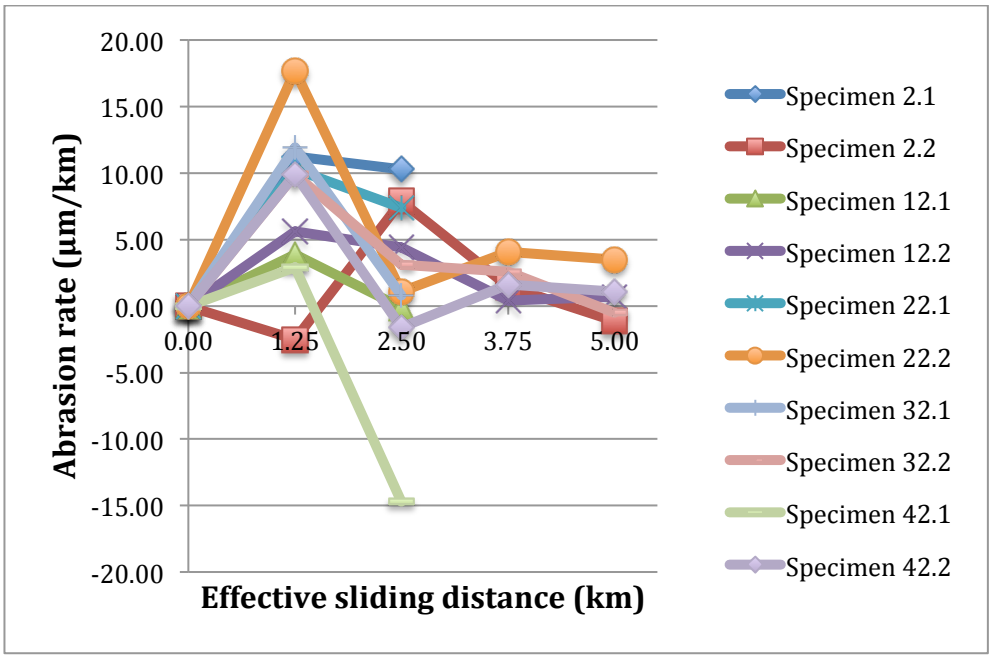

Figure 42 Abrasion rate for specimens run at 25 cm/s

In (Kirkhaug 2013), the abrasion of a similar B70 reference concrete as the one used in this thesis has been investigated. Figure 43 compares the results from these two abrasion studies. At an average, Kirkhaug´s results show an abrasion rate that is approximately eleven times the rate found in the abrasion experiments done for this thesis. The reasons for this is discussed in section 5.5.

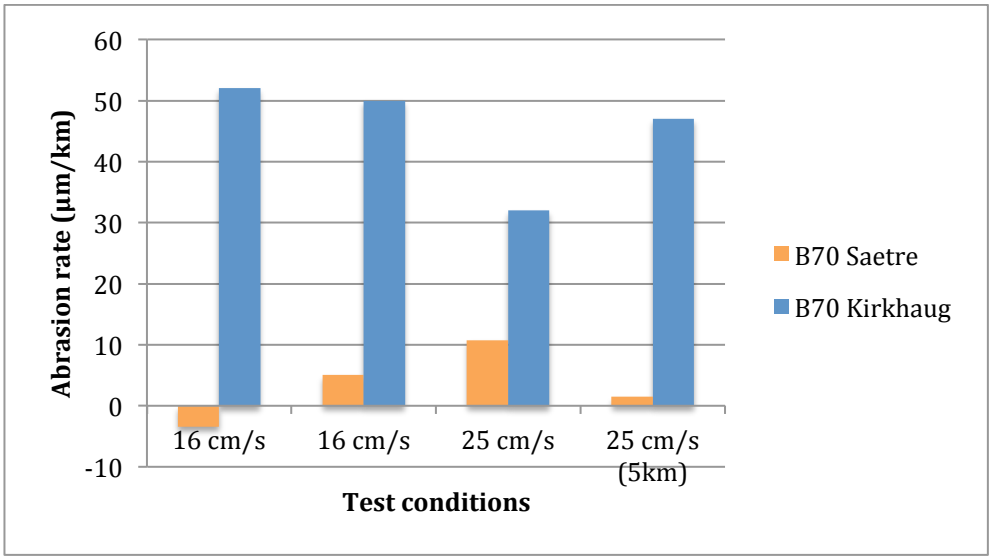

Figure 43 Comparison of abrasion rates with (Kirkhaug 2013) on B70 reference concrete

4.4.1 Test Conditions

Due to the large differences in abrasion results on the specimens in this thesis, a check of the general test conditions has been performed for two of the concrete specimens. The test conditions of specimen 12.1 and specimen 22.1, with, respectively, low and high abrasion rates relative to each other, have been studied in order to check if any differences in the test conditions can be the cause of the abrasion differences.

Figures 44-46 show the average vertical load throughout the entire sliding distance for specimen 12.1, 22.1 and 31.1, respectively. This data is logged by Labview and is found in Column I under the name Vert Load Sum Cycle when opening the log files in Microsoft Excel.

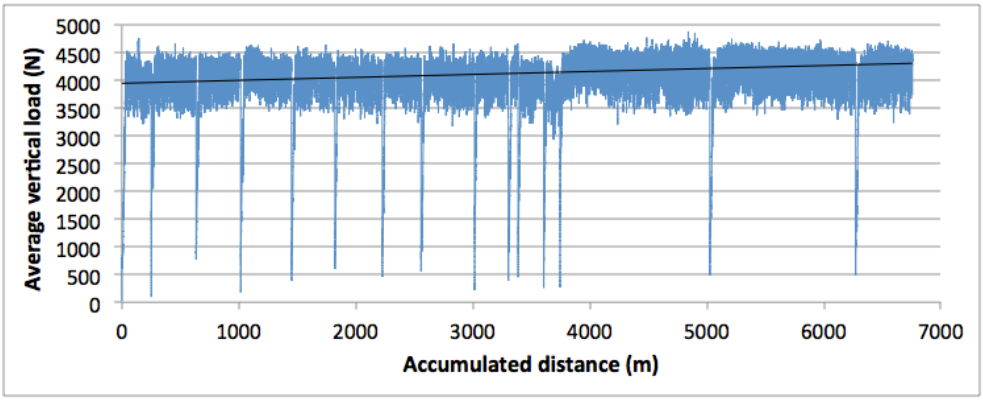

Figure 44 Average vertical load vs sliding distance for specimen 12.1

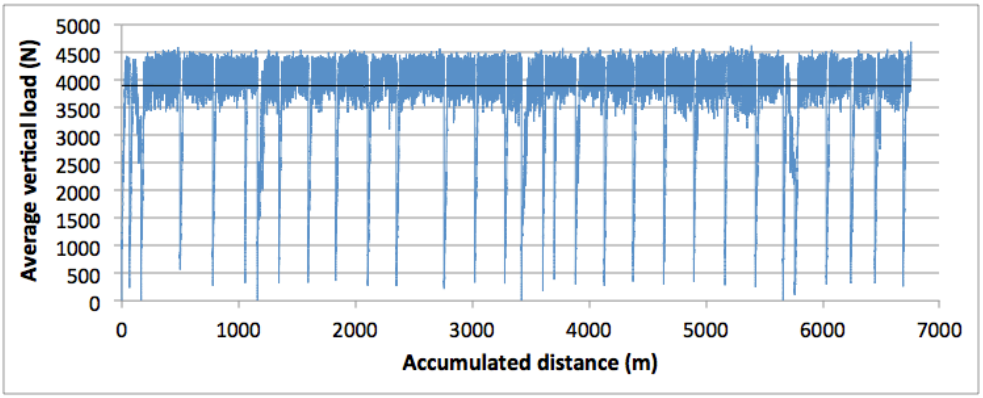

Figure 45 Average vertical load vs sliding distance for specimen 22.1

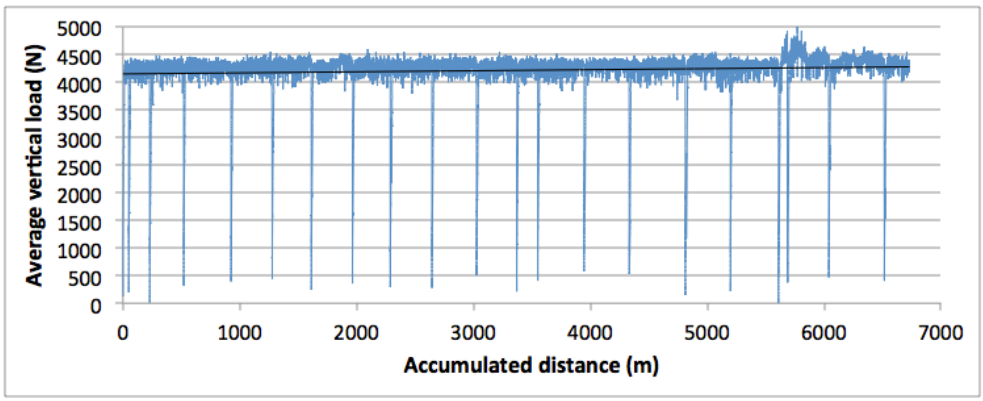

Figure 46 Average vertical load vs sliding distance for specimen 31.1

Figures 47 and 48 show the average recorded sliding velocity for specimens 12.1 and 31.1, respectively. This data is logged by Labview and is found in Column Q under the name Mean Hor. Velocity Cycle when opening the log files in Microsoft Excel.

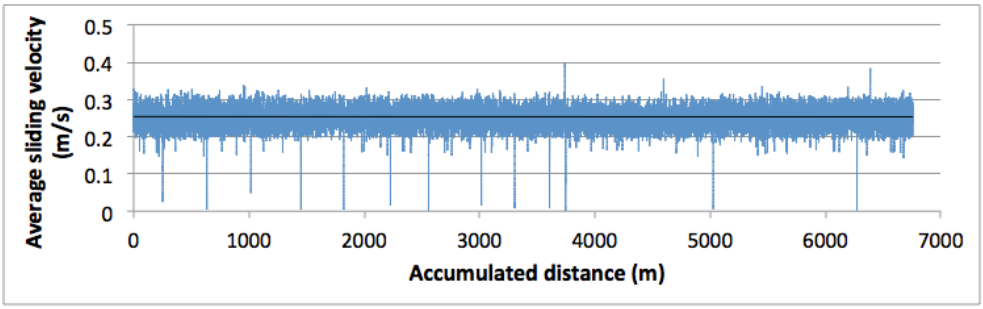

Figure 47 Average sliding velocity vs sliding distance for specimen 12.1

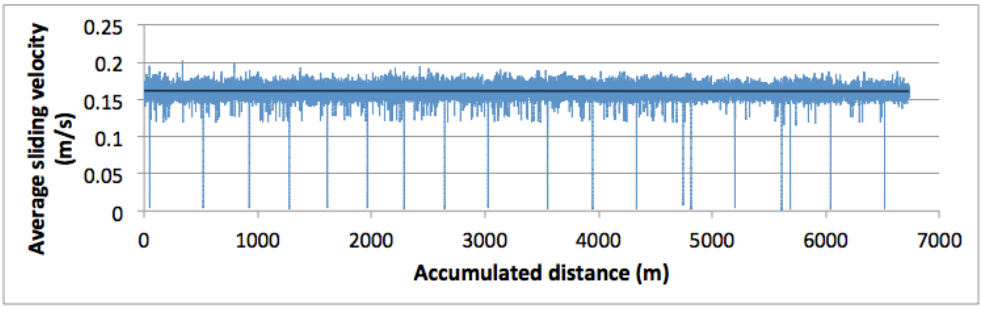

Figure 48 Average sliding velocity vs sliding distance for specimen 31.1

Figure 49 and Figure 50 show the air temperature in the test room during testing for specimens 12.1 and 22.1. Figure 51 shows the air temperature in the test room during testing on a B70 concrete specimen in (Kirkhaug 2013). This data is logged by Labview and is found in Column Y under the name Reserve Temp Wago 22 when opening the log files in Microsoft Excel.

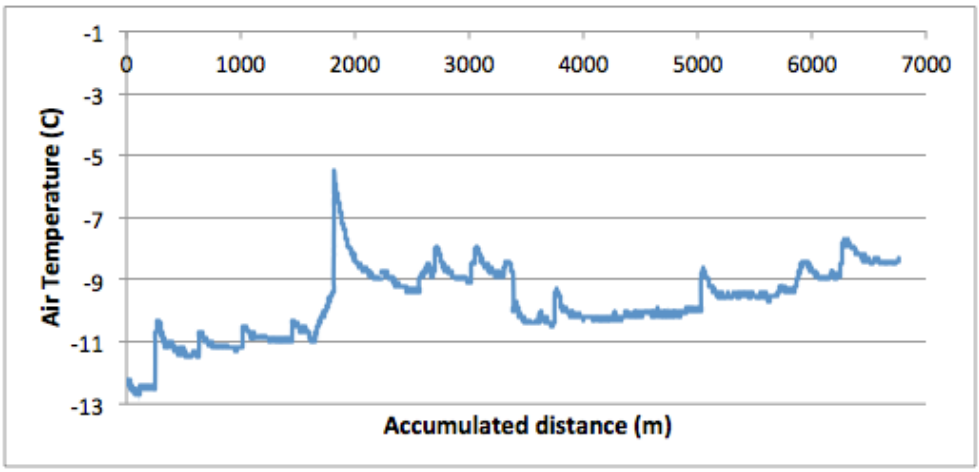

Figure 49 Air temperature in ice abrasion rig room vs accumulated sliding distance for specimen 12.1

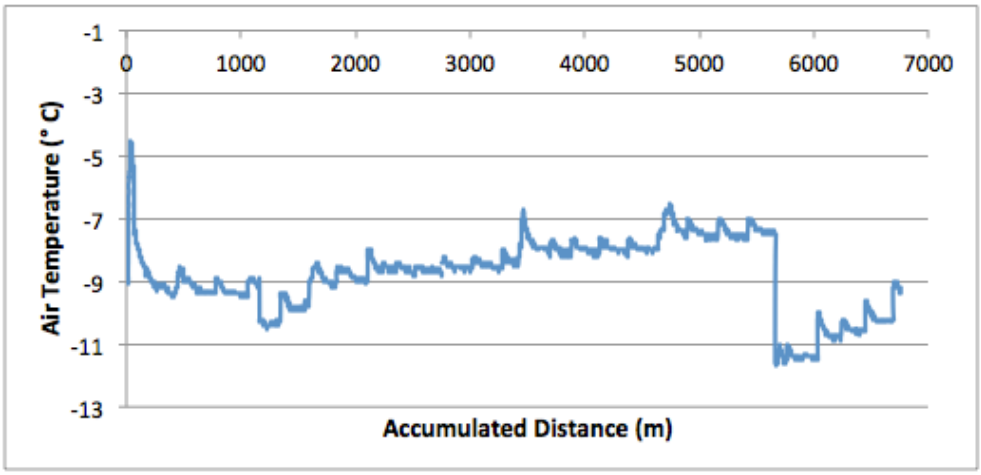

Figure 50 Air temperature in ice abrasion rig room vs accumulated sliding distance for specimen 22.1

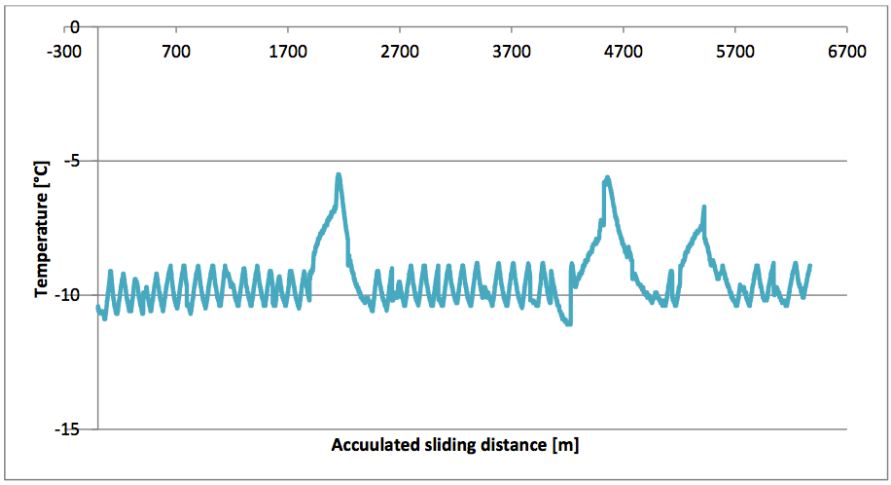

Figure 51 Air temperature in ice abrasion rig room vs accumulated sliding distance for a B70 specimen tested in (Kirkhaug 2013)

Figure 52 and Figure 53 show the temperature variations of the ice specimen cylinder for specimens 12.1 and 22.1. This data is logged by Labview and is found in Column U under the name Air Temp (C) Wago 21 when opening the log files in Microsoft Excel. It is important to notice that even though the column is named Air Temp, it is actually the ice cylinder temperature.

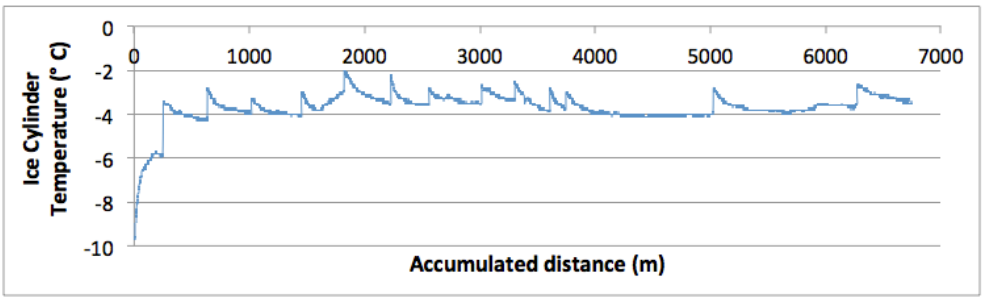

Figure 52 Ice cylinder temperature vs accumulated sliding distance for specimen 12.1

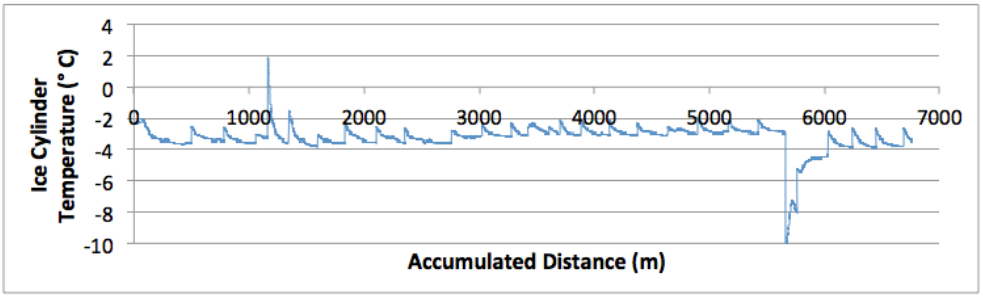

Figure 53 Ice cylinder temperature vs accumulated sliding distance for specimen 22.1

The final general test condition that is thought to possibly have affected the abrasion results, is the temperature in the concrete specimen during testing. The filling of epoxy in the copper plate under the concrete specimen has altered the temperature variation in the concrete specimen during testing. Figure 54 shows the temperature variation in the concrete specimen before the addition of epoxy, measured by (Kirkhaug 2013). Figure 55 shows the temperature variation measured after the addition of epoxy filling. This data is logged by Labview and is found in Column V, X and AB when opening the log files in Microsoft Excel.

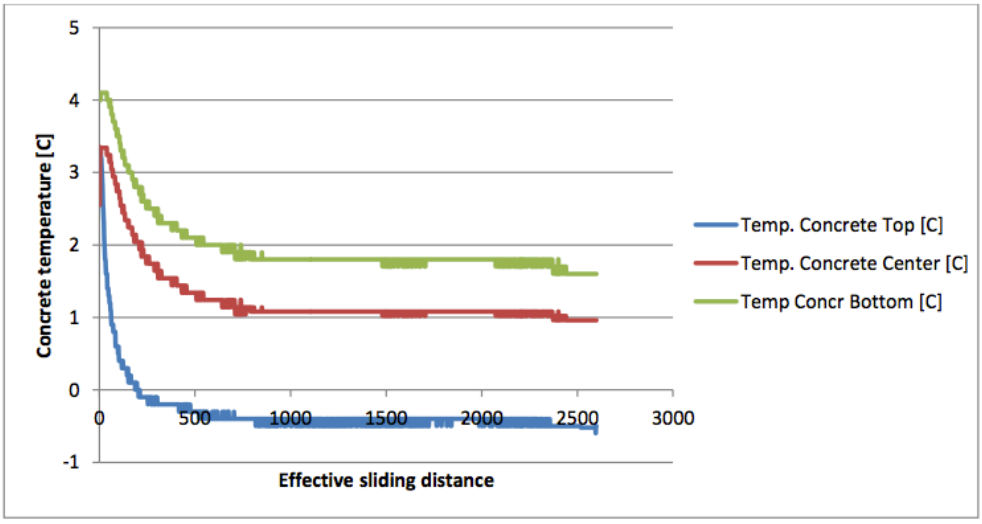

Figure 54 Temperature in concrete specimen during testing from (Kirkhaug 2013)

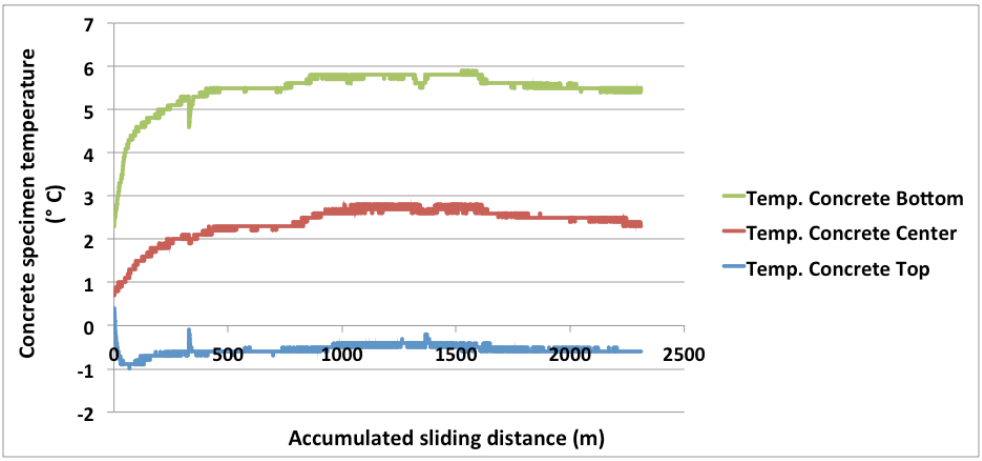

Figure 55 Temperature in concrete specimen during testing after filling of epoxy

4.4.2 Roughness

Based on the discussion in section 2.6.2, where it was concluded that it is more appropriate to use surface roughness parameters compared to profile roughness parameters for evaluating the surface of concrete, Table 15 presents the surface roughness values for all of the specimens, before and after 2.5 km effective sliding distance.

Table 15 Surface Roughness Parameters

Specimen	Surface Roughness Parameters							
	Before abrasion (mm)				After 2.5 km abrasion (mm)			
	S_a	S_q	S_{sk}	S_{ku}	S_a	S_q	S_{sk}	S_{ku}
Specimen 1.1	0.233	0.270	-0.340	2.035	0.262	0.319	-0.424	2.355
Specimen 1.2	0.125	0.143	0.601	2.260	0.108	0.127	0.746	2.493
Specimen 2.1	0.076	0.096	0.875	3.039	0.069	0.091	1.049	3.596
Specimen 2.2	0.115	0.139	0.761	2.601	0.114	0.139	0.832	2.699
Specimen 11.1	0.112	0.146	0.904	3.716	0.110	0.140	0.982	3.370
Specimen 11.2	0.074	0.093	0.933	3.114	0.076	0.096	1.139	3.446
Specimen 12.1	0.061	0.080	0.907	3.508	0.059	0.078	0.855	3.410
Specimen 12.2	0.081	0.209	-6.320	49.352	0.082	0.209	-6.222	48.471
Specimen 21.1	0.165	0.206	1.052	3.183	0.107	0.135	0.926	3.400
Specimen 21.2	0.099	0.118	0.641	2.529	0.087	0.105	0.857	2.767
Specimen 22.1	0.054	0.076	0.108	4.651	0.052	0.069	0.856	3.530
Specimen 22.2	0.086	0.103	-0.465	2.556	0.080	0.096	-0.649	2.758
Specimen 31.1	0.100	0.121	-0.001	2.459	0.069	0.085	-0.511	3.015
Specimen 31.2	0.085	0.105	0.967	3.033	0.077	0.097	1.051	3.282
Specimen 32.1	0.070	0.090	1.119	3.573	0.074	0.097	0.568	3.239
Specimen 32.2	0.069	0.087	-0.501	3.366	0.064	0.084	-0.192	3.124
Specimen 41.1	0.076	0.103	-0.203	4.605	0.084	0.112	-0.262	4.498
Specimen 41.2	0.050	0.066	0.823	3.505	0.047	0.063	0.818	3.553
Specimen 42.1	0.076	0.096	1.097	3.475	0.072	0.089	-0.831	3.315
Specimen 42.2	0.062	0.083	1.127	3.775	0.056	0.076	1.073	3.930

S_a=Surface Average Roughness; S_q= Surface Root Mean Square Height; S_{sk}=Surface Skewness;S_{ku}=Surface Kurtosis

Figure 56 and Figure 57 show the correlation between the different surface roughness parameters and the abrasion rate.

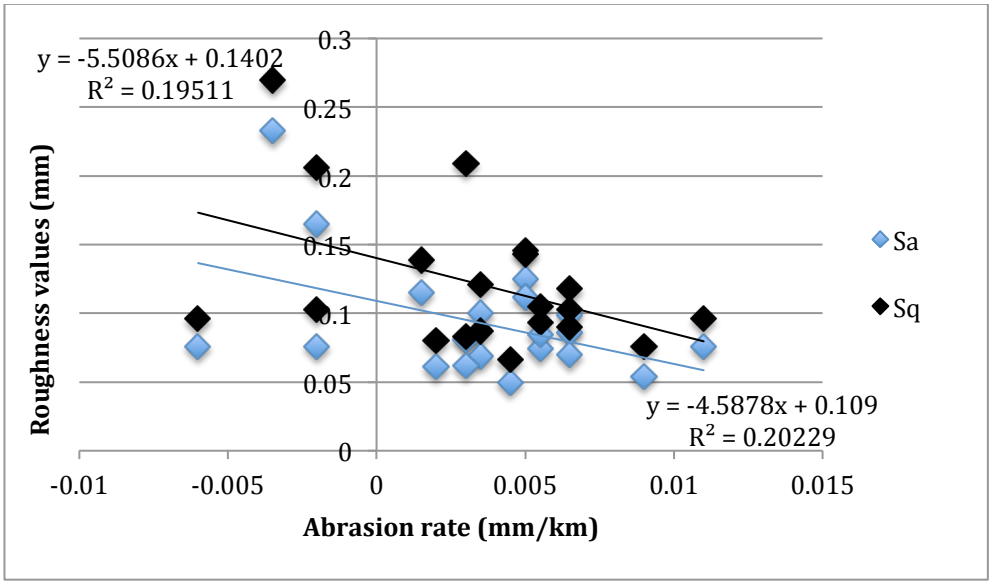

Figure 56 Correlation between average surface roughness, root mean square roughness and abrasion rate

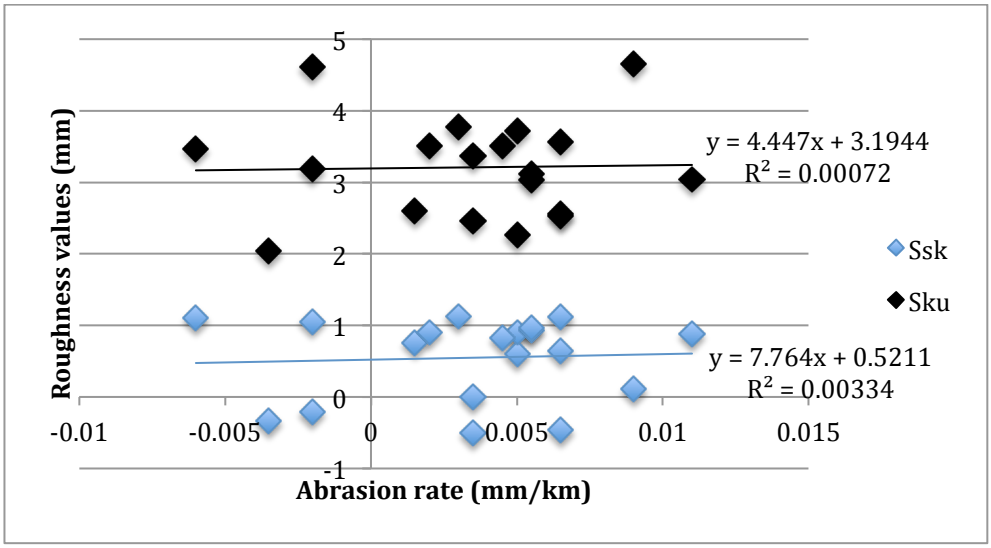

Figure 57 Correlation between surface skewness, surface kurtosis and abrasion rate

Irregularities in the concrete surfaces are thought to have affected the surface roughness values. Figure 58 and Figure 59 show 3D plots of the concrete specimen surfaces before abrasion for specimens 21.1 and 22.1. Figure 60 and Figure 61 show 3D plots of the same concrete

specimens after 2.5 km effective abrasion. These plots have been made using Microsoft Excel with the data from the measurements using the Mitutoyo digital indicator. To see the similarities in the surface irregularities for the different specimens, refer to Appendix I, where the 3D plots before abrasion for the rest of the specimens have been plotted. A large drop can be seen to the left in Figure 58, as well as in a couple of the other 3D plots in Appendix I. This is due to the measuring point at this spot hitting a cavity, similar to the one shown in Figure 68.

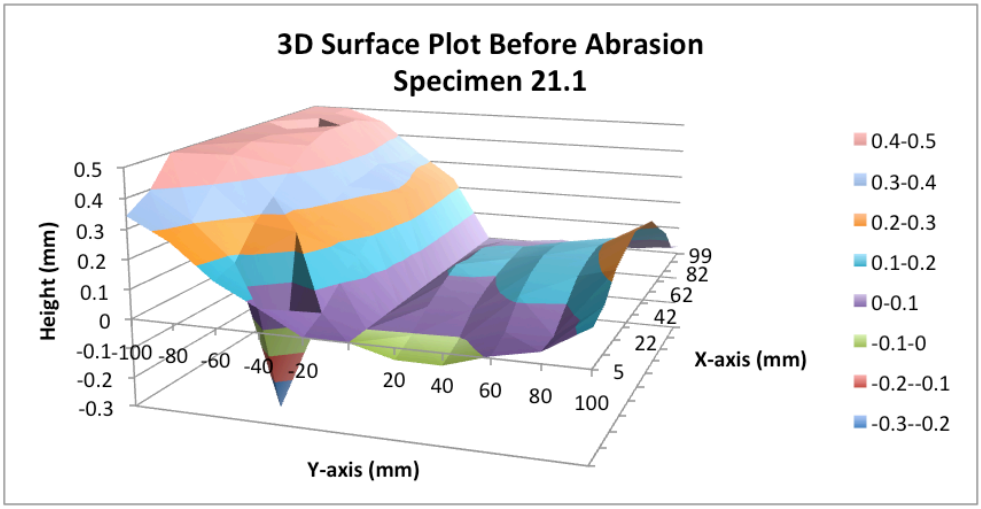

Figure 58 3D surface plot of specimen 21.1 before abrasion

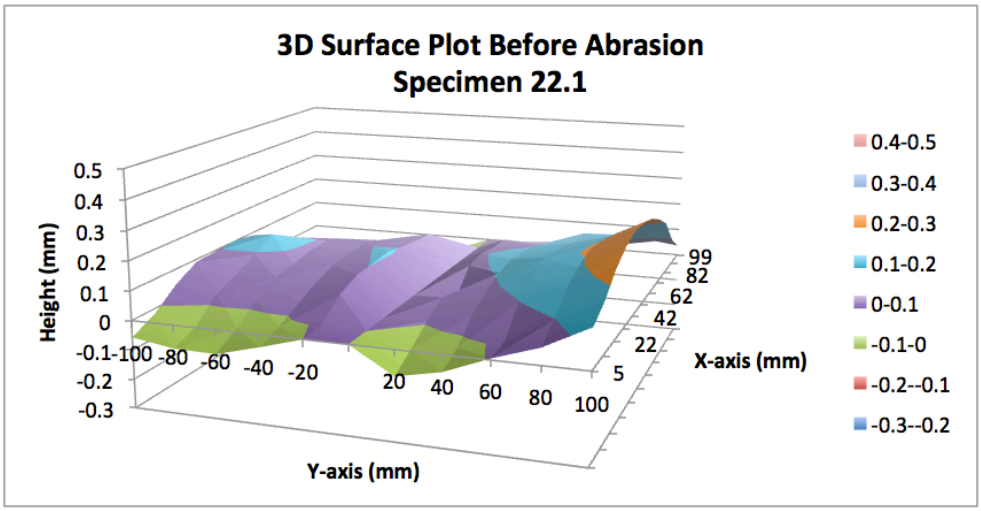

Figure 59 3D surface plot of specimen 22.1 before abrasion

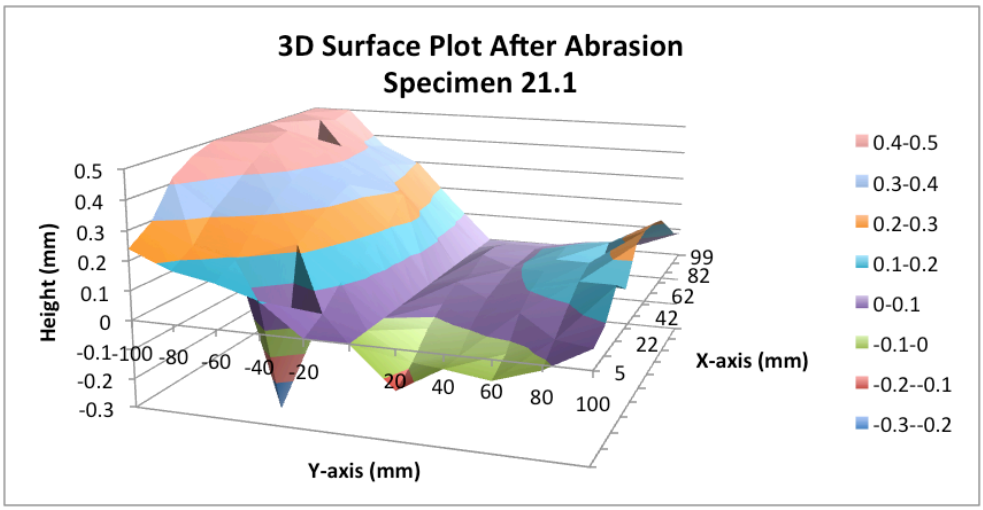

Figure 60 3D surface plot of specimen 21.1 after 2.5 km effective abrasion

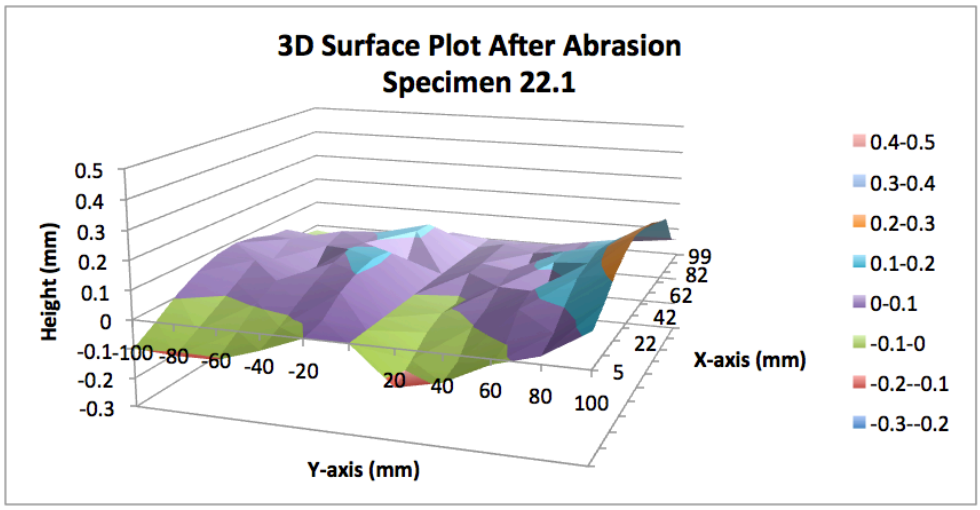

Figure 61 3D surface plot of specimen 22.1 after 2.5 km effective abrasion

4.4.3 Wear Profile

Based on the studies done by (Itoh, Yoshida et al. 1988) it is interesting to see if the concrete ice abrasion experiments at the

NTNU laboratory show the same effect of a larger wear depth at the center than at either side along the x-axis (Figure 28). The wear profile along the x-axis, using abrasion calculation methods 1 and 2, has been plotted for all of the specimens in order to see if there is any trend. No consistent trend has been found, neither supporting Itoh´s studies nor the idea by (Jacobsen, Sætre et al. 2013) of a more homogeneous wear profile due to the ice being confined within a steel cylinder. Figures 62-64 show the wear profiles along the x-axis of three randomly chosen specimens. The wear profiles for the rest of the specimens are presented in Appendix J, and the data for these wear profiles is found in Appendix K. It is important to notice that these graphs are inversed compared to Itoh´s wear profiles in Figure 12. Whereas Itoh´s figure shows the profile height along the y-axis, these graphs show the abrasion depth along the y-axis.

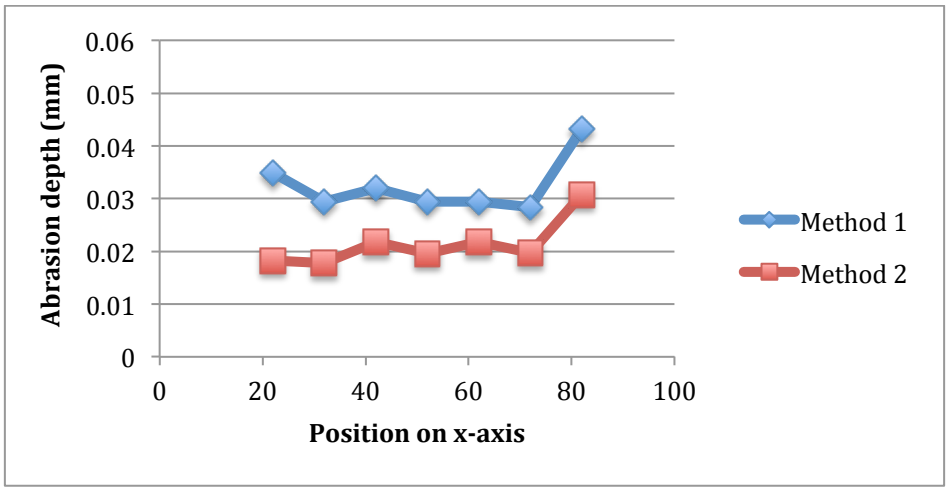

Figure 62 Wear profile along x-axis for specimen 2.1

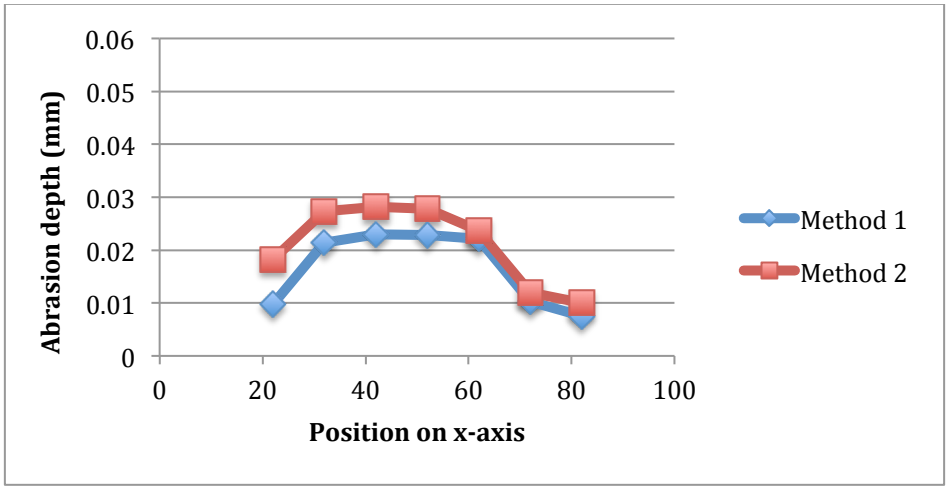

Figure 63 Wear profile along x-axis for specimen 32.2

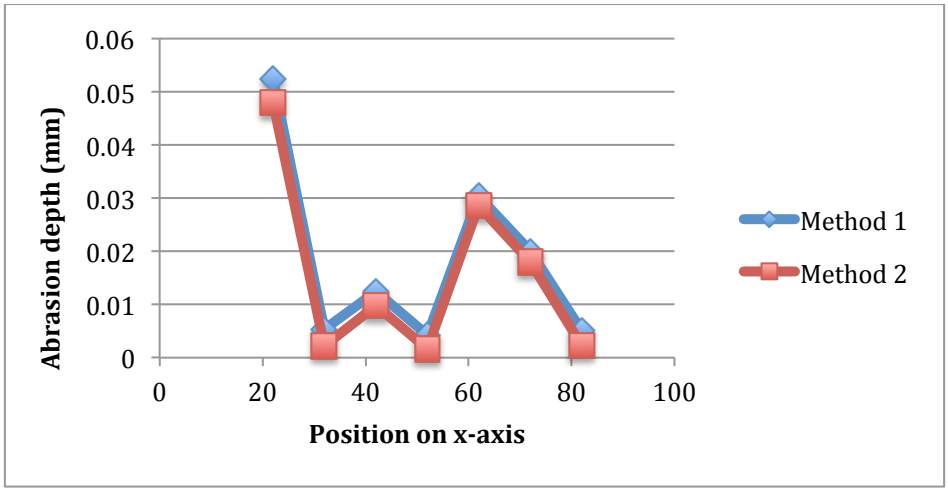

Figure 64 Wear profile along x-axis for specimen 21.2

It was also of interest to investigate the wear profile along the y-axis of the concrete specimens. (Kirkhaug 2013) found a tendency of increased abrasion on the edges of the specimens where the ice specimen turns. The wear profile along the y-axis, using abrasion calculation methods 1 and 2, of three randomly chosen specimens can be seen in Figures 65-67. The wear profiles along the y-axis for the rest of the specimens are presented in Appendix L, and the data for these wear profiles is found in Appendix M.

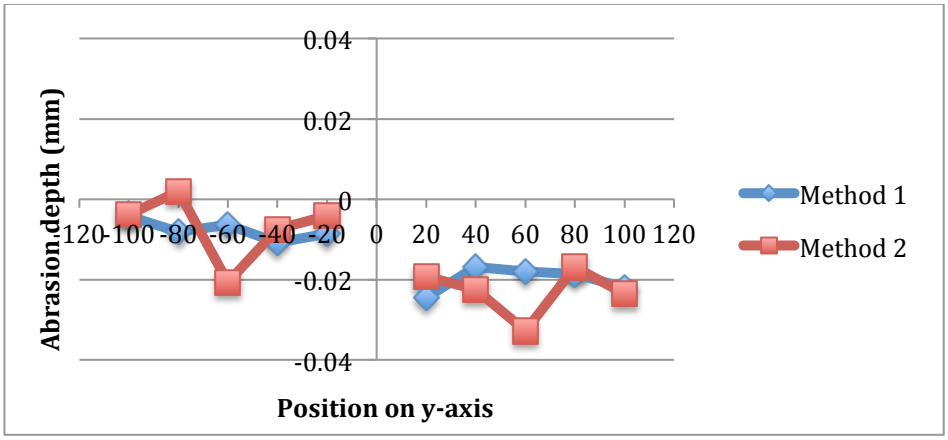

Figure 65 Wear profile along y-axis for specimen 42.1

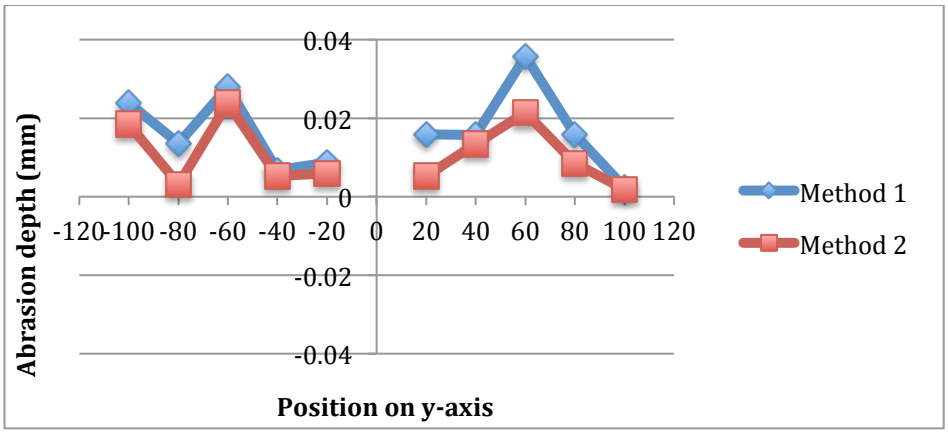

Figure 66 Wear profile along y-axis for specimen 32.1

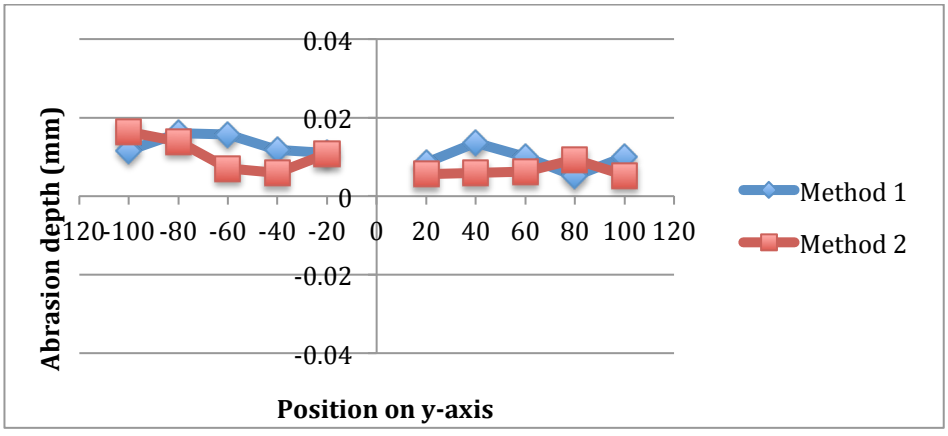

Figure 67 Wear profile along y-axis for specimen 1.2

5 Discussion

In parts of the following discussion related to the effect of various parameters on the abrasion rate of the different concrete specimens, it is chosen to disregard the specimens that were measured using the old measuring method, as referred to in section 3.6. This means that specimens 1.1, 11.1, 21.1, 31.1 and 41.1 are disregarded. Due to lack of time, the friction data from the experiments in this thesis has not been analyzed. It is referred to (Kirkhaug 2013) and (Greaker 2014) for a discussion on the effects of friction coefficients on the abrasion rate using the NTNU ice abrasion rig.

5.1 Effect of Different Fiber Types on Abrasion Resistance

Figure 36 shows the overall average of the abrasion rate for the different product types, disregarding the specimens that were measured using the old method, and independent of the test conditions. From this figure we can rank the different product types from highest abrasion rate to lowest abrasion rate: 1.5% steel fiber (7.4 μm/km), B70 reference (5.7 μm/km), 1.5% polypropylene (5.1 μm/km), 0.5% steel (3.4 μm/km) and 1.5% basalt (0.4 μm/km). The very low average abrasion rate on the concrete specimens with basalt fiber is mainly due to the abrasion rate measured on specimen 42.1 (-5.9 μm/km). Obviously, this negative abrasion rate must be due to some measuring inaccuracy. The swelling of concrete can be another explanation for this volume increase, but is deemed unlikely due to the relatively short period of times between measurements. Disregarding this one measurement, the average abrasion rate for the concrete specimens with 1.5% basalt fiber addition is 3.5 μm/km, which places it just above the abrasion rate of the specimens with 0.5% steel fiber additions.

From these results, it can be concluded that all of the fiber additions, except for the 1.5% steel fiber addition, have improved the ice abrasion resistance of the concrete. This supports the studies done by, among others (Kabay 2014), (Sun and Xu 2009) and (Grdic, Curcic et al. 2012), which have shown that the abrasion resistance of concrete, although not by ice, is improved with the use of basalt and polypropylene fibers. The results in Figure 36 also show a decreased

abrasion resistance with increased amounts of steel fiber, contradicting the findings in (Maage 1977) and (Horszczaruk 2009), where it was found that increasing amounts of steel fiber gives an increased abrasion resistance.

The negative effect on abrasion resistance observed here for a 1.5% steel fiber addition has not been found in earlier studies as far as the author of this thesis is aware of, but similar results showing that the addition of steel and polypropylene fibers have no effect on the abrasion resistance have been found in (Nanni 1989) and (Atis, Karahan et al. 2009).

5.2 Effect of Sliding Velocity and Sliding Distance on Abrasion Resistance

Figure 37 shows the abrasion rate for the different specimens at the two sliding velocities, 16 cm/s and 25 cm/s. No clear trend can be observed from these results. When comparing the reference concrete specimens, the abrasion rate for one of the specimens run at 25 cm/s more than doubles compared to the specimen run at 16 cm/s, while for the other reference specimen run at 25 cm/s the abrasion rate is reduced to about one third compared to the one run at 16 cm/s.

The same contradicting results are seen in the specimens with 1.5% polypropylene and 1.5% steel fiber additions. For both of these product types, the abrasion rates for the specimens run at 25 cm/s both increases and decreases compared to the specimen run at 16 cm/s. On the other hand, both the specimens with 0.5% steel and 1.5% basalt additions show a decrease in abrasion rates at an increased sliding velocity.

The effect of sliding velocity ranges from 70% decreases to 120% increases between sliding velocities 16 cm/s and 25 cm/s. These contradicting results lead to a conclusion that sliding velocity between ice and fiber reinforced concrete has little effect on the abrasion rate, supporting the findings in (Itoh, Tanak et al. 1994).

The results presented in Figure 41 and Figure 42 show a tendency of the abrasion rates decreasing between effective sliding distance 1.25-2.5 km compared to between 0-1.25 km. The reason for this is unknown, especially since the general test conditions are shown to be

close to constant throughout the abrasion tests, as discussed in section 5.5. At extended sliding distances the abrasion rates seem to level out and approach zero, as seen in Figure 42.

5.3 Effect of Roughness Parameters on Abrasion Resistance

The effect of the *Surface Roughness Parameters* on the abrasion resistance of concrete has been studied. Table 15 presents the *Surface Average Roughness*, *Root Mean Square Roughness*, *Skewness* and *Kurtosis* for all of the specimens, before and after 2.5 km abrasion. They are in the range 0.047-0.262 mm, 0.063-0.319 mm, -0.831-1.139 mm and 2.035-4.651 mm, respectively. This is disregarding the extreme values for *Skewness* and *Kurtosis* shown for specimen 12.2, which are discussed in section 5.4.1. The *Average Roughness* values are all much larger than the abrasion rates. This can result in an inaccuracy in the abrasion measurements and is discussed in section 5.8.

The correlation between these different roughness parameters and the abrasion rate is shown in Figure 56 and Figure 57. A trend can be seen in Figure 56 that a decreasing *Surface Average Roughness* (S_a) and *Root Mean Square Roughness* (S_q) result in an increased abrasion rate. This is expected because a decrease in these roughness values means a flatter surface, which in turn means a larger contact area between the concrete and the ice.

As seen in Figure 57, most of the *Skewness* (S_{sk}) values are positive and around 1 mm. This makes it difficult to see any trend on the effect of *Skewness* on abrasion rates. The same goes for the *Kurtosis* (S_{ku}) values, which are mostly in the area 2.5-4 mm and do not show any trend on it´s effect on abrasion rates. Neither the positive effect on abrasion rate of a positive skewness, nor a kurtosis value larger than three, as predicted in section 2.6.3, have been confirmed from these experiments. The effect of *Surface Skewness* and *Kurtosis* on abrasion rate is an area that should be studied further.

The effect of abrasion on the *Surface Roughness Parameters* has also been looked into. In general, the values after 2.5 km abrasion are similar to the values before abrasion. The *Average Roughness* decreases with an average of 6%, the *Root Mean Square Roughness*

decreases with an average of 5% and the *Surface Kurtosis* increases with an average of 3%. The only parameter that shows a significant difference after abrasion is the *Surface Skewness*, which has an average increase of 34%. The reliability of these roughness calculations is questionable, though, as discussed in the following chapter.

5.4 Reliability of Roughness Calculations

5.4.1 Effect of Varying Distances Between Measuring Points on Roughness Calculations

The above discussion on roughness is based on a very coarse grid with only 110 measuring points on the entire surface. Using an ATOS 3D Optical Scanner, (Sætre 2013) studied the effect of varying distances between measuring points when calculating the profile roughness of one of the concrete specimens used in (Kirkhaug 2013). Here, up to 200000 points have been measured along one profile of the surface. Table 16 presents the results.

Table 16 Average roughness with varying distances between measuring points on one of Kirkhaug´s samples (Sætre 2013)

Distance between measuring points	Average profile (length=90mm) roughness, Ra (x-axis)	Average profile (length=200mm) roughness, Ra (y-axis)
10 mm	0.1091	0.0771
5 mm	0.1928	0.0684
1 mm	0.2021	0.0690
0.1 mm	0.2055	0.0694
0.01 mm	0.2058	0.0695
0.001 mm	0.2058	0.0695

It can be seen that the average roughness parameter converges toward a value of 0.2058 and 0.0695 in the x and y-axis, respectively, when decreasing the distance between measuring points. A distance of 5 mm between the measurement points will give a roughness value with an accuracy of 0.013 mm along the x-axis, and an accuracy of 0.001 along the y-axis. The differences in these accuracies are due to

the fact that these measurements are just of a single profile along the axes, and do not represent the entire surface. However, these results imply that a maximum distance of 5 mm between measuring points is needed to get an accurate roughness value. An example of this can be seen in Figure 16. A large difference between each measurement point can result in all of the measuring points being on the top of the peaks or all of them in the bottom of the valleys. This would result in the roughness values representing a flat surface, when in reality the surface is not flat at all. By decreasing the distance between each measuring point, the chances are that the measuring points will both hit on the peaks and in the valleys, giving a better representation of the surface.

In this thesis, surface roughness parameters have been calculated instead of profile roughness parameters. The distances between measuring points have been 10 mm along the x-axis and 20 mm along the y-axis. The use of surface instead of profile parameters may provide a better picture of the surface topography, but the distances between each measurement should still be cut down to a maximum of 5 mm along both axes in order to calculate accurate roughness parameters. This implies that the roughness values calculated in Table 15 may be inaccurate and misleading.

Measuring points with distances of 5 mm or less between each point will be very time consuming if done with the Mitutoyo Digital Indicator. Therefore it is recommended to use the ATOS 3D Optical Scanner to scan the surfaces and then use the program GOM Inspect to extract data from the scans. An explanation and user manual for this program is given in (Sætre 2013). Lack of time is the reason why roughness inspections of the concrete surfaces have not been done using the ATOS 3D Optical Scanner for this thesis.

As seen in Table 15, Specimen 12.2 has very large *Surface Skewness* and *Surface Kurtosis* values. This was investigated a bit closer, and it was found that this was due to one of the measuring points having been in a large cavity on the concrete surface, which resulted in this one point having a large deviation from the mean plane. An illustration of this can be seen on the 3D plot of Specimen 12.2 in Appendix I. When using such a small amount of measuring points to calculate the surface roughness as is done here, these extreme values will affect the roughness parameters drastically. Just by changing this one extreme value to a value close to the mean plane, the skewness increased from -6.3 to 0.9 and the kurtosis fell from 49.3 to 3.5,

similar to the other surfaces. These drastic changes in roughness values because of only one of the measuring points also indicates the need of measuring as many points on the surface as possible in order to get accurate roughness values.

5.4.2 Effect of Systematical Irregularities on Concrete Surfaces on Roughness Calculations

On the 3D plots in Figures 58-61, systematical irregularities can be seen on the concrete surfaces in both the x-axis and y-axis; a curvature along the x-axis and height differences of up to 0.7 mm along the y-axis. By systematical, it is meant that these irregularities are not due to the roughness of the concrete surface, but to the fact that the surface is not flat. A reason for this may be that the plane cutting equipment at NTNU, pictured in Figure 20, is not accurate enough. Similar systematical irregularities are seen in all of the concrete surfaces (Appendix I), meaning that none of these surfaces are perfectly flat. The same systematical irregularities are also seen in the 3D plots after abrasion, in Figure 60 and Figure 61.

These irregularities are suspected to influence the roughness parameter measurements and may cause misleading roughness parameter values. This is because the formulas for the different roughness parameters assume a flat surface. This suspicion is investigated by comparing two specimens of the same product type; one that shows large systematical irregularities on the surface (Specimen 21.1 in Figure 58) and one that shows a relatively smaller amount of systematical irregularities on the surface (Specimen 22.1 in Figure 59). These, being two specimens of the same concrete mix, are expected to have similar roughness parameter values, but due to the larger amount of systematical irregularities on Specimen 21.1, the assumption is that this specimen will show significantly higher roughness values.

Table 15 presents the roughness data for these specimens before abrasion. Specimen 21.1 is found to have a *Surface Average Roughness (S_a)* of 0.165 mm and a *Surface Root Mean Square Roughness (S_q)* of 0.206 mm. Specimen 22.1 is found to have an S_a of 0.054 mm and an S_q of 0.076 mm. This is an increase of 206% and 171% on the S_a and S_q, respectively. This result supports the assumption of these systematical irregularities on the concrete surface having an effect on the roughness parameters. This same trend of

these systematical irregularities increasing the roughness values is seen in all of the different concrete mixes.

5.5 Effect of Test Conditions on Abrasion Resistance

A comparison has been done between two of the concrete specimens; specimen 12.1, which had a low abrasion rate, and specimen 22.1, which had a high abrasion rate. This is done to investigate if any of the test conditions can be the cause of the large differences in abrasion rates. The test conditions are also compared against the test conditions in (Kirkhaug 2013) to investigate if any of these can be the cause to the large differences in abrasion rate between the two studies, as shown in Figure 43. In addition, the use of freshwater ice, instead of seawater ice, and its effect on the results has been discussed.

5.5.1 Effect of Vertical Load on Abrasion Resistance

The average vertical load is found to be close to constant over the accumulated distance for both of the specimens, as seen in Figures 44 and 45. An average of 4129 N and 3895 N, with standard deviations of 550 N and 772 N for specimens 12.1 and 22.1, respectively, are observed. This means that an average ice pressure of a little below 1 MPa has been used during testing. Since specimen 22.1, which had the higher abrasion rates, has a lower average vertical load, it is concluded that the vertical load is not the reason for these differences in abrasion rate. The average vertical load used in (Kirkhaug 2013) is also approximately the same as the load used here at about 4100 N.

Clearly, the ice abrasion rig has had problems delivering the requested load of 4300 N (1 MPa). A trend has been seen, for example in the testing of specimen 12.1 in Figure 44, that the quicker the ice is used up, the lower the average vertical load has been and with a relative high standard deviation. The abrasion rig also tends to keep the vertical load closer to the desired level at lower sliding velocities. An example of this can be seen in Figure 46, where specimen 31.1, with a sliding velocity of 0.16 m/s, has an average vertical load of 4215 N and a standard deviation of 482 N.

5.5.2 Effect of Sliding Velocity on Abrasion Resistance

The average sliding velocities are found to be very similar for specimens 12.1, seen in Figure 47, and 22.1, measured at 0.253 m/s and 0.251 m/s, respectively, both with a standard deviation of 0.025 m/s. These are both very close to the desired sliding velocity of 0.25 m/s. (Kirkhaug 2013) registered an average sliding velocity and standard deviation of 0.25±0.045 m/s. Specimen 31.1, which was supposed to hold a velocity of 0.16 m/s, shows, in Figure 48, an average velocity of 0.161 m/s with a standard deviation of 0.01 m/s. The sliding velocity seems to have been held constant at the desired level, independent of product type or sliding speed, but it is noticed that the variations in sliding velocity seem to be higher when the average sliding velocity increases.

5.5.3 Effect of Air and Ice Cylinder Temperatures on Abrasion Resistance

The average air temperature during testing is found to be about 1°C higher, at -8.8°C, for specimen 22.1 compared to specimen 12.1, which is at -9.7°C. This is seen in Figures 49 and 50. They both had standard deviations of 1.1°C. These temperatures are similar to the temperatures recorded by (Kirkhaug 2013), who had an average air temperature of about -9.7°C, as seen in Figure 51. The sensor for the air temperatures registered in this thesis was placed near the floor behind the ice abrasion rig. As cold air sinks, this may give misleading air temperature values, and it is recommended to mount this sensor at a more appropriate location in future tests. It is unknown where the sensor was placed during Kirkhaug´s measurements.

As seen in Figures 52 and 53, the temperature of the ice specimen cylinder varies between -2°C and -4°C. The average ice cylinder temperature during testing is found to be higher for specimen 22.1, at -3.2°C, about 0.5°C higher than for specimen 12.1, at -3.7°C. Both of them have a standard deviation of 0.8°C. An increase in temperature leads to a decrease in the hardness of ice, as shown in Figure 5. This excludes these parameters from being the reason for the large abrasion rate differences between the specimens, because specimen 22.1, which was tested during the highest temperatures, has the

highest abrasion rate. The ice cylinder temperatures during Kirkhaug´s tests are unknown.

The average air temperatures are a little bit above the desired air temperature of -10°C. This is most likely due to the activity in and out of the test room to change ice specimens during testing. It should be considered lowering the temperature in the room so that it stays at around -10°C with the activity in and out. The ice cylinder temperatures are also above the air temperature. The reason for this is because each time the ice is changed, the ice cylinder is heated up in order to get the old ice specimen out. Since the ice is changed as often as it is, it is possible that the cylinder only has time to cool down to around -4°C before it is heated up again.

With one of the test conditions during these tests being that the air temperature is -10°C, it is expected that the ice specimen has this same temperature. Clearly this is not the case, even though the room temperature is close to this, seeing that the temperature of the ice cylinder is a lot higher. As shown in Figure 5, the temperature of the ice affects the hardness, especially close to the melting point. Therefore, the effect of lowering the ice temperature during testing, by connecting an extra Julabo 2000 heating circulator to the ice specimen cylinder, is something that should be studied further.

5.5.4 Effect of Concrete Specimen Temperature on Abrasion Resistance

The temperature in the concrete specimen during testing has also been investigated. Due to the filling of epoxy in the copper bedding to stiffen up the system, as discussed in section 3.4, the temperature gradient in the concrete specimen has been altered. Before the system was improved, (Kirkhaug 2013) measured about 1.8°C, 1.1°C, and -0.4°C at, respectively, the bottom, center and top of the concrete specimen as seen in Figure 54. The average room temperature during this test is unknown, but is assumed to be around -10°C, as seen in Figure 51. The temperatures measured in the concrete specimen after the filling of epoxy are shown in Figure 55. These are about 5.5°C, 2.4°C and -0.5°C at the bottom, center and top. The room temperature during this test was at an average -11.1°C.

The surface temperature is approximately the same for both cases. On the other hand, the temperature in the rest of the concrete specimen is a lot higher for the specimen tested after the filling of epoxy. To clarify, the exact same specimen, from Kirkhaug´s work, with temperature sensors casted inside, has been used in both cases. It seems as though the copper plate is transferring more heat to the concrete specimen than before. Even though the surface temperatures are still the same, there might be a larger heat transfer from the concrete specimen to the ice specimen, which can be causing the ice to melt at the same time as it is abrading the concrete surface. This may be a possible explanation for the low abrasion values encountered in this thesis compared to (Kirkhaug 2013), and the heat transfer from the concrete to the ice is therefore a topic that should be studied further.

There is one observation that might support this theory of the ice melting because of higher heat transfer from the concrete during testing. It can be seen in Figures 44-46 that the load regularly drops close to 0 N. This happens when the ice has to be replaced, and the first logged values are small until the desired load is reached. This also shows how often the ice had to be replaced during the testing. The ice tended to vary in how long it lasted. As can be seen in Figure 44, the ice suddenly lasts a lot longer during the second half of the testing. Neither the air temperature in Figure 49, nor the ice cylinder temperature in Figure 52, show any changes that can explain this. Therefore, it is believed that this might have to do with the heat transfer from the concrete specimen to the ice specimen. The tendency of the ice varying in how long it lasted was one that reoccurred for many of the specimens, making it hard to understand exactly why this was the case.

It is found that for an effective sliding distance of 2.5 km, an average of 11 ice specimens is needed for the B70 reference concrete, 14 for the 0.5% steel fiber concrete, 21 for the 1.5% steel fiber concrete, 27 for the 1.5% polypropylene fiber concrete, and 11 ice specimens for the 1.5% basalt fiber concrete. These numbers clearly show an increase in ice consumption due to both steel and polypropylene fibers and indicate that these fibers are wearing the ice down. However, the low abrasion rates found in these tests compared to Kirkhaug´s are on the B70 reference concrete, and therefore this

wearing of the ice from the fiber reinforcement cannot be the only cause of these low rates.

In general, the ice consumption was a lot larger in the tests for this thesis compared to that of (Kirkhaug 2013). Based on Figures 85 and 86 in (Kirkhaug 2013), just six ice specimens were used on each concrete specimen for an effective sliding distance of 2.5 km. These two specimens were a B60 reference concrete and a Densit Wearflex 2000 repair mortar. The reason for this approximately triple increase in ice consumption in this thesis compared to Kirkhaug´s is believed to be a combination of the new heat flow in the concrete, and the addition of fiber reinforcement. The effect of both the heat flow and the addition of fibers on the consumption of ice is something that should be studied further to see if this is affecting the abrasion rates.

5.5.5 Effect of Freshwater Ice vs Seawater Ice on the Abrasion Results

A final comment on the test conditions of these experiments is the use of freshwater ice instead of seawater ice. Using seawater ice on the ice abrasion rig would introduce the hazard of parts of the rig rusting and not performing properly. This problem is easily avoided by using freshwater ice. The negative aspect is obviously that in reality there will be seawater ice abrading the concrete surface, which brings a degree of uncertainty towards the results of these tests.

In natural, cold-climate conditions, water has freezing temperature at the surface and thus predominantly one direction of heat flux, which results in most of the air being expelled into the water underneath as it freezes. The laboratory grown ice used in these experiments is made by filling plastic cylinders with water and placing them in -10°C. In this way the ice is only in contact with the air at the top-side of the cylinder. Thus, when the initial ice layer is created at the water surface, the air is trapped within the cylinder. This results in the ice having a lower density than natural freshwater ice.

As seen in section 4.1, the average density of the freshwater ice used in these experiments was about 904 kg/m^3, a bit lower than the theoretical density of freshwater ice, at 917 kg/m^3. When discussing the abrasion of concrete structures, it is the sea ice above the waterline that is important. This ice has a density in the range 840 to 910 kg/m^3, according to (Timco and Frederking 1996). In this regard,

it is concluded that, at least regarding the density of the ice, it is on the conservative side to use freshwater ice instead of seawater ice in these experiments. However, the effect of parameters such as salts and the formation of brine in seawater ice on the abrasion of concrete are unknown. Therefore, further research should be done on the effect of using freshwater ice instead of seawater ice in concrete abrasion experiments.

All in all, the general test conditions, including vertical load, sliding velocity and air and ice cylinder temperatures, have been kept approximately constant for the specimens tested in this thesis, and also compared to Kirkhaug´s tests. The only test condition that has been altered compared to Kirkhaug´s tests is the heat flow through the concrete specimen. This alteration is believed to possibly be part of the cause to the low abrasion rates found in this thesis compared to (Kirkhaug 2013). The use of freshwater ice instead of seawater ice has also been shown to be on the conservative side when it comes to the density and the hardness of the ice.

5.6 Wear Profiles

The wear profiles along the x-axis in Figures 62-64 show no clear trends on the abrasion rate along this axis, as was observed by (Itoh, Yoshida et al. 1988) who experienced a higher abrasion towards the center of the specimens. Figure 62 shows the abrasion increasing slightly towards the sides of specimen 2.1, while Figure 64 shows the abrasion both increasing and decreasing towards each side of specimen 21.2. The abrasion on specimen 32.2, in Figure 63, increases towards the center, similar to Itoh´s observations. Based on these examples, and the rest of the wear profiles presented in Appendix J, no conclusions can be drawn on the wear profile along the x-axis.

The wear profiles along the y-axis have also been studied. Figures 65-67 present these results. Based on measuring methods 1 and 2, specimen 1.2 seems to have a more or less homogeneous abrasion profile, while the abrasion on specimens 32.1 and 42.1 tends to vary a bit more, although not showing any clear trend. The tendency of increased abrasion on the edges of the specimens where the ice specimen turns, as observed by (Kirkhaug 2013), was not found in these abrasion tests.

5.7 Freeze-Thaw Resistance

None of the concrete mixes survived the ASTM C666 Procedure A freeze-thaw testing. Failure has occurred to all of the concrete mixes according to the durability factor because all of the relative moduli are less than 60% of the initial moduli, as seen in Table 11. The exact durability factor for each concrete mix has not been possible to calculate due to a lack of sufficient transverse frequency measurements during the freeze-thaw cycling, as mentioned in section 3.2. The reason for this lack of freeze-thaw durability in all the concrete mixes has been investigated by performing air-void measurements in the fresh concrete and in the hardened concrete, using both the PF-method and image analysis. It has been found that this failure to freeze-thaw exposure most likely is connected to the air content and structure in the concrete mixes.

A 4-6% air/macro pore content is usually needed for a concrete to be frost resistant (Jacobsen 2009). The results from the different air-void measurements, presented in Table 12, show that only two of the concrete mixes show an air content in this range; the B70 reference concrete and the concrete mix with 1.5% basalt fiber addition. These both have an air/macro pore content of 4.2% when averaging the results from the three different methods. The remaining three concretes lie in the range 2.4%-3.4%.

The spacing factor is another important parameter when determining if a concrete is frost-resistant. None of the concrete mixes fulfill the requirement for a good quality, frost-resistant concrete, of a spacing factor less than 0.20 mm (ASTM-C457). Also, only one of the concrete mixes, the mix with 1.5% steel fiber addition, fulfills ASTM´s requirement of a specific surface of the pores greater than 25 mm^{-1}.

All the concrete mixes also fail to fulfill the requirement for frost resistant concrete of a PF value larger than 25% (Jacobsen 2009). The concrete with addition of basalt fiber is close with a PF value of 24.4%, while the rest of the mixes are in the range 13.6%-22.1%.

Judging by the failure of all the concrete mixes to pass these requirements for a good quality, frost resistant concrete, it can be concluded that the reason that none of them passed the freeze-thaw testing is because of a poor air content and structure. The improvement in freeze-thaw durability observed by (Richardson,

Coventry et al. 2012) with the use of polypropylene fibers has not been observed in this thesis. This lack of freeze-thaw resistance may also be one of the reasons for lower abrasion rates compared to (Kirkhaug 2013). Unfortunately, any data on the freeze-thaw durability of the concrete mixes used by Kirkhaug has not been available, so this theory cannot be proven. Further research on the effect of the concretes freeze-thaw durability in regard to the abrasion resistance is recommended.

5.8 Accuracy and Reliability of Abrasion Measurements

In the following, the accuracy of the abrasion measurements is investigated and the reliability of the results discussed.

5.8.1 Correlation Between Similar Specimens

For these results to be trustworthy, a correlation between abrasion rates on specimens of the same product type and tested using the same test conditions should be observed. Since half of the specimens run at a sliding velocity of 16 cm/s are deemed misleading due to the use of the old measuring method, the correlation between specimens of the same product type run at this velocity cannot be investigated. Therefore, the correlation between specimens of the same product type, run at 25 cm/s is looked into. Half of these specimens have undergone an effective sliding distance of 5 km, but to omit the effect of extended sliding distances, the abrasion rates after 2.5 km effective sliding distance have been calculated for all of them.

Table 17 Abrasion rates on specimens of the same product type and test conditions

Specimens	Product Type	Test conditions	Abrasion rates (µm/km)
2.1 / 2.2	B70 Reference	1 MPa, 25 cm/s, -10°C, 2.5 km	10.8/2.7
12.1 / 12.2	0.5% Steel Fiber	1 MPa, 25 cm/s, -10°C, 2.5 km	1.9/5.0
22.1 / 22.2	1.5% Steel Fiber	1 MPa, 25 cm/s, -10°C, 2.5 km	8.8/9.4
32.1 / 32.2	1.5% Polyp. Fiber	1 MPa, 25 cm/s, -10°C, 2.5 km	6.4/6.5
42.1 / 42.2	1.5% Basalt Fiber	1 MPa, 25 cm/s, -10°C, 2.5 km	-5.9/4.1

Table 17 shows that the abrasion results are not very consistent. The two similar B70 Reference specimens, Specimens 2.1 and 2.2, tested under the same conditions, show abrasion rates of 10.8 µm/km and 2.7 µm/km, respectively. This is a 300% difference, which does not coincide with the expectations of these having a similar abrasion rate. The differences for the 0.5% steel, 1.5% steel, 1.5% polypropylene and 1.5% basalt specimens are 163%, 7%, 2% and -169%, respectively. Both the specimens with 1.5% steel and 1.5% polypropylene fiber additions show acceptable correlation. On the other hand, the other three product types show very different abrasion rates. This poor correlation leads to the question of how reliable these results are, which is discussed in the following section.

5.8.2 Accuracy of the Surface Measurements

The largest source of error, when it comes to the measurement technique, is believed to be the initial placement of the concrete specimen prior to measurements, which affects all of the measuring points. Figure 68, taken from (Greaker 2014), illustrates this. It shows the tip of the Mitutoyo digital indicator, which has a diameter of 1.8 mm, on the edge of a cavity on the concrete surface. A relocation of the tip can cause it to fall either deeper or completely into the cavity, which would give a very different measurement value. This means that if the initial placement of the concrete specimen, prior to measurements, has minor deviations compared to the placement during the previous measurement, it could cause large inaccuracies in the measurements. The situation shown in Figure 68

is a drastic example of the effect of these inaccuracies, but even though the measuring tip might not land on the edge of a cavity very often, it might land on a grain of sand or on a fiber that it did not land on in the previous measurement. With the abrasion values being in such a small scale as they are, especially compared to the *Average Roughness* parameters of the surfaces, such tiny inaccuracies in where the measuring tip lands for each measuring point, can play a large role in the accuracy of the results.

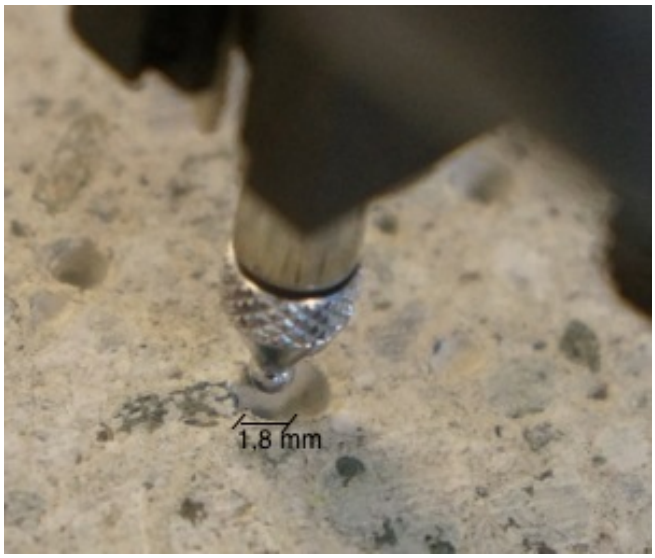

Figure 68 The tip of the Mitutoyo digital indicator, with a diameter of 1.8 mm, on the edge of a cavity (Greaker 2014)

The initial placement of the concrete specimen is done by the person doing the measurements. Even though this person is as careful as possible to place the concrete specimen in the exact same way for each measurement, deviations will occur from one measurement to the other, especially since these deviations can occur in any direction.

In order to get an idea of the accuracy of the surface measurements, Specimen 2.2 was measured a total of six times, consecutively. These measurements were all done without any abrasion being performed, meaning that with perfect measurement equipment and technique, these measurements would all be exactly the same. An inaccuracy of up to 0.003 mm is expected from the Mitutoyo digital indicator, so any larger inaccuracy is assumed to be due to the measurement

technique, which includes both the accuracy of the measuring table and the accuracy of the person handling the measurements.
The six measurements, each using 110 measuring points on the surface, done on specimen 2.2, before any abrasion, showed an average deviation of 0.004 mm with a standard deviation of 0.003 mm. This seems like a very good accuracy when taking into account the accuracy of the Mitutoyo digital indicator being 0.003 mm. However, these measurements were done consecutively, without any disturbances to the measuring table or the digital indicator in between measurements. During testing, the last measurements are done possibly several days following the initial measurements. In the meantime, the measuring table may have been used to do measurements on other specimens and the position of the digital indicator may have been altered, both possibly affecting the measurements.

To get a more realistic idea of the accuracy of these measurements, the deviations of the reference points between measurements, on the abraded specimens, have been studied. This means that the values of these reference points (the red and blue measuring points in Figure 29), before, during and after the concrete specimen has undergone abrasion, have been compared to eachother. These should have the exact same value before and after abrasion since they are outside of the abrasion zone. The problem is that they do not.

Comparing these reference points on the concrete specimens, before, during and after abrasion, an average deviation of 0.015 mm with a standard deviation of 0.015 mm is found. These are, respectively, four and five times larger than the deviations found on the six pre-abrasion measurements of specimen 2.2. Basically, this means that a single reference point tends to vary in a range of up to 0.04 mm between measurements, when in reality it should be showing the exact same value. This is a problem, seeing that most of the abrasion rates are approximately a tenth of this. This points towards the fact that the eventual disturbances of the measuring table in between measurements is affecting the accuracy of the measurements.

These large deviations of the reference points between measurements is the reason why the abrasion calculation methods 1 and 2, presented in section 3.6.2, have been used. These calculation methods use the differences between abraded measuring points and reference measuring points rather than the absolute values of each of these points.

To investigate if this calculation technique improves the accuracy of the abrasion measurements, the deviations of the differences between abrasion points and reference points have been calculated on the six pre-abrasion measurements of specimen 2.2. This will not give values of the real accuracy of the measurements, due to the fact that these measurements were performed consecutively and disregard the effect of disturbances to the measuring table in between measurements. However, it can indicate whether or not there is a basis for using the calculation methods chosen here.

The results show an average deviation of 0.003 mm with a standard deviation of 0.002 mm. This is an improvement of approximately 33% on the average deviation and 50% on the standard deviation compared to the previous results on these six measurements. To clarify, the difference now is that we are looking at the relationship between the measuring points in the abrasion zone and the reference points, instead of just looking at each point for itself, as earlier.

Clearly, there is an improvement in the accuracy of the abrasion measurements when using the differences between abraded points and reference points, instead of using the exact values of the abrasion points, before and after abrasion. Based on this discussion, it is concluded that to calculate abrasion, calculation methods 1 and 2 are the most appropriate.

As mentioned, the accuracy of these six consecutive measurements on specimen 2.2 is a lot better than the real accuracy of the measurements on the abraded specimens. Using the exact values of the measuring points gave an average deviation and standard deviation of 0.004 mm and 0.003 mm. When using the differences of these measuring points from the reference points, these deviations improved with 33% and 50%, respectively, as shown above. On the other hand, using the exact values of the reference points on the abraded specimens showed an average deviation and standard deviation that were both 0.015 mm. Based on the assumption that these deviations will improve, when using the differences between abraded points and the reference points instead of the exact values, with the same degree as seen on the six measurements of specimen 2.2, the following deviations are found in the abrasion measurements:

- Average deviation = 0.011 mm (33% improvement from 0.015 mm)

- Standard deviation = 0.010 mm (50% improvement from 0.015 mm)

This average deviation in the abrasion measurements is larger than any of the abrasion rates. The reliability of the results found in these tests is therefore questionable, due to the large inaccuracy of the surface measurements compared to the low abrasion values. In other words, not too much weight should be put on the ranking of the different fiber concretes in regard to their ice abrasion resistance. All of the rates found for the different concrete mixes are lower than the average deviation of the measurements. Therefore, the mixes showing a better ice abrasion resistance than the others may just as well be due to the inaccuracy of the measurements than to the actual ice abrasion resistant properties of the material.

6 Conclusion

This chapter presents some concluding remarks based on the various laboratory tests performed in this thesis and the discussion above.

- All of the fiber additions, except for the 1.5% steel fiber addition, have shown improved ice abrasion resistance compared to the B70 reference concrete, supporting various previous studies.
- The ranking of these different fiber concretes in regard to their ice abrasion resistance has been found to be difficult, due to the fact that the abrasion rates are all lower than the average deviation of the measurements. Therefore, the mixes showing a better ice abrasion resistance than the others may just as well be due to the inaccuracy of the measurements than to the actual ice abrasion resistant properties of the material.
- The inaccuracy in the measurement equipment and procedures used has been shown to be large compared to the abrasion rate values. The reliability of the results found in these tests is therefore found to be questionable.
- A poor correlation has been found between abrasion rates on specimens of the same product type and tested under the same test conditions, backing up the doubt on the reliability of these results.
- The maximum abrasion rate found in this report is 0.011 mm/km. The abrasion rates observed here are on average 11 times lower than the rates found in similar tests in (Kirkhaug 2013). Possible reasons for this may be the lack of freeze-thaw resistance and the altered heat flow in the concrete specimen during testing.
- It has been shown, through comparison of two specimens with, relatively, high and low abrasion rates, that the general test conditions, including vertical load, sliding velocity and air and ice cylinder temperatures, are not the reason for these differences in abrasion rate.
- A decreasing *Surface Average Roughness (S_a)* and *Root Mean Square Roughness (S_q)* have been shown to result in an increased abrasion rate, while no correlation has been found between *Surface Skewness (S_{sk})* or *Kurtosis (S_{ku})* in regard to abrasion rates.

- However, the accuracy of these roughness parameter values has been questioned due to the large distances between measuring points and systematical irregularities of the concrete surfaces.
- The addition of fiber reinforcement to the concrete mixes has not resulted in an improved freeze-thaw durability as expected based on previous studies. It has been found, through air void analysis, that the reason for this low concrete quality, in regard to freeze-thaw resistance, has been due to a poor air void content and structure in all of the concrete mixes.
- The use of freshwater ice instead of seawater ice has been shown to be on the conservative side when it comes to the density and the hardness of the ice.

7 Further Work

Ice abrasion of concrete is a relatively new and unexplored topic. A lot of further research into different areas of this subject, especially when it comes to which concrete properties that have the largest influence on abrasion resistance, is needed to get a proper understanding of this process. Following are a couple of suggestions for further research topics.

- The effect of various surface roughness parameters, among others the skewness and the kurtosis, on the ice abrasion resistance of concrete using a 3D optical scanner.
- The effect of different fiber types and dosages on concrete ice abrasion.
- The effect of concrete properties such as compressive strength, tensile strength, flexural strength and size and shape of the aggregate on the abrasion rate.
- The effect of ice properties such as density, temperature and hardness, on the abrasion rate.
- The effect of using freshwater ice instead of seawater ice in concrete ice abrasion experiments.
- The effect of the heat transfer from the concrete to the ice specimen on the abrasion rate.
- The effect of both the heat flow in the concrete specimen and the addition of fibers on the consumption of ice during ice abrasion tests.
- The effect of the concretes freeze-thaw durability in regard to the abrasion resistance.
- A more thorough discussion on the accuracy and reliability of the measurement equipment and procedures at the NTNU ice abrasion laboratory.
- The benefits, in regard to the accuracy and reliability of the abrasion measurements, of obtaining new measuring equipment at the NTNU ice abrasion laboratory.
- The use of a 3D optical scanner for abrasion measurements compared to the Mitutoyo digital indicator.

References

Archard, J. F. (1953). "Contact and Rubbing of Flat Surfaces." Journal of Applied Physics **24**(8): 981-988.

ASTM-C457 Standard Test Method for Microscopical Determination of Parameters of the Air-Void System in Hardened Concrete. West Conshohocken, PA, USA, ASTM International.

ASTM-C666 (2008). Standard Test Method for Resistance of Concrete to Rapid Freezing and Thawing. West Conshohocken, PA, USA, ASTM International.

ASTM-C779 Standard Test Method for Abrasion Resistance of Horizontal Concrete Surfaces. West Conshohocken, PA, USA, ASTM International.

ASTM-C1138 Standard Test Method for Abrasion Resistance of Concrete (Underwater Method). West Conshohocken, PA, USA, ASTM International.

Atis, C. D. and O. Karahan (2007). "Properties of steel fiber reinforced fly ash concrete." Construction and Building Materials **23**: 392-399.

Atis, C. D., O. Karahan, K. Ari, Ö. C. Sola and C. Bilim (2009). "Relation between Strength Properties (Flexural and Compressive) and Abrasion Resistance of Fiber (Steel and Polypropylene)-Reinforced Fly ash Concrete." Journal of Materials in Civil Engineering **21**: 402-408.

Barnes, P. and D. Tabor (1966). "Plastic Flow and Pressure Melting in the Deformation of Ice." Nature **210**: 878-882.

Bergdahl, L. (1977). Physics of ice and snow as aff. Gothenburg, Chalmers University of Technology, Dept. of Hydraulics.

Bloomfield, M. (2006, 26/11/2013). "Roughness Concepts." Retrieved 15, from http://homepages.rpi.edu/~bloomm2/roughness.pdf.

Cavdar, A. (2014). "Investigation of freeze-thaw effects on mechanical properties of fiber reinforced cement mortars." Composites: Part B **58**: 463-472.

Deleanu, L., C. Georgescu and C. Sucio (2012). "A Comparison Between 2D and 3D Surface Parameters for Evaluating the Quality of Surfaces." Technologies in Machine Building.

Dhir, R. K., P. C. Hewlett and Y. N. Chan (1991). "Near-surface characteristics of concrete: abrasion resistance." Materials and Structures **24**: 122-128.

Febrillet, N., A. Kido, Y. Ito and K. Ishibashi (2000). "Strength and Abrasion Resistance of Ultra-High Strength Steel Fiber Reinforced Concrete." 63-71.

Felekoglu, B., S. Türkel and Y. Altuntas (2007). "Effects of steel fiber reinforcement on surface wear resistance of self-compacting repair mortars." Cement and Concrete Composites **29**: 391-396.

Fiorio, B. (2005). "Wear characterisation and degradation mechanisms of a concrete surface under ice friction." Construction and Building Materials **19**(5): 366-375.

Fonseca, P. C. and G. W. Scherer (2013). Using image analysis to determine the air void structure of mortar and concrete. Princeton, NJ, Princeton University.

Gadelmawla, E. S., M. M. Koura, T. M. A. Maksoud, I. M. Elewa and H. H. Soliman (2002). "Roughness parameters." Journal of Materials Processing Technology **123**(1): 133-145.

GOM. (2013). "GOM Inspect." 2013, from http://www.gom.com/3d-software/gom-inspect.html.

Grdic, Z. J., G. A. T. Curcic, N. S. Ristic and I. M. Despotovic (2012). "Abrasion resistance of concrete micro-reinforced with polypropylene fibers." Construction and Building Materials **27**: 305-312.

Greaker, N. S. (2013). Ice Quality in Measurements of Concrete Ice Abrasion: Pre-study Project Thesis, Norwegian University of Science and Technology.

Greaker, N. S. (2014). Laboratory Measurements of Ice-Concrete Abrasion with Different Types of Ice Quality. Trondheim, NTNU.

Hamilton, G. M. and L. E. Goodman (1966). "The stress field created by a circular sliding contact." Journal of Applied Mechanics **33**: 371-376.

Hara F., e. a. (1995). Evaluation of the test methods of abrasion by ice movements on the surface of reinforced concrete structures. CONSECJ95: Concrete under Severe Conditions -Environment and loading, Sapporo.

Hertz, H. (1881). "Ueber die Berührung fester elastischer Körper." Pure and Applied Mathematics **92**: 156-171.

Horszczaruk, E. (2005). "Abrasion resistance of high-strength concrete in hydraulic structures." Wear **259**: 62-69.

Horszczaruk, E. K. (2009). "Hydro-abrasive erosion of high performance fiber-reinforced concrete." Wear **267**: 110-115.

Huovinen, S. (1993). "Abrasion of Concrete Structures by Ice." Cement and Concrete Research **23**: 69-82.

Itoh, Y., Y. Tanak and H. Saeki (1994). Estimation method for abrasion of concrete structures due to sea ice movement. International Offshore and Polar Engineering Conference, Osaka.

Itoh, Y., A. Yoshida and M. Tsuchiya (1988). An Experimental Study on Abrasion of Concrete Due to Sea Ice. Offshore Technology Conference. Houston, Texas.

Jacobsen, S. (2009). Frost Deterioration. TKT 4215 Concrete Technology 1. Trondheim.

Jacobsen, S., A. Bekker, T. Uvarova, E. Pomnikov and K. T. Fosså (2012). Concrete Ice Abrasion: Deterioration Mechanisms, Testing and Modeling . International Congress on Durability of Concrete. Trondheim, Norway.

Jacobsen, S., K. Sætre and N. S. Greaker (2013). The NTNU Concrete-Ice Abrasion Laboratory. Concrete Innovation Conference 2014. Oslo.

Jacobsen, S., G. Scherer and E. Schulson (2013). Concrete Ice Abrasion Mechanics.

Kabay, N. (2014). "Abrasion resistance and fracture energy of concretes with basalt fiber." Construction and Building Materials **50**: 95-101.

Kirkhaug, J. R. (2013). Ice Abrasion and Bond Testing of Repair Mortars and High Performance Concrete. Master Master, Norwegian University of Science and Technology.

Kobrick, R. L., D. M. Klaus and K. W. Street (2011). "Validation of proposed metrics for two-body abrasion scratch test analysis standards." Wear **270**(11-12): 815-822.

Kvaerner. (2014). "http://www.Kvaerner.com." Retrieved 15.05, 2014.

Leising, C. (2010) "Surface Roughness of Concrete with 3D Profilometry."

Li, W. and J. Xu (2009). "Mechanical properties of basalt fiber reinforced geopolymeric concrete under impact loading." Materials Science and Engineering A **505**: 178-186.

Maage, M. (1977). Mechanical Wear on Fiber-reinforced Concrete. Nordforsk, Stockholm.

Mitutoyo. (2005). "Digimatic Indicators." from http://www.mitutoyo.com/wp-content/uploads/2012/11/1824˙DigimaticIndicators.pdf.

Møen, E., S. Jacobsen and H. Myhra (2007). Ice abrasion data on concrete structures - an overview. SINTEF Building and Infrastructure. SINTEF. Trondheim, NTNU.

Mu, R., W. Sun, X. Luo and C. Miao (2002). "Effect of chloride salt, freeze-thaw cycling and externally applied load on the performance of the concrete." Cement and Concrete Research **32**: 1859-1864.

Nanni, A. (1989). "Abrasion Resistance of Roller Compacted Concrete." ACI Materials Journal **86(6)**: 559-565.

Nawwar, A. M. and V. M. Malhotra (1988). "Development of a Test Method to Determine the Resistance of Concrete to Ice Abrasion and/or Impact." **109**: 401-426.

Olivito, R. S. and F. A. Zuccarello (2007). "An experimental study on the tensile strength of steel fiber reinforced concrete." Composites: Part B **41**: 246-255.

Petrovic, J. J. (2003). "Review: Mechanical properties of ice and snow." Journal of Material Science **1**.

Pettit, G. J. L. (2003). ABRASION TEST METHODS FOR PAVING UNITS COMPARED. The 7th International Conference on Concrete Block Paving, Sun City, South Africa.

Richardson, A. E., K. A. Coventry and S. Wilkinson (2012). "Freeze/thaw durability of concrete with synthetic fibre additions." Cold Regions Science and Technology **83-84**: 49-56.

Rognlien, B. (2013). Kvaerner Concrete Solutions Presentation at NTNU.

Sætre, K. (2013). Ice Abrasion of Concrete - Roughness analysis of ice-abraded concrete surfaces using 3D optical scanning. Trondheim, NTNU.

Santos, P. M. D. and E. N. B. S. Julio (2013). "A state-of-the-art review on roughness quantification methods for concrete surfaces." Construction and Building Materials **38**: 912-923.

Sedlacek, M., B. Podgornik and J. Vizintin (2009). "Influence of surface preparation on roughness parameters, friction and wear." Wear **266**(3-4): 482-487.

Sedlacek, M., B. Podgornik and J. Vizintin (2012). "Correlation between standard roughness parameters skewness and kurtosis and tribological behaviour of contact surfaces." Tribology International **48**: 102-112.

Sellevold, E. J. (2008). Chapter 8 - Porosity, pore structure. TKT 4215 Concrete Technology 1. Trondheim.

Siddique, R., K. Kapoor, E.-H. Kadri and R. Bennacer (2012). "Effect of polyester fibres on the compressive strength and abrasion resistance of HVFA concrete." Construction and Building Materials **29**: 270-278.

Siewczynska, M. (2012). "Method for determining the parameters of surface roughness by usage of a 3D scanner." Archives of Civil and Mechanical Engineering **12**(1): 83-89.

Skjølsvold, O. (2014). Memo - Test specimens for ice abrasion testing. Trondheim, SINTEF Byggforsk.

Sun, W., Y. M. Zhang, H. D. Yan and R. Mu (1999). "Damage and damage resistance of high strength concrete under the action of load and freeze-thaw cycles." Cement and Concrete Research **29**: 1519-1523.

Sun, Z. and Q. Xu (2009). "Microscopic, physical and mechanical analysis of polypropylene fiber reinforced concrete." Materials Science and Engineering A **527**: 198-204.

Tayebi, N. and A. A. Polycarpou (2004). "Modeling the effect of skewness and kurtosis on the static friction coefficient of rough surfaces." Tribology International **37**(6): 491-505.

Thomas, T. R. (1999). Rough Surfaces 2nd ed. London, Imperial College Press.

Timco, G. W. and R. M. W. Frederking (1996). "A review of sea ice density." Cold Regions Science and Technology **24**: 1-6.

Timco, G. W. and W. Weeks (2009). "A review of the engineering properties of sea ice." Cold Regions Science and Technology.

Topcu, I. B. and M. Canbaz (2006). "Effect of different fibers on the mechanical properties of concrete containing fly ash." Construction and Building Materials **21**: 1486-1491.

Yun, Y. and Y.-F. Wu (2011). "Durability of CFRP-concrete joints under freeze-thaw cycling." Cold Regions Science and Technology **65**: 401-412.

Appendices

Appendix A

Aggregate Grading EN 933-1

Table A.1 Aggregate grading

Aggregate	Residue, %, on sieve									
	0.125	0.25	0.5	1	2	4	8	11.2	16	32
Årdal 0-8 mm	93.8	86.8	75.2	57.2	37.1	19.6	2.3	0		
Årdal 8-16 mm	100	100	100	100	100	100	97	72.1	12.1	0
Combined aggregate	97.0	93.7	88.1	79.5	69.8	61.4	51.5	37.5	6.3	0

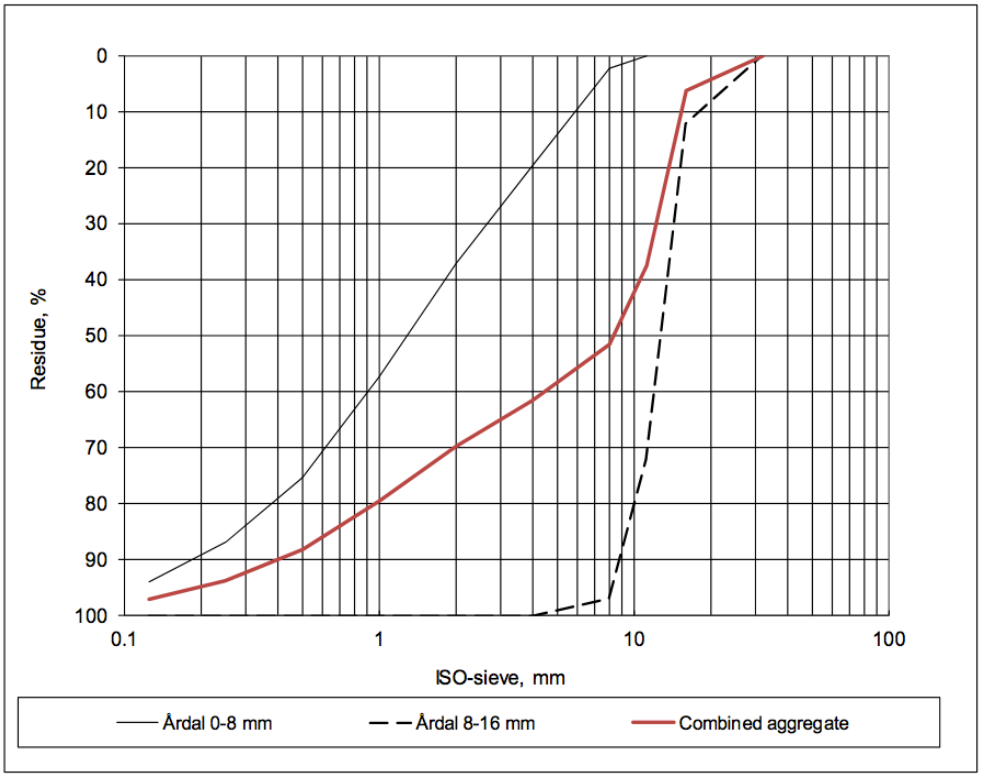

Figure A.1 Aggregate grading

Appendix B

Quick Guide to the Ice Abrasion Rig and Test Procedures, taken and improved from (Kirkhaug 2013)

This appendix is a quick guide on how to use and operate the NTNU ice abrasion rig. The rig is built at NTNU and the experience performing the tests of this study and previous studies has given a great insight on how the abrasion rig works. This includes the everyday operating procedures and how to avoid problems, resulting in a more efficient test process. Various problems and unforeseen events that occurred during testing are described in order to be be avoided in the future.

The following equipment and tools should be available when using the ice abrasion rig: silicone-based lubricant, oil, wrench, mallet, flat-head screwdriver, gaffer tape, anti-freeze liquid (spray bottle) and extra rubber rings.

1 Ice

One of the first things that should be done is to make ice. This could be done either by drilling out cores from ice sheets or by filling plastic cylinders with water and freezing them. If the latter method is chosen, there are a couple of things to be aware of. Firstly, there should be made enough ice before testing is started, so that unwanted stops in testing is avoided. Secondly, the volume expansion when water freezes to ice generates large forces on the plastic cylinder used to make ice specimens. Therefore, it is important to not fill the plastic cylinders to the top, but leave approximately 2 cm of open space at the top. This way, the cracking of the plastic cylinders is mostly avoided. If they do crack, however, gaffer tape can be used to seal the cracks. This is also important in regard to the height of the ice specimens. If the plastic cylinders are filled to the top, the ice specimens end up being to high for the ice container in the ice abrasion rig.

Ice can be stored in the ice abrasion laboratory. However, ice that is stored over longer periods of time has a tendency to melt, even

though the temperature is -10°C. This might be due to the large activity of going in and out of this room when operating the rig, causing warm air to regularly stream in and melt the ice. Ice should therefore not be stored more than one week before it is used for testing.

Another challenge is that the fuse, for the circuit where the temperature regulator is connected, can blow for no apparent reason. The ice abrasion laboratory is well insulated and a blown fuse during the night is not too critical. However, if the fuse is not turned back on within a day or so, all the stored ice will melt completely. It is therefore recommended to store ice in the freezer for periods when the laboratory is not kept under regular observation. This fuse, however, was replaced before the performed tests of this thesis and no problems occurred during these tests.

2 Testing

After completing initial surface treatment and measurement, the specimen is ready to be mounted in the ice abrasion rig. If the specimen is taken straight from room temperature, the concrete surface is going to be warm. Placing it in the freezer about 30 minutes before testing is found to reduce the surface temperature to approximately 0°C.

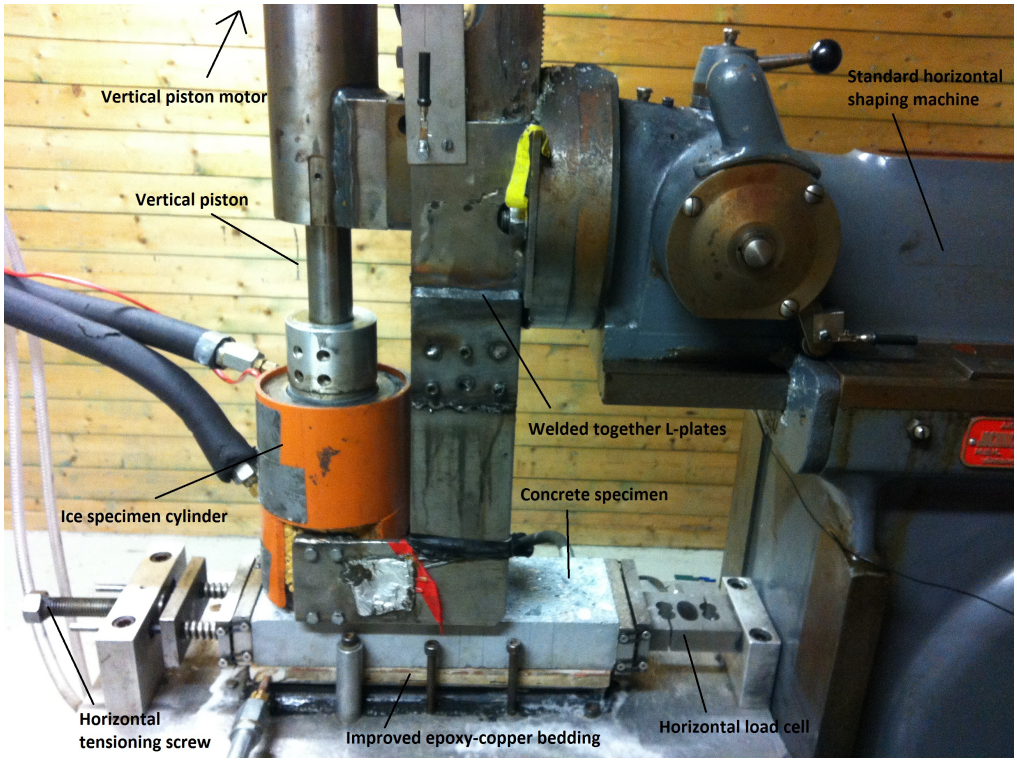

Figure B.1 NTNU ice abrasion rig

Test specimens are placed on the copper plate and, before tightening the tensioning screw, seen to the left in Figure B.1 the vertical load cells need to be calibrated. This is done so that the load cells can register the applied ice load. Calibration is done by entering the calibration tab in the Labview program. In the calibration tab, click on the "Zero" button for both of the vertical load cells, shown at the bottom of Figure B.2.

When the vertical load cells have been calibrated, the tensioning screw is tightened to about 1500N. This keeps the specimen in place during testing in order to get meaningful values of horizontal load and friction. When the tensioning screw has been tightened, the horizontal load cell, seen at the top of Figure B.2, needs to be calibrated.

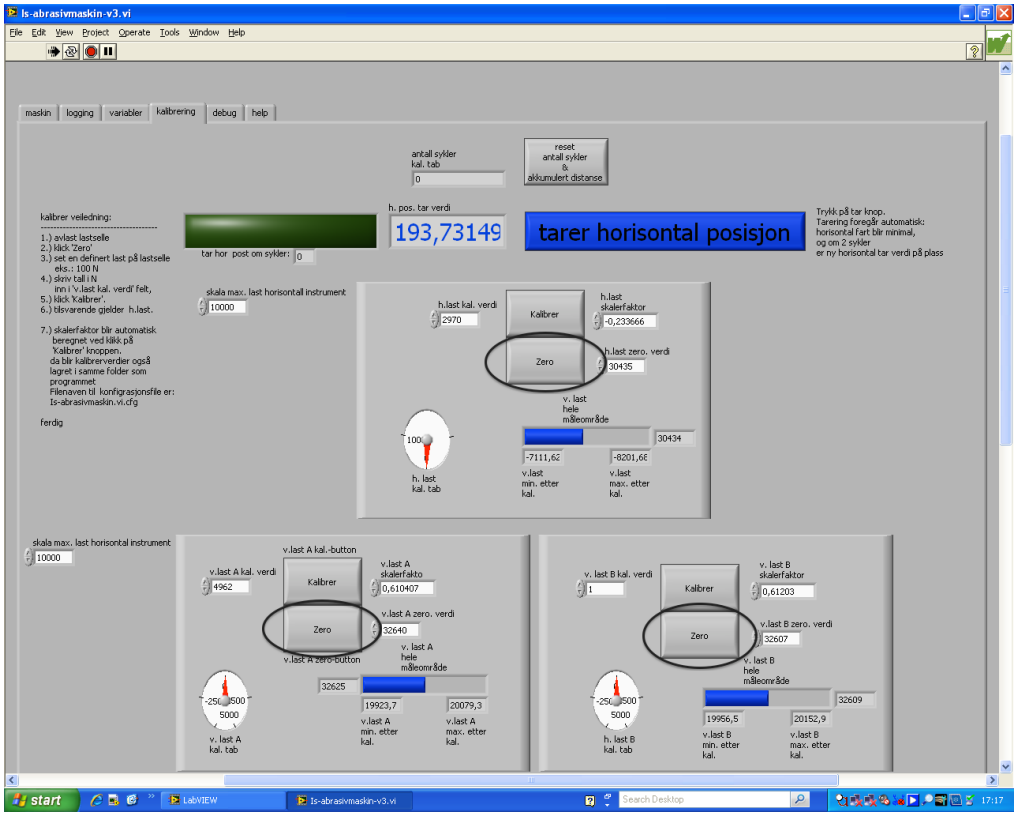

Figure B.2 Calibration tab in Labview

After calibration is performed, the ice can be placed in the ice container and the bedding with the concrete specimen could be swung back under the ice using the horizontal motor. It is important that the concrete specimen is placed with its center under the center of the ice specimen. If the concrete specimen is casted with temperature sensors, these need to be connected.

To get meaningful results, test parameters and test settings need to be decided and entered into the Labview program. Sampling rate can be chosen in the "Logging" tab of the Labview program, shown in Figure B.3. Available options are frequency, up to 10 Hz, or cycle controlled logging.

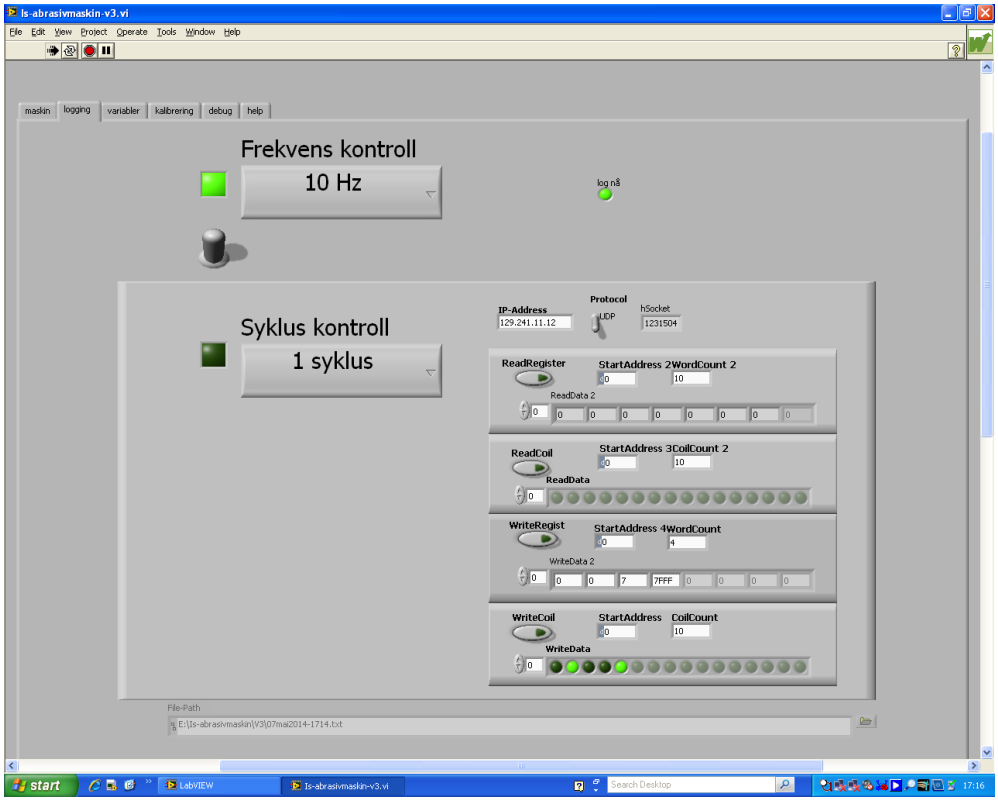

Figure B.3 Logging frequency tab in Labview

The following parameters that are to be entered in Labview are shown in Figure B.4. Contact pressure is entered as a load, [N], and can be found by multiplying desired contact pressure with the surface area of the ice specimen, which is 4300 mm^2. For example, 1 MPa = 4300 N. It was experienced, however, that the abrasion rig has trouble delivering the desired load. Therefore, a load of 4500 N was entered in Labview for specimens run at 16 cm/s and a load of 4700 N was entered in Labview for specimens run at 25 cm/s. This still did not give the desired load of 4300 N, as seen in Figures 44-46. Therefore, it should be considered entering higher load values in Labview to achieve the desired load of 4300 N.

Vertical gain [mm] and vertical speed (rpm) have to be set in order for the ice abrasion rig to be able to apply load. A low gain and high vertical speed is preferable to get as stable a load as possible. This way, the rig adjusts the piston quickly and often. A vertical speed of about 600 rpm and a vertical goain of 0,02 mm is found to provide a

stable loading. Increasing the vertical speed may result in overheating of the vertical engine, which should be avoided.

The next parameter to be set in Labview is the horizontal sliding velocity. This is entered as rpm in the "Horisontal Turtall" box. An rpm of 850 is found to give a velocity of approximately 16 cm/s, while an rpm of 1330 provides a velocity of approximately 25 cm/s.

Finally, sliding distance needs to be entered for when the rig should stop automatically. Unless this parameter is set, the rig runs until the ice is consumed or until it is stopped manually. It is important to keep in mind that the distance entered here is not the effective sliding distance, as explained in section 3.6.3. If an effective sliding distance of 2,5km is desired, a distance of 6757m (2500/0,37) needs to be entered in this box.

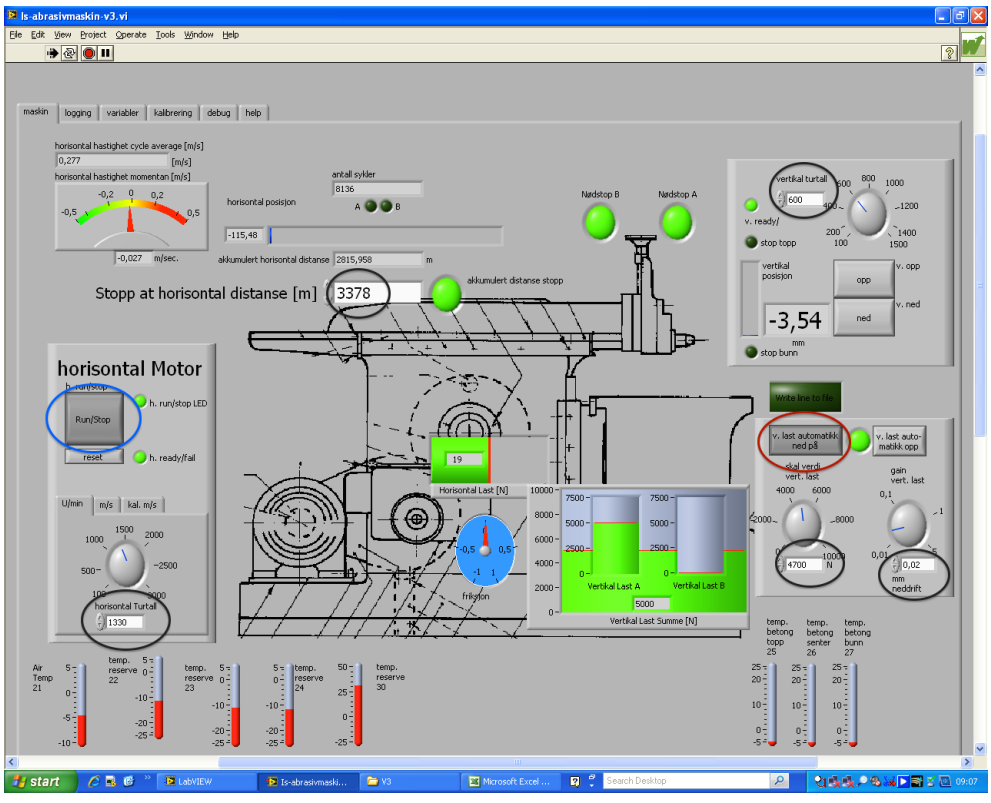

Figure B.4 The main operating window in Labview

To avoid water from freezing on the test specimen surface, the Julabo heating circulator, shown in Figure B.5, needs to be switched on. The

temperature should be adjusted so that the copper plate transfers enough heat to keep the concrete surface at a temperature of about 0°C. Different concretes will have different heat transfer properties. Specimens with temperature sensors should be used to find the correct temperature of the heating circulator. Alternatively, an infrared temperature gun can be used to measure the temperature on the surface. The products tested in this study were found to need a temperature in the range of 11-12°C to avoid freezing on the surface. The gauges that circulate to the copper bedding can ke kept open constantly. On the other hand, the gauges that circulate to the ice specimen container need to be closed before testing. These are only to be opened, for as short a period as possible, when the ice needs to be switched.

Figure B.5 Julabo 2000 heating circulator

Before starting the test, the "v. last automatikk ned på" button, marked with a red circle on Figure B.4, needs to be pressed. If this is not done, no load will be applied and the ice will move back and

forth without any load. After this button is pressed, the sensors registering the vertical load start to increase. Pay close attention to these, and when the vertical load has reached approximately 1000N, start the testing by pushing the "Run/Stop" button, marked with a blue circle in Figure B.4. The rig now runs by itself until the desired distance is reached or until the ice is consumed and needs to be changed.

When the ice is fully consumed or the desired distance is reached, the rig automatically sets the horizontal sliding speed to 400 rpm and vertical speed to 1350 rpm so that the piston can be reversed to its top position. However, the rig does not stop automatically, so it is important to remember to stop the rig by pressing the "Run/Stop" button. An eye should be kept on the rig when the position of the vertical piston gets close to zero. For some reason the reversing seems to hang up from time to time. If the vertical engine is not stopped when this happens it could cause the engine to overheat and burn up. This is found to be avoided by stopping the engine and reducing the vertical speed before restarting the engine again.

To get the old ice out of the ice container, the gauge on the heating circulator, on the circuit connected to the ice specimen container, should be opened for half a minute or so. Then the ice melts enough to be removed and replaced. A mallet can be used on the ice to help speed things along. Remember to close the gauge to avoid the new ice to melt. Also, remember to calibrate the horizontal and vertical load cells each time a new ice specimen is placed in the rig. Especially the horizontal load cells tend to loosen up a bit during testing, causing them to not be zeroed out at the beginning of the next testing. Remember also to readjust the values for horizontal and vertical speed, since these have automatically been altered when the ice specimen came to its end.

3 Things to Remember/ Precautionary Measures

The experiments have been delayed due to many unforeseen events and problems. These are explained in this section in order to be able to deal with similar problems in a quicker manner in the future.

The rig is sealed between the bedding where the concrete specimen lies and the vertical load cells. This is to prevent water from leaking and freezing on the load cells, which can result in the load cells not registering the load properly. If this happens, the rig will try to adjust the load by pushing down the piston even more, but as long as the load is not being registered by one or both of the cells, the vertical engine will end up overloading. This can result in the engine having to be replaced. To prevent the sealing from leaking, an anti-freeze liquid should be sprayed on this sealing before each testing so that ice does not freeze directly on the sealing. There will still end up freezing ice around the sealing, but when removed it will not pull the sealing with it when anti-freeze spray is used. To remove the ice it is best to use the mallet and crush it, which makes it easier to remove.

The sealing should be repaired when necessary, and it should also be considered to install some sort of heating on the plates under the concrete specimen bedding to prevent any formation of ice.

In the beginning of testing for this thesis, there arised problems with the vertical piston. It was having trouble delivering the necessary force of 4300N to the concrete specimen. It was tried to increase the vertical speed and gain, but this did not help. Therefore it was decided that the motor probably was not working properly, so a new motor was ordered and installed. This did not solve the problem and it was concluded that maybe the load cells were not registering the load properly. The vertical load cells were then tested with an external load cell and they were discovered to be working properly. Once again a new motor was ordered and installed, this time a more powerful one. After it had been installed it was discovered that a new converter was needed with this new motor, so this was ordered and installed also. But still, the load cells were not registering the desired load.

Finally, the entire abrasion rig was dismantled, in order to find out what was causing this problem. It was found out that some of the screws had been tightened too much. This had caused the track where the vertical piston slides up and down to be too narrow. Therefore, the vertical piston was not moving freely in this track and could not exert the desired force. The abrasion rig was rebuilt and the testing could continue.

This next problem occurred during Kirkhaug´s testing, but not during the testing in this thesis. When an ice specimen is consumed,

the rig is supposed to set horizontal velocity to 400 rpm and reverse the piston to its top position. After some while of testing the rig was unable to reverse the piston automatically. A temporary solution that seemed to work was to stop the rig manually and use a lower vertical speed (800-1000 rpm) when reversing the piston. However, after doing this for a while it became impossible to adjust the piston at all.

One likely cause of this problem is that the repeated movement up and down lead to large friction on some of the components and they were practically welded together. In addition, one component needed for adjusting vertical position of the piston had fallen out. Because of this the rig had to be dismantled and rebuilt. The rig has been working fine after this, but no components have been replaced, and the problem could therefore reoccur. Using silicon based lubricant on the vertical moving parts once a day or so is used as a solution to prevent this problem. If it should reoccur, there is little that can be done and there should be kept an eye on it when ice level is getting close to zero and the rig is entering "maintenance" mode. If the piston is not reversed automatically, the laboratory staff (Steinar or Gøran) should be contacted to assess the situation.

In the last part of the tests of Kirkhaug´s study, the ice abrasion rig shut down completely, blowing the main fuse every time it was restarted. After troubleshooting this problem from many angles the solution was found to be quite simple. As the vertical piston is moving up and down, the insulation of the cable to the sensor indicating vertical position of the piston, had been chewed up, causing a short circuit of the electrical system. The problem was fixed by applying some electrical tape on the damaged cable, and it should be easy to prevent this from happening again if there is kept an eye on the cable. This problem also affected some of the computer chips in the control unit, which had to be replaced.

The sensor which registers the vertical position of the piston is fastened relatively loosely to the rig. It happened more than once that the vibration from the rig made it alter its position. It is therefore important to be in the proximity of the test rig when ice level is closing down to zero, to make sure the piston is not pushed too far down.

The bedding where the test specimens are mounted is driven back and forth to be able to mount new concrete specimens or change ice.

The track it slides on should be lubricated with oil in the following situations:

- After the temperature in the ice abrasion laboratory has been higher than 0°C.
- Once a week in periods of testing, or before testing if it has been a while since the rig has been used.

The ice abrasion rig is built of many individual components, which are carefully put together. Vibrations and other stresses have been found to loosen screws. Therefore, all visible screws should be checked and tightened regularly to avoid any unnecessary damage to the rig. Also the rubber stretches used on the plate in front of the horizontal load cell should be kept an eye on. These seem to get brittle due to the low temperatures and have to be replaced regularly. Make sure to always have some extra on hand.

A time efficient tip is to connect the laboratory computer to the internet and create a Teamviewer account. The computer is easily connected to internet using a wireless LAN USB-disc. By installing Teamviewer and connecting the computer to your account, tests can be monitored also outside of the laboratory on the Teamviewer account. This makes it possible to do other work in the laboratory and still be able to respond quickly to the ice abrasion tests.

A new log file is created each time the "Automatisk last ned" button is hit. Values like distance and number of cycles are continued to be counted in the next log file. However, if the Labview software is restarted, values are counted from zero again. This should be done if new specimens are to be tested. It is also important to have an organized system of sorting the log files for different specimens, as the number of files can become high and difficult to have a good overview over.

4 Summary of Ice Abrasion Test Procedure (Improved from (Kirkhaug 2013)):

1. Make ice minimum 24 hours before testing.
2. Enter desired temperature of the laboratory on the Pego 2000 Expert control unit.
3. Perform pre-abrasion surface measurement.
4. Switch on the heat flow from the Julabo 2000 heating circulator to the copper bedding and decide the temperature.
5. Decide test conditions and enter these into Labview: average ice pressure, sliding velocity, sliding distance(=effective sliding distance/0,37), vertical rotational speed, vertical gain and logging frequency.
6. Mount test specimens on the copper bedding and pretension the concrete specimens (Horizontal load ≈ 1500 N).
7. Calibrate vertical and horizontal load cells.
8. Insert ice in the ice specimen cylinder.
9. Turn on the motor that moves the test specimen to under the ice cylinder.
10. Make sure there is a small gap (≈2 mm) between the ice specimen cylinder and concrete specimen. If not, the concrete specimen has to be plane cut to a smaller thickness. If the gap is too large, use one of the steel plates(2 or 3 mm) between the copper bedding and test specimen.
11. Push the apply vertical load button in Labview.
12. When the vertical load cells start receiving pressure from the ice, hit the Run/Stop button in Labview.
13. The rig now runs automatically until the wanted sliding distance is reached or until the ice has to be changed.
14. When the wanted sliding distance is reached or the ice has to be changed, the ice abrasion rig enters maintenance mode, adjusting the horizontal velocity to 400 rpm and the piston that applies load to the ice is reset to its top vertical position.
15. Stop the horizontal movement by hitting the Run/Stop button.
16. Before removing the ice, open the gauge on the heating circulator to the ice specimen cylinder circuit so that the ice

can be removed.

17. Use a mallet to give the ice a stroke if necessary. This makes the removal faster. When the ice is removed, close the gauge on the heating circulator to the ice specimen cylinder right away.
18. Insert new ice.
19. Reset vertical rotational speed and horizontal velocity (since these have automatically been adjusted when the rig entered maintenance mode).
20. Hit the Run/stop button and continue testing by performing steps 5-19 until desired distance is reached.
21. Remove concrete specimen from the bedding.
22. Measure abrasion.
23. Obtain log file. Log files should be obtained immediately and archived in a well- organized system for each specimen.
24. Remember to lubricate the described moving parts on the rig.
25. Keep an eye on ice growth on vertical load cells.

Appendix C

Detailed Freeze-Thaw Results

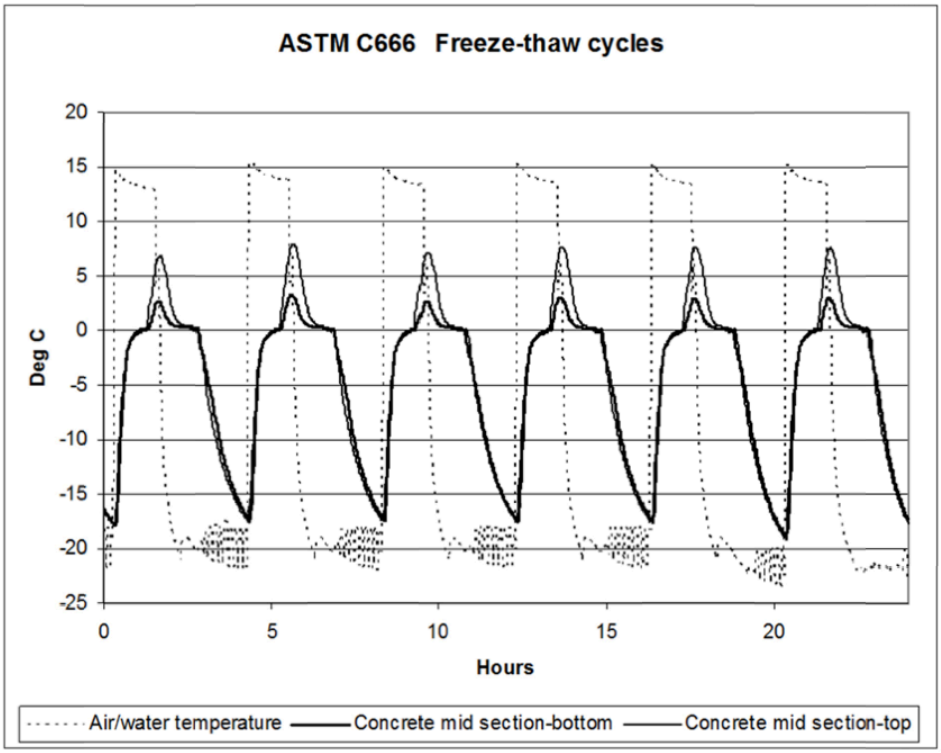

Figure C.1 Temperature in concrete specimens during freeze-thaw exposure

Table C.1 Transverse frequency of concrete specimens

No of cycles	Transverse frequency (n), Hz									
	1	2	11	12	21	22	31	32	41	42
0	3165	3165	3145	3086	3086	3165	3086	3165	3086	3067
155	1950	1630	1786	No result	2076	2101	No result	2039	1947	2408
300	1399	No result	1947	No result	2321	1959	No result	2133	1347	No result

Table C.2 Relative Dynamic Modulus of Elasticity

No of cycles	Relative Dynamic Modulus of Elasticity, n^2/n_0^2 (%)									
	Mix 1		Mix 2		Mix 3		Mix 4		Mix 5	
	1	2	11	12	21	22	31	32	41	42
0	100	100	100	100	100	100	100	100	100	100
155	38	27	32		45	44		42	40	62
300	20		38		57	38		45	19	

Appendix D

Ice Density Calculation (Greaker 2013)

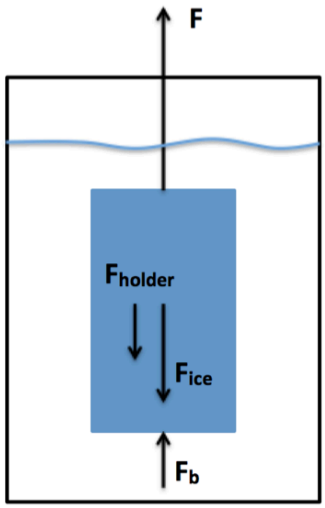

Figure D.1 Forces acting on ice and holder submerged in kerosene

$$\begin{aligned} \sum F &= 0 \\ F &= F_{ice} + F_{holder} - F_b \end{aligned} \tag{C.1}$$

$$\begin{aligned} F &= m_{ice+holder,ker} \times g \\ F_{ice} &= m_{ice} \times g \\ F_{holder} &= m_{holder,air} \times g \\ F_b &= \rho_{ker} \times V_{disp} \times g \end{aligned} \tag{C.2}$$

$$\begin{aligned} \rho &= \frac{m}{V} \\ V_{disp} &= V_{ice} + V_{holder} \\ &= \frac{m_{ice}}{\rho_{ice}} + V_{holder} \end{aligned} \tag{C.3}$$

$$\begin{aligned} m_{ice+holder,ker} \times g &= m_{ice} \times g + m_{holder,air} \times g - \rho_{ker} \times V_{disp} \times g \\ m_{ice+holder,ker} &= m_{ice} + m_{holder,air} - \rho_{ker} \times (\tfrac{m_{ice}}{\rho_{ice}} + V_{holder}) \\ \rho_{ker} \times \tfrac{m_{ice}}{\rho_{Ice}} &= m_{holder,air} + m_{ice} - m_{ice+holder,ker} - \rho_{ker} \times V_{holder} \\ \rho_{ice} &= \frac{\rho_{ker} \times m_{ice}}{m_{holder,air} + m_{ice} - m_{ice+holder,ker} - \rho_{ker} \times V_{holder}} \end{aligned} \tag{C.4}$$

$$m_{ice} = m_{ice+holder,air} - m_{holder,air} \tag{C.5}$$

$$\rho_{ice} = \frac{m_{ice+holder,air} - m_{holder,air}}{m_{ice+holder,air} - m_{ice+holder,ker} - \rho_{ker} \times V_{holder}} \times \rho_{ker} \tag{C.6}$$

Volume of holder, V_{holder}

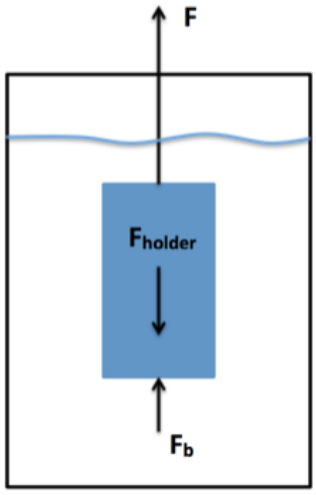

Figure D.2 Forces acting on holder submerged in kerosene

$$F = F_{holder} - F_b \tag{C.7}$$

$$\begin{aligned} F &= m_{holder,ker} \times g \\ F_{holder} &= m_{holder,air} \times g \\ F_b &= \rho_{ker} \times V_{holder} \times g \end{aligned} \tag{C.8}$$

$$m_{holder,ker} \times g = m_{holder,air} \times g - \rho_{ker} \times V_{holder} \times g \tag{C.9}$$

$$V_{holder} = \frac{m_{holder,air} - m_{holder,ker}}{\rho_{ker}} \tag{C.10}$$

Appendix E

Ice Density Data

Table E.1 Ice density data

Spec. #	Temp, C	ρ_ice_theoretical	ρ_ker	M_holder_air (g)	M_ice+holder_air (g)	M_holder_ker (g)	M_ice+holder_ker (g)	ρ_ice	Porosity	V_holder
1	-6,9	917,97	761	33,14	606,12	30,26	124,22	904,83	1,43%	3,78E-06
2	-7,0	917,98	761	33,25	604,45	30,35	123,81	904,38	1,48%	3,81E-06
3	-7,5	918,05	761	33,25	601,98	30,36	122,85	903,31	1,61%	3,80E-06
4	-7,3	918,02	762	33,23	603,67	30,36	123,2	904,69	1,45%	3,77E-06
5	-7,4	918,04	762	33,22	611,4	30,38	123,48	902,96	1,64%	3,73E-06
6	-7,4	918,04	762	33,25	610,88	30,38	124,02	904,07	1,52%	3,77E-06
7	-7,6	918,07	762	33,26	618,52	30,39	124,08	901,97	1,75%	3,77E-06
8	-7,5	918,05	762	33,28	603,13	30,39	122,6	903,64	1,57%	3,79E-06
9	-7,4	918,04	762	33,29	598,69	30,39	121,95	903,71	1,56%	3,81E-06
10	-7,2	918,01	762	33,3	598,62	30,39	121,65	903,15	1,62%	3,82E-06

Notes: ker=kerosene, M=mass, V=volume, ρ= density (kg/m^3)

Appendix F

Concrete Specimens After Freeze-Thaw Testing According to ASTM C666 Procedure A

Figure F.1 Concrete Mix 1 after 300 freeze-thaw cycles

Figure F.2 Concrete Mix 2 after 300 freeze-thaw cycles

Figure F.3 Concrete Mix 3 after 300 freeze-thaw cycles

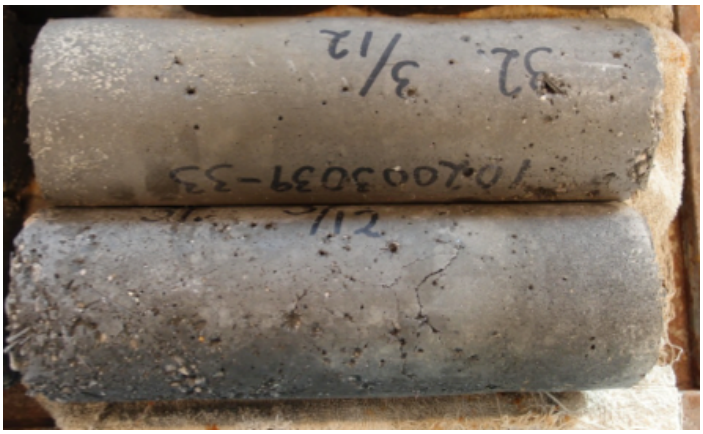

Figure F.4 Concrete Mix 4 after 300 freeze-thaw cycles

Figure F.5 Concrete Mix 5 after 300 freeze-thaw cycles

Appendix G

PF-test Data

Table G.1 PF-test data

Sample	W1 (105°C)	W2 (saturated)	Weight in water	Volume (mL)	W3 (pressure sat.)	ε tot	ε suc	ε air	% air	PF
B70 Reference 1	456,8	478,2	280,9	197,3	485	0,143	0,108	0,034	3,4	0,241
B70 Reference 2	474,3	496,6	291,8	204,8	502,9	0,140	0,109	0,031	3,1	0,220
B70 Reference 3	449,2	470,5	277,6	192,9	475,9	0,138	0,110	0,028	2,8	0,202
0,5% Steel 1	479,2	501,8	298,8	203	506,5	0,134	0,111	0,023	2,3	0,172
0,5% Steel 2	481,6	504,2	299,7	204,5	508,9	0,133	0,111	0,023	2,3	0,172
0,5% Steel 3	485,2	507,8	299	208,8	512,9	0,133	0,108	0,024	2,4	0,184
1,5% Steel 1	480,5	502,8	303,1	199,7	506,3	0,129	0,112	0,018	1,8	0,136
1,5% Steel 2	494,7	517,1	311,7	205,4	520,6	0,126	0,109	0,017	1,7	0,135
1,5% Steel 3	476,7	499,1	300,7	198,4	502,7	0,131	0,113	0,018	1,8	0,138
1,5% Polypropylene	447,8	471,1	274,7	196,4	476,7	0,147	0,119	0,029	2,9	0,194
1,5% Polypropylene	449,1	472	275,1	196,9	477,3	0,143	0,116	0,027	2,7	0,188
1,5% Polypropylene	469,1	491,8	288,2	203,6	497,2	0,138	0,111	0,027	2,7	0,192
1,5% Basalt 1	461,8	484,3	283,8	200,5	491,2	0,147	0,112	0,034	3,4	0,235
1,5% Basalt 2	456,3	480,6	277,8	202,8	488,3	0,158	0,120	0,038	3,8	0,241
1,5% Basalt 3	470	493,8	285,6	208,2	502	0,154	0,114	0,039	3,9	0,256
Notes: W=weight (g)										

Appendix H

Abrasion Rates at Various Distance Intervals

Table H.1 Abrasion rates at distance intervals

Specimen	Product Type	Effective sliding distance (km)	Sliding velocity (cm/s)	Abrasion rate* 0-1,25km	Abrasion rate* 1,25-2,5km	Abrasion rate* 2,5-3,75km	Abrasion rate* 3,75-5km	Total abrasion rate*
1.1	B70	2,5	16	0,000	-0,007			-0,003
1.2		2,5	16	0,009	0,001			0,005
2.1	Reference	2,5	25	0,011	0,010			0,011
2.2		5	25	-0,003	0,008	0,002	-0,001	0,002
11.1	0,5% steel fibers	2,5	16	0,008	-0,007			0,001
11.2		2,5	16	0,011	0,000			0,005
12.1		2,5	25	0,004	0,000			0,002
12.2		5	25	0,006	0,004	0,000	0,001	0,003
21.1	1.5% steel fibers	2,5	16	0,004	-0,008			-0,002
21.2		2,5	16	0,014	0,000			0,007
22.1		2,5	25	0,010	0,007			0,009
22.2		5	25	0,018	0,001	0,004	0,004	0,007
31.1	1.5% polypropyl. fibers	2,5	16	0,001	0,005			0,003
31.2		2,5	16	0,002	0,008			0,005
32.1		2,5	25	0,012	0,001			0,006
32.2		5	25	0,010	0,003	0,003	-0,001	0,004
41.1	1.5% basalt fibers	2,5	16	0,004	-0,008			-0,002
41.2		2,5	16	0,008	0,001			0,004
42.1		2,5	25	0,003	-0,015			-0,006
42.2		5	25	0,010	-0,002	0,002	0,001	0,003

*Abrasion rates in mm/km

Appendix I

3D Surface Plots Before Abrasion

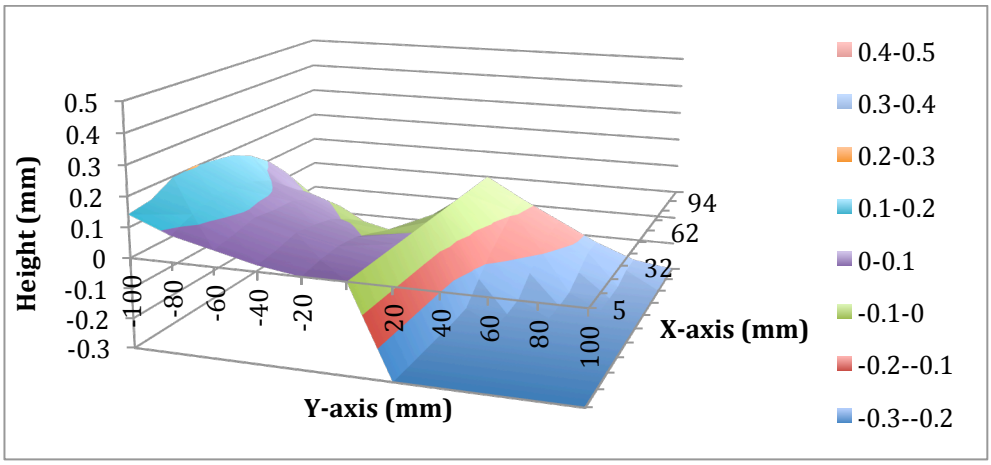

Figure I.1 3D surface plot of specimen 1.1 before abrasion

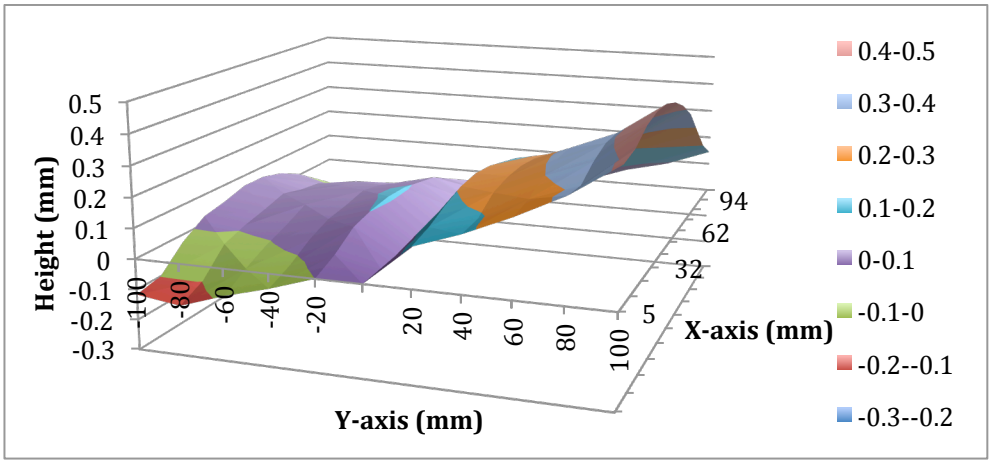

Figure I.2 3D surface plot of specimen 1.2 before abrasion

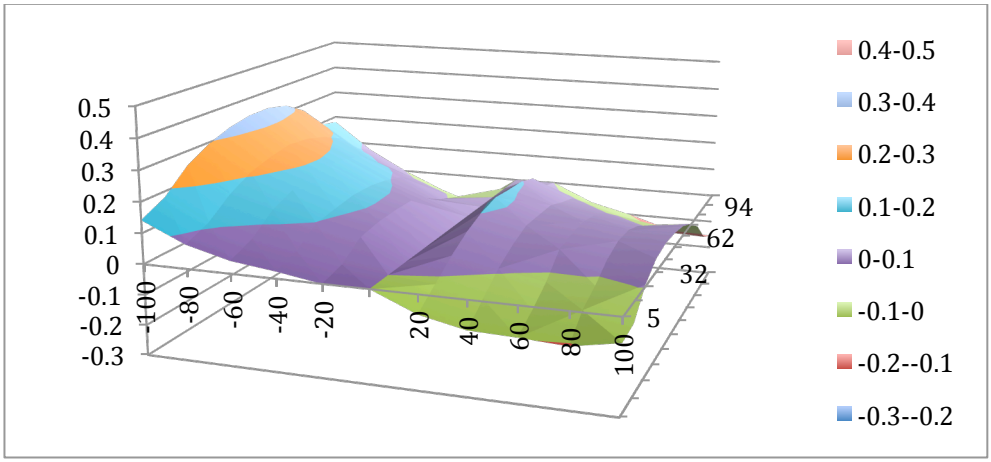

Figure I.3 3D surface plot of specimen 2.1 before abrasion

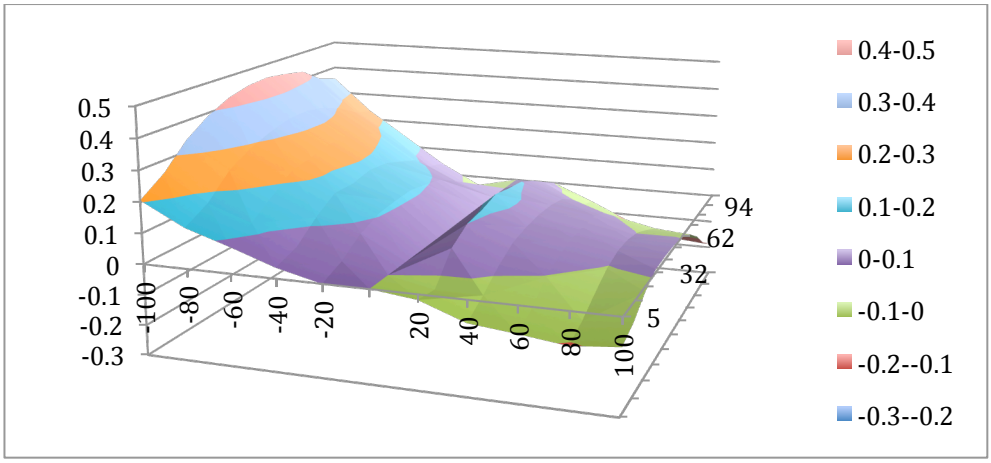

Figure I.4 3D surface plot of specimen 2.2 before abrasion

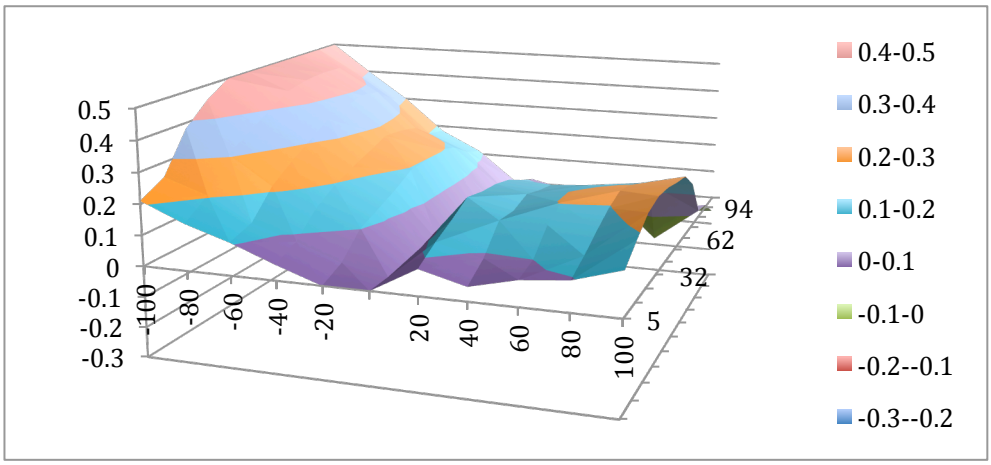

Figure I.5 3D surface plot of specimen 11.1 before abrasion

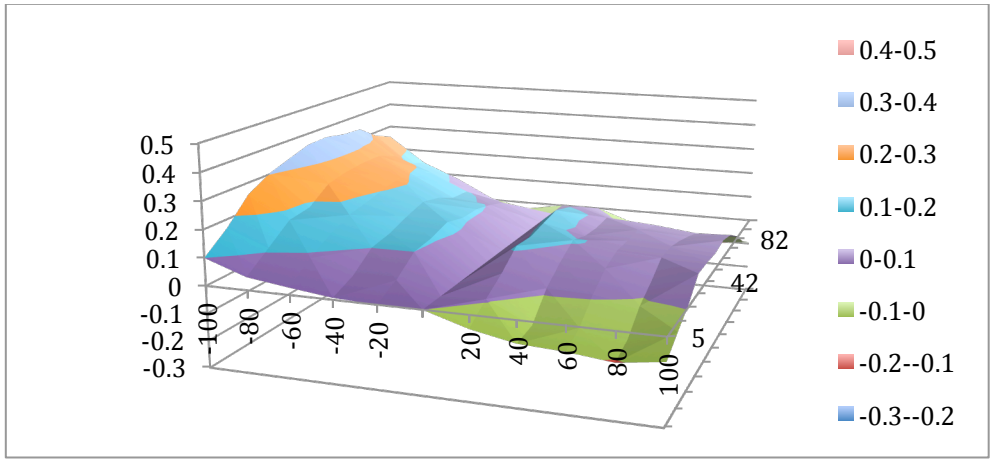

Figure I.6 3D surface plot of specimen 11.2 before abrasion

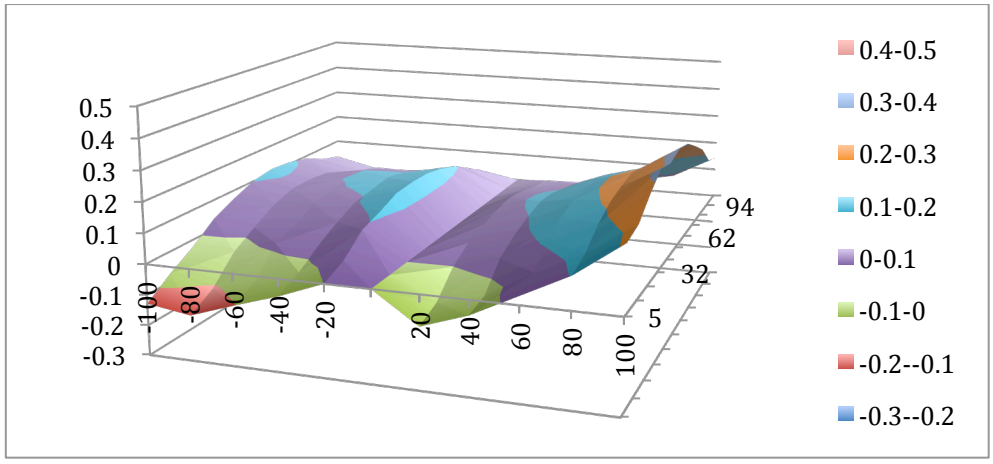

Figure I.7 3D surface plot of specimen 12.1 before abrasion

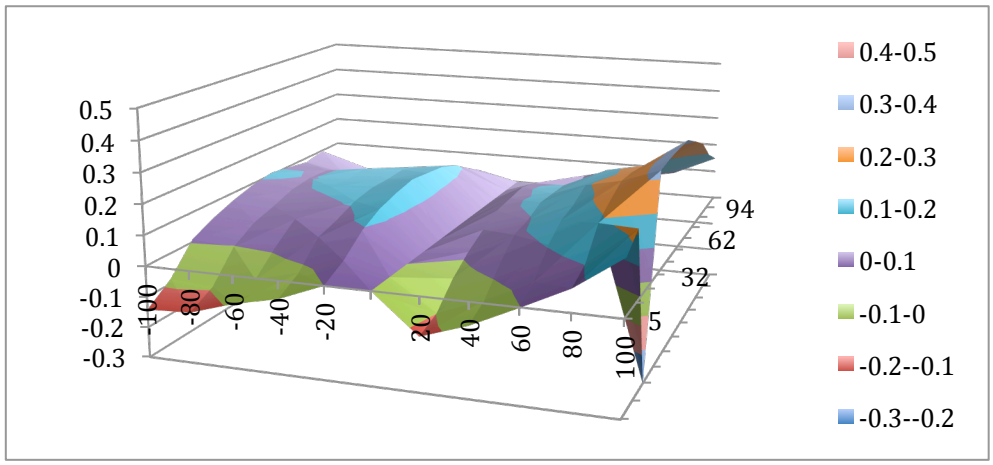

Figure I.8 3D surface plot of specimen 12.2 before abrasion

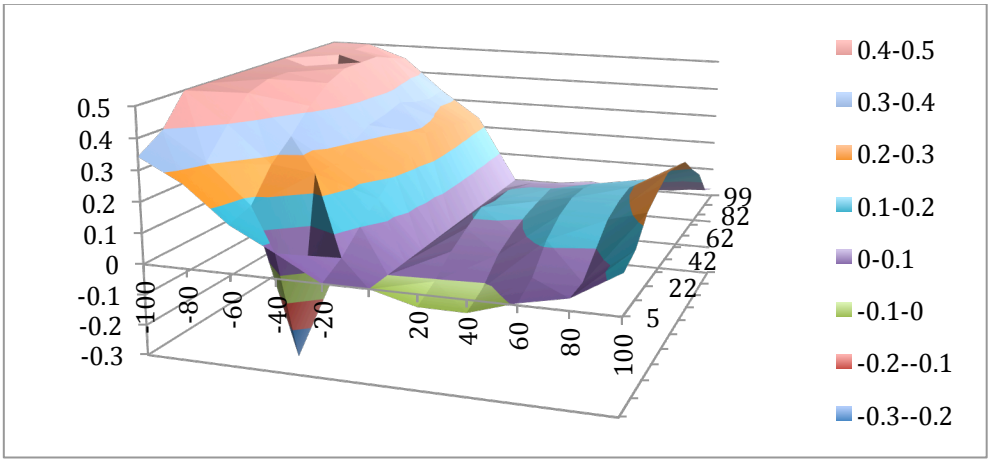

Figure I.9 3D surface plot of specimen 21.1 before abrasion

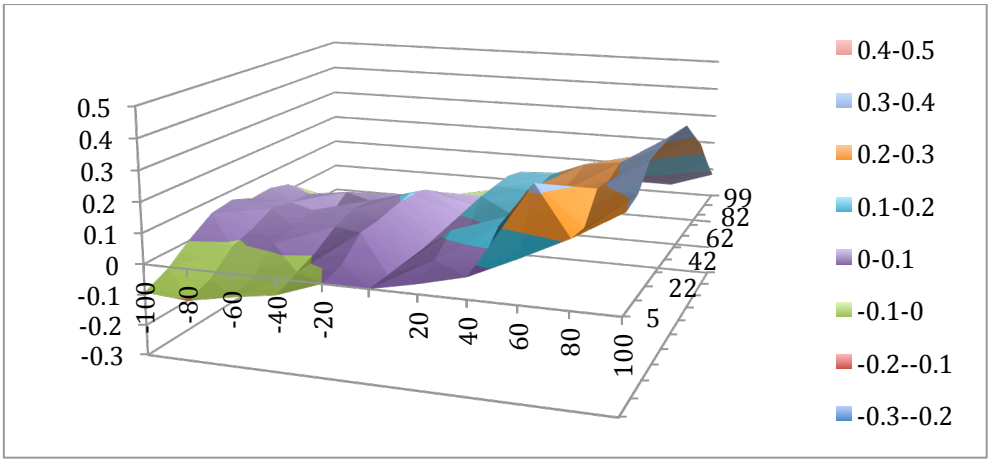

Figure I.10 3D surface plot of specimen 21.2 before abrasion

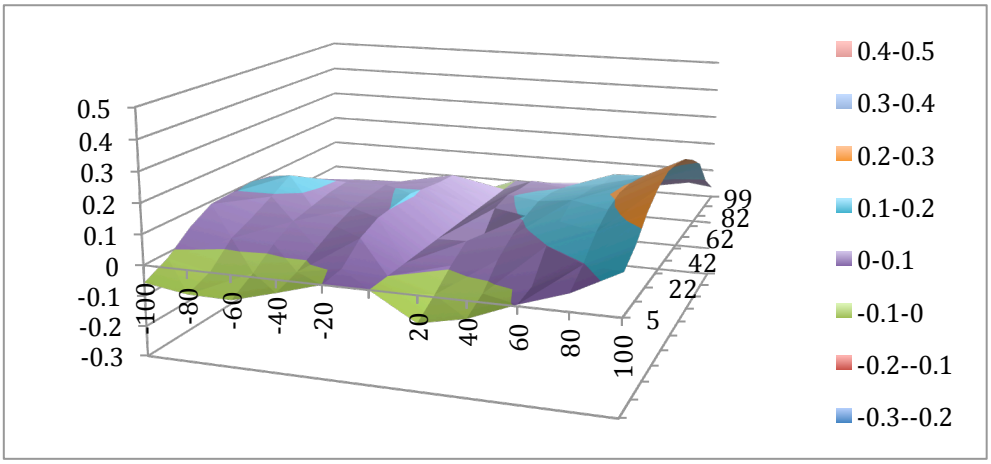

Figure I.11 3D surface plot of specimen 22.1 before abrasion

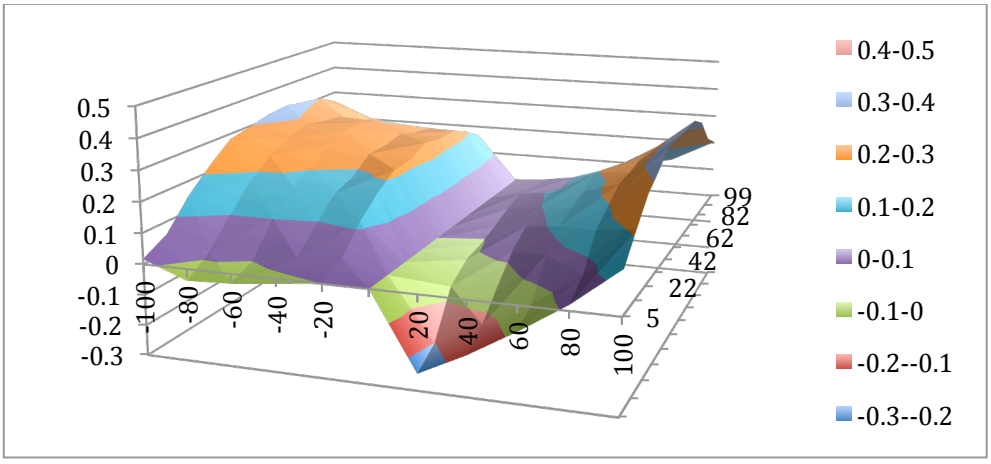

Figure I.12 3D surface plot of specimen 22.2 before abrasion

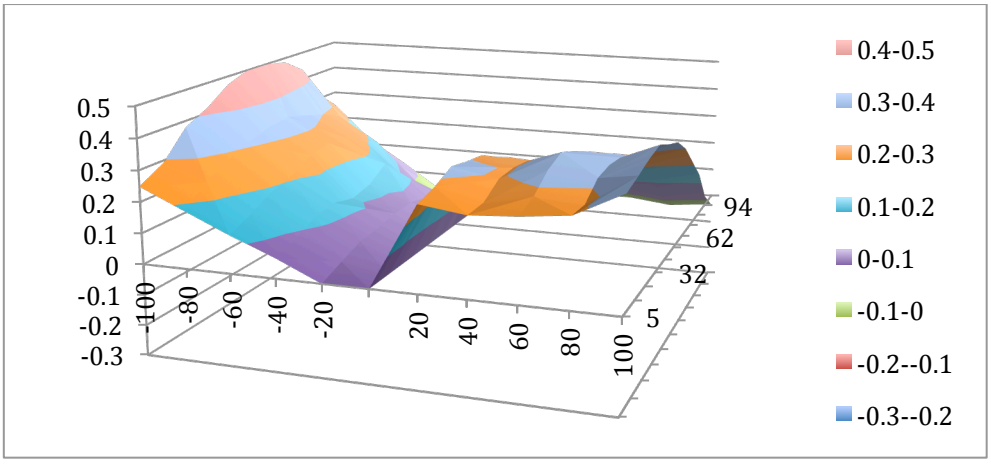

Figure I.13 3D surface plot of specimen 31.1 before abrasion

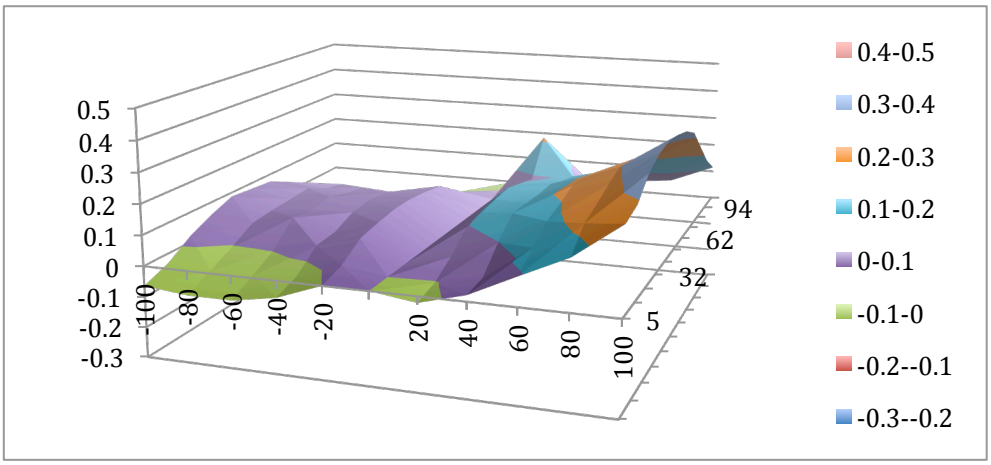

Figure I.14 3D surface plot of specimen 31.2 before abrasion

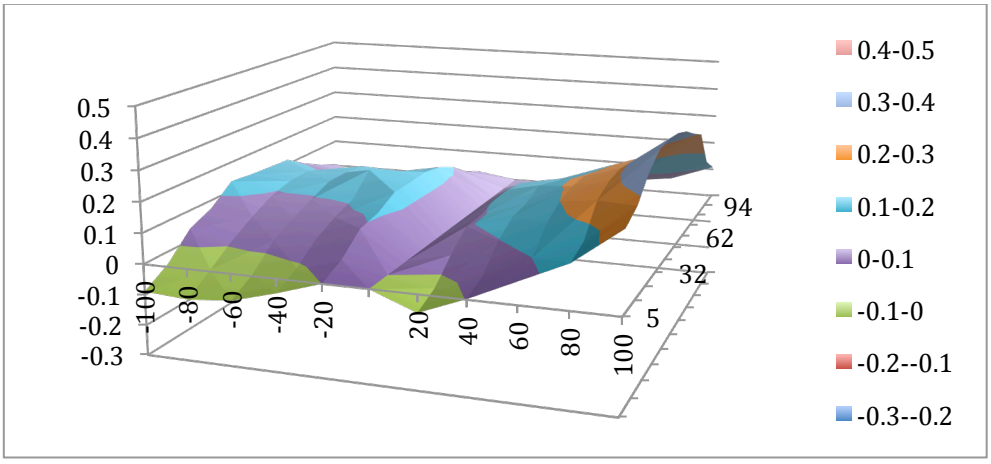

Figure I.15 3D surface plot of specimen 32.1 before abrasion

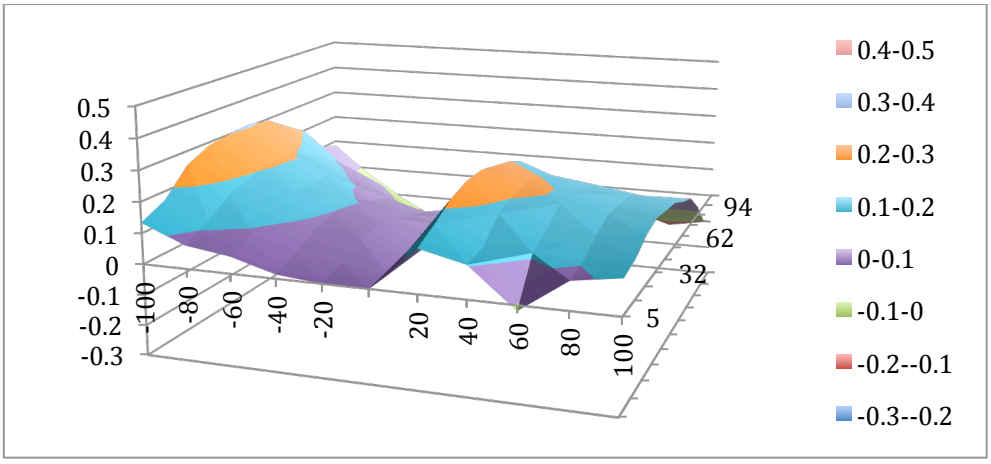

Figure I.16 3D surface plot of specimen 32.2 before abrasion

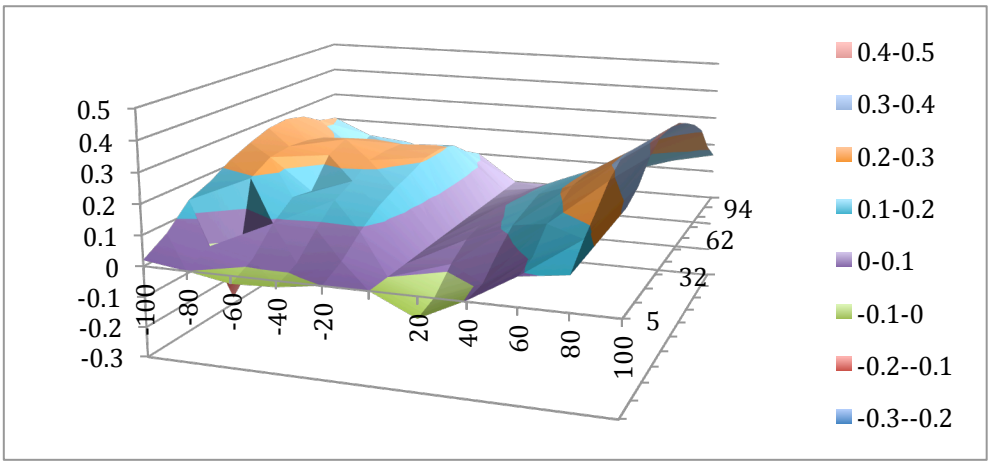

Figure I.17 3D surface plot of specimen 41.1 before abrasion

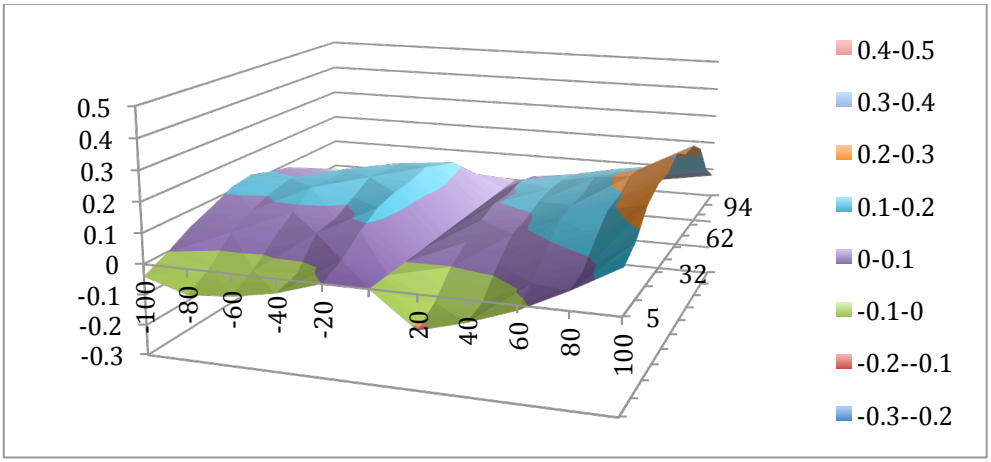

Figure I.18 3D surface plot of specimen 41.2 before abrasion

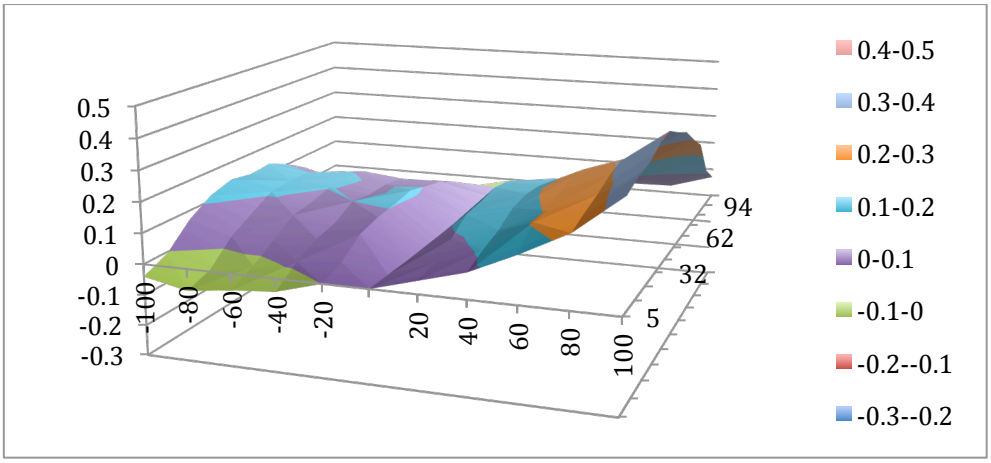

Figure I.19 3D surface plot of specimen 42.1 before abrasion

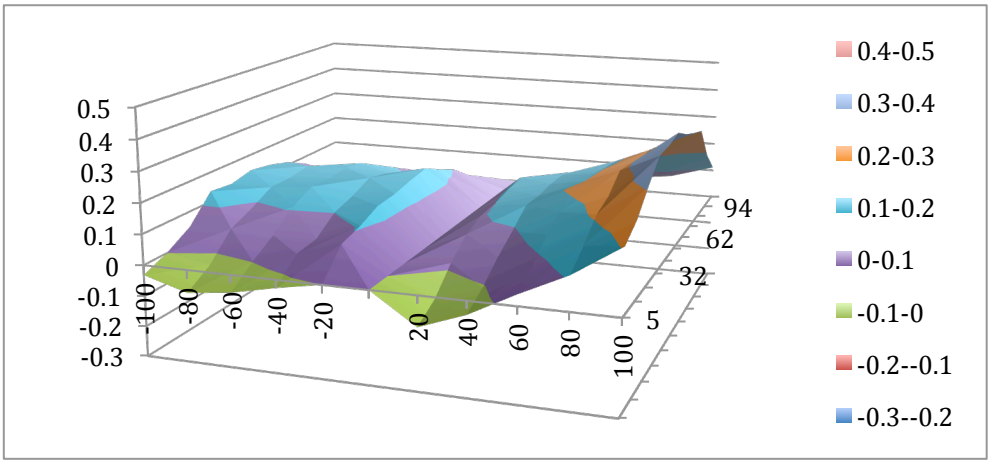

Figure I.20 3D surface plot of specimen 42.2 before abrasion

Appendix J

Wear Profiles Along X-axis

Method 1

Method 2

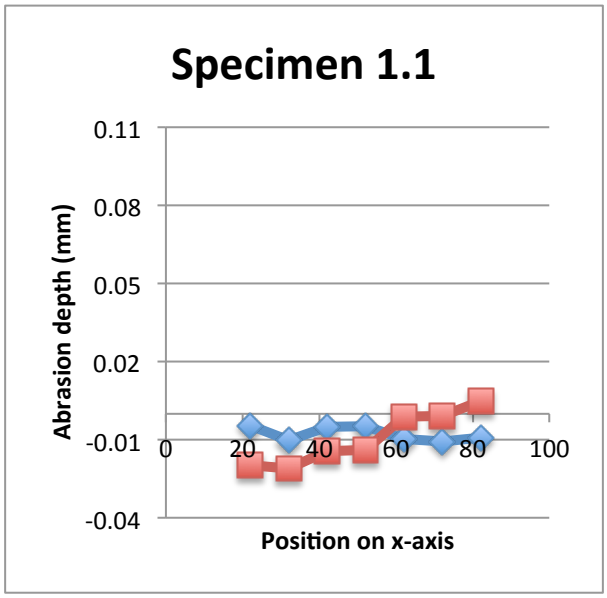

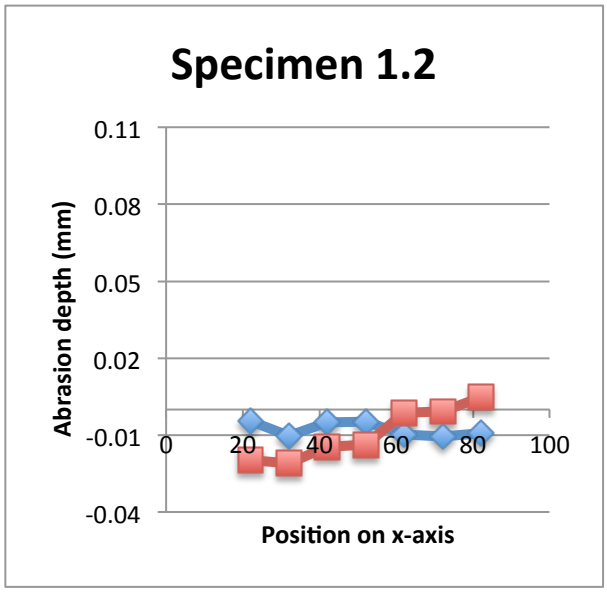

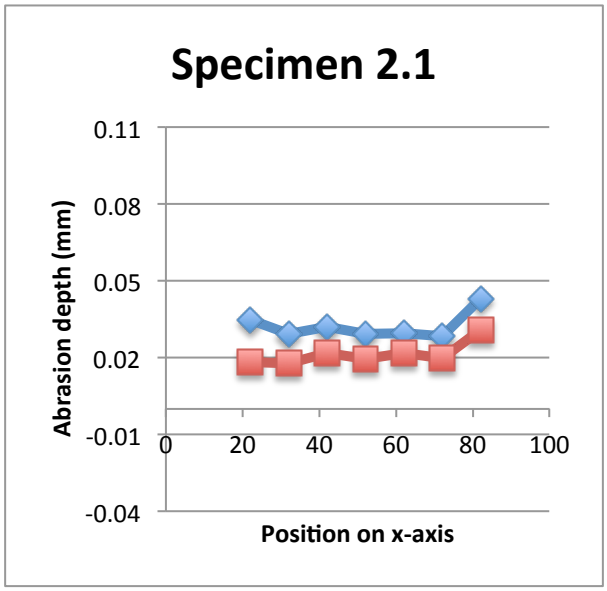

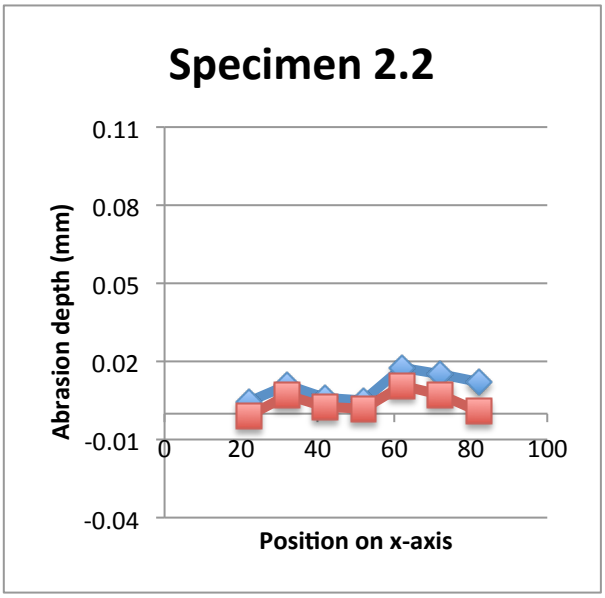

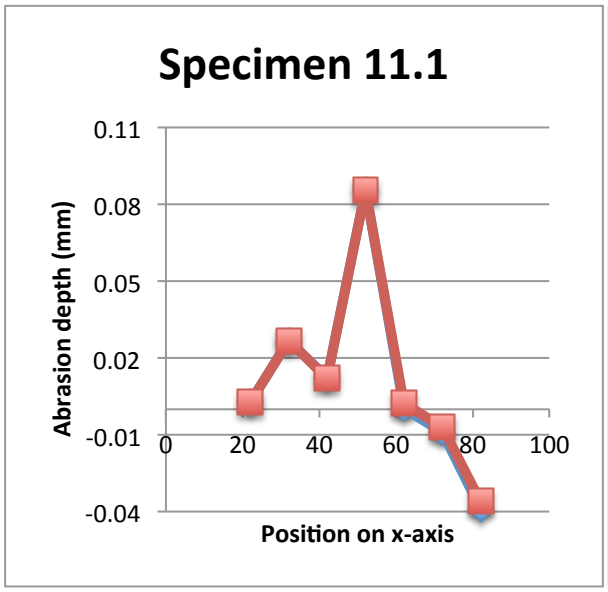
Specimen 11.1
Abrasion depth (mm)
0.11
0.08
0.05
0.02
-0.01
-0.04
0
20
40
60
80
100
Position on x-axis

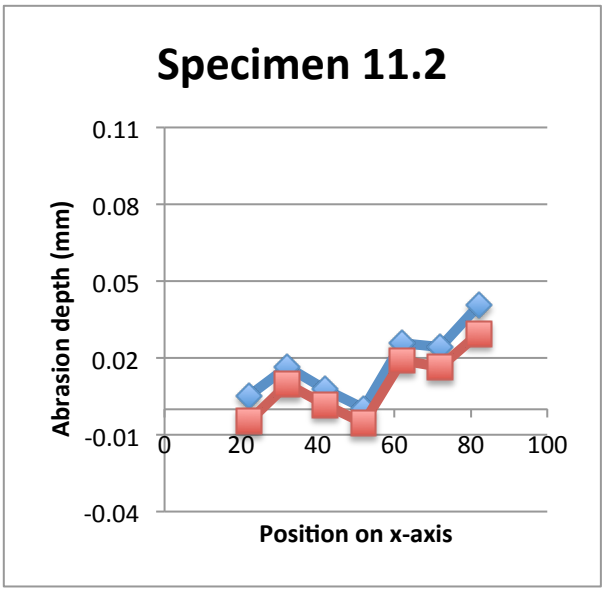
Specimen 11.2
Abrasion depth (mm)
0.11
0.08
0.05
0.02
-0.01
-0.04
0
20
40
60
80
100
Position on x-axis

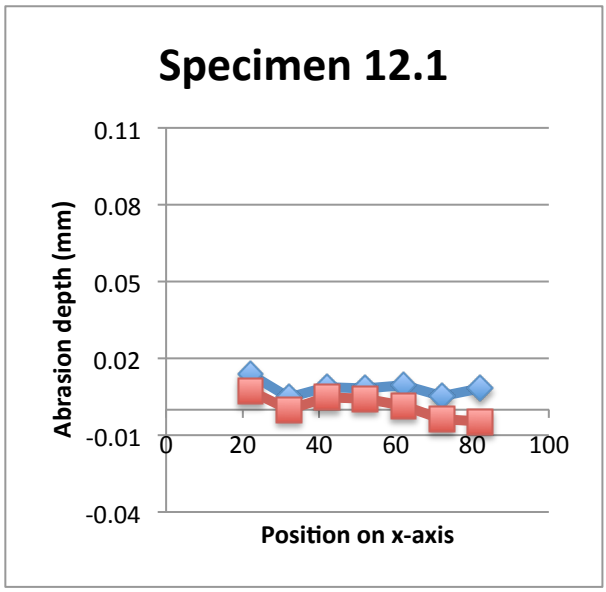
Specimen 12.1
Abrasion depth (mm)
0.11
0.08
0.05
0.02
-0.01
-0.04
0
20
40
60
80
100
Position on x-axis

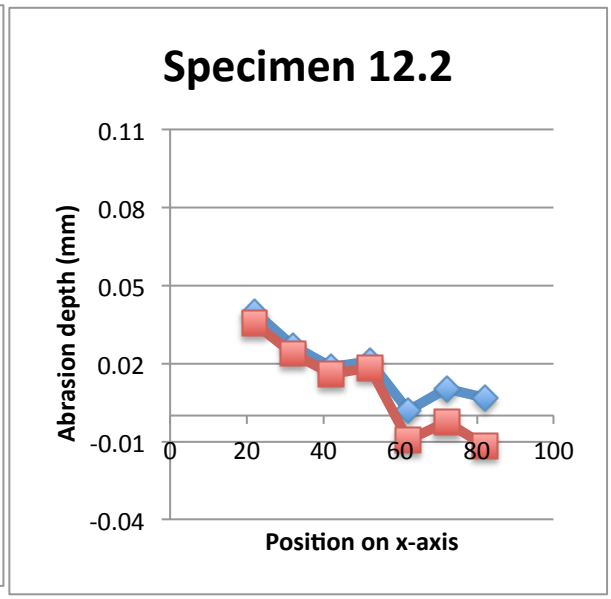
Specimen 12.2
Abrasion depth (mm)
0.11
0.08
0.05
0.02
-0.01
-0.04
0
20
40
60
80
100
Position on x-axis

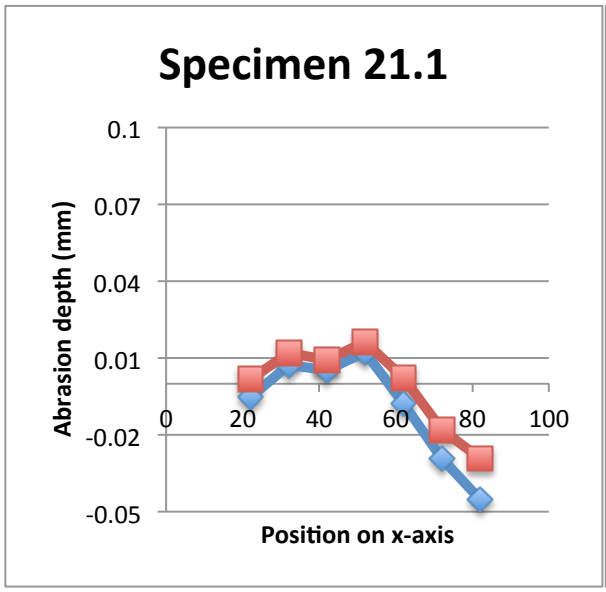
Specimen 21.1
Abrasion depth (mm)
0.1
0.07
0.04
0.01
-0.02
-0.05
0
20
40
60
80
100
Position on x-axis

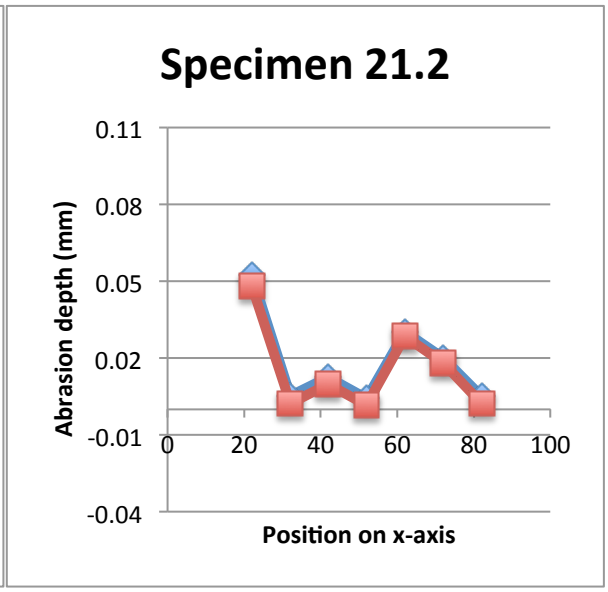
Specimen 21.2
Abrasion depth (mm)
0.11
0.08
0.05
0.02
-0.01
-0.04
0
20
40
60
80
100
Position on x-axis

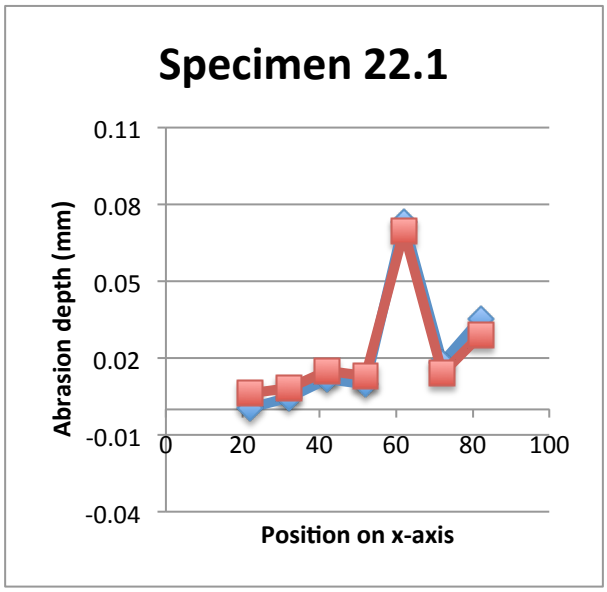
Specimen 22.1
Abrasion depth (mm)
0.11
0.08
0.05
0.02
-0.01
-0.04
0
20
40
60
80
100
Position on x-axis

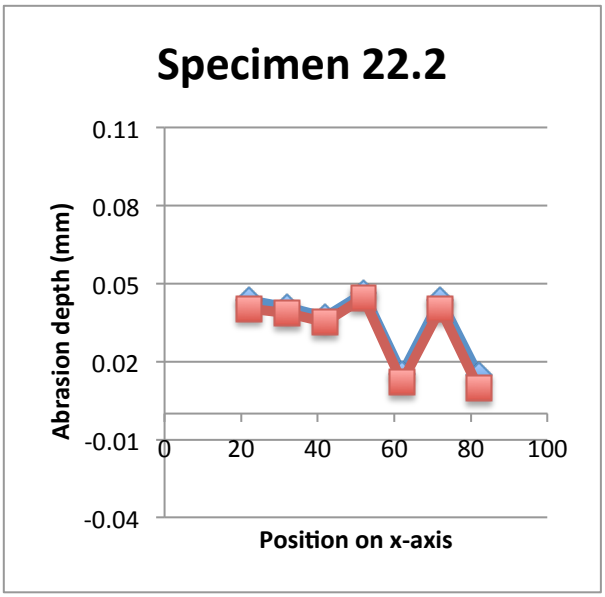
Specimen 22.2
Abrasion depth (mm)
0.11
0.08
0.05
0.02
-0.01
-0.04
0
20
40
60
80
100
Position on x-axis

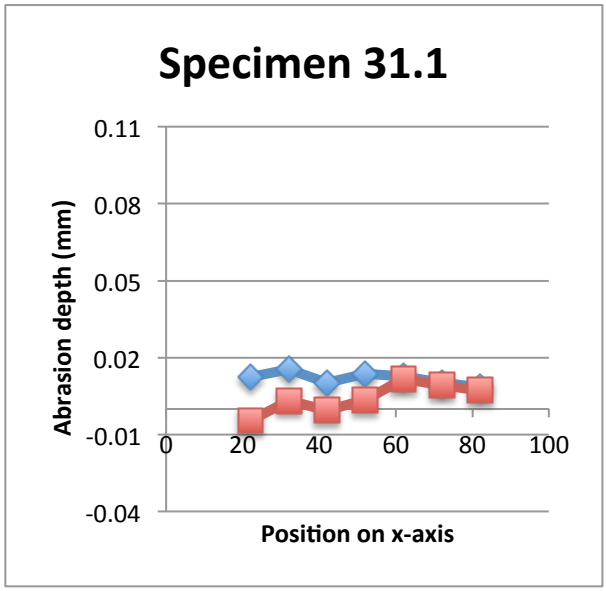
Specimen 31.1
Abrasion depth (mm)
0.11
0.08
0.05
0.02
-0.01
-0.04
0
20
40
60
80
100
Position on x-axis

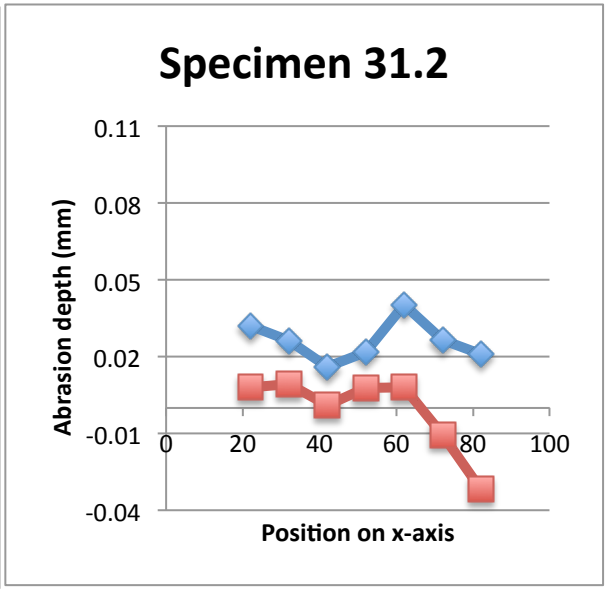
Specimen 31.2
Abrasion depth (mm)
0.11
0.08
0.05
0.02
-0.01
-0.04
0
20
40
60
80
100
Position on x-axis

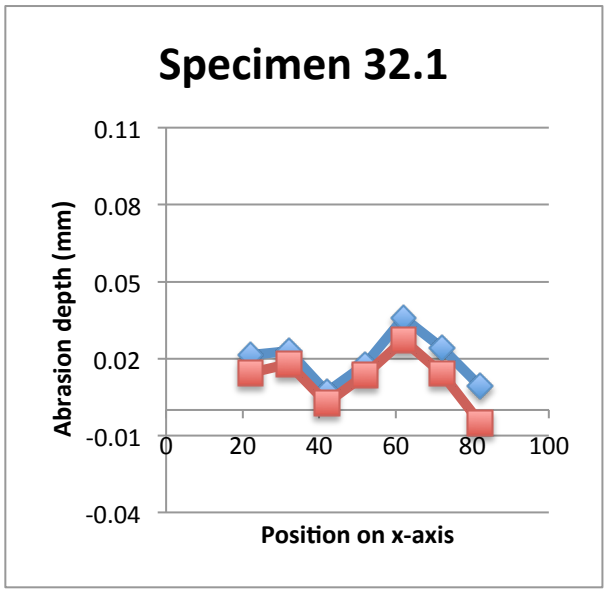
Specimen 32.1
Abrasion depth (mm)
0.11
0.08
0.05
0.02
-0.01
-0.04
0
20
40
60
80
100
Position on x-axis

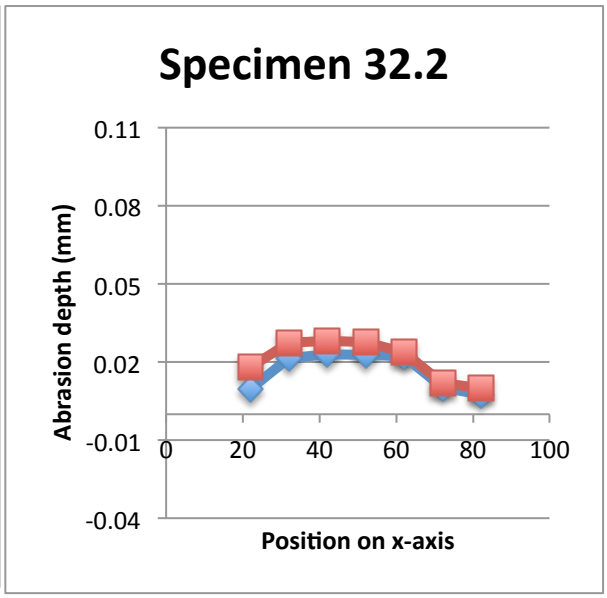
Specimen 32.2
Abrasion depth (mm)
0.11
0.08
0.05
0.02
-0.01
-0.04
0
20
40
60
80
100
Position on x-axis

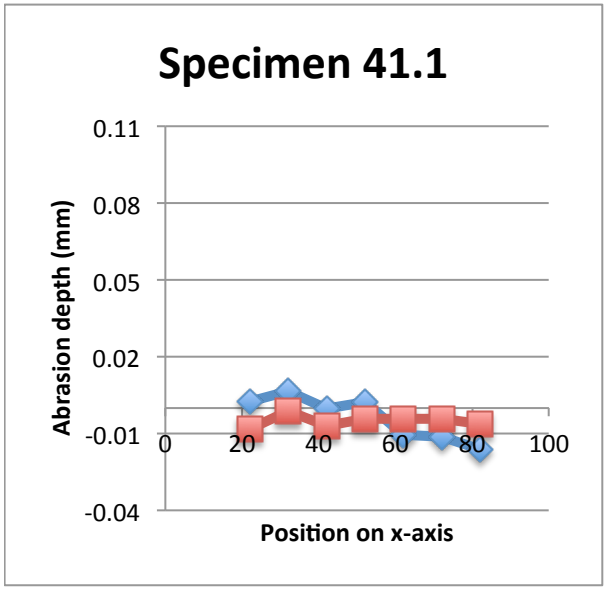

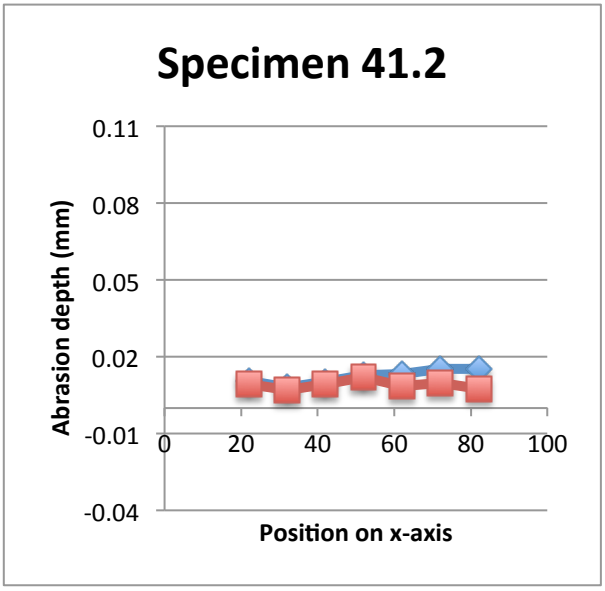

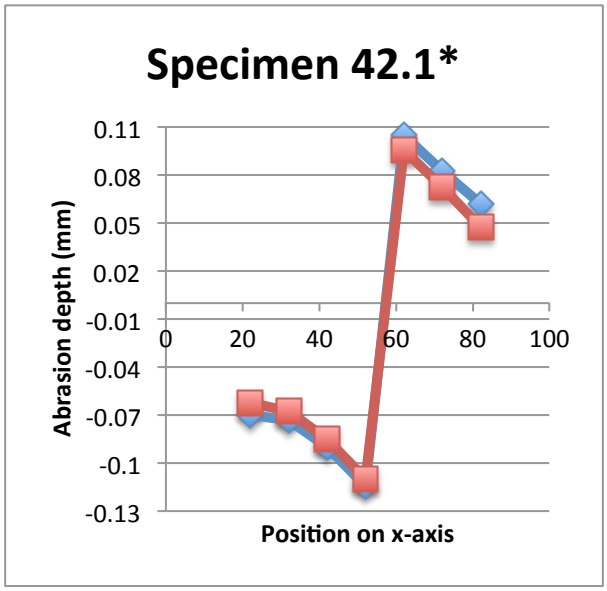

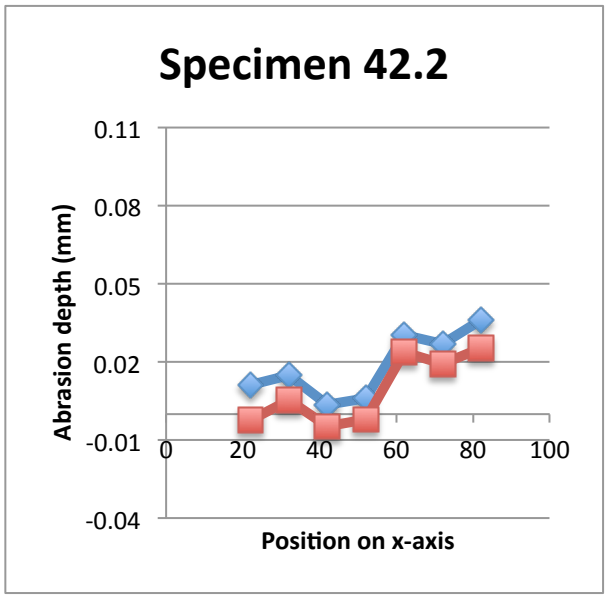

*Different scale on the y-axis than the rest

Appendix K

Abrasion Rates Along X-axis – Average of Method 1 and 2

Table K.1 Abrasion rates along x-axis

Abrasion Rate (mm/km) Along the X-axis								
Product Type	B70 Reference				0,5% Steel Fiber			
Specimen	1.1	1.2	2.1	2.2	11.1	11.2	12.1	12.2
Contact Pressure (MPa)	1	1	1	1	1	1	1	1
Sliding Velocity (cm/s)	16	16	25	25	16	16	25	25
Y=-100	0,011	0,007	0,010	0,001	0,000	0,000	-0,002	-0,001
Y=-80	0,006	0,008	0,008	0,002	-0,005	0,009	0,002	0,003
Y=-60	0,004	0,005	0,012	0,001	0,001	0,002	0,005	0,003
Y=-40	0,009	0,004	0,008	0,001	0,001	0,006	0,003	0,004
Y=-20	0,009	0,005	0,006	0,002	0,003	0,007	0,004	0,002
Y=20	-0,013	0,003	0,011	0,000	0,001	0,004	0,000	0,004
Y=40	-0,012	0,005	0,007	0,001	0,018	0,009	0,001	0,000
Y=60	-0,014	0,004	0,013	0,002	0,001	0,007	-0,001	0,003
Y=80	-0,016	0,004	0,016	0,003	-0,008	0,009	0,003	0,003
Y=100	-0,018	0,004	0,017	0,002	-0,003	0,001	0,004	0,007
Average	-0,004	0,005	0,011	0,002	0,001	0,006	0,002	0,003

Table K.2 Abrasion rates along x-axis

Abrasion Rate (mm/km) Along the X-axis								
Product Type	1,5% Steel Fiber				1,5% Polypropylene Fiber			
Specimen	21.1	21.2	22.1	22.2	31.1	31.2	32.1	32.2
Contact Pressure(MPa)	1	1	1	1	1	1	1	1
Sliding Velocity (cm/s)	16	16	25	25	16	16	25	25
Y=-100	0,006	0,009	-0,009	0,006	0,018	0,002	0,009	0,002
Y=-80	-0,030	0,001	0,014	0,007	0,005	0,005	0,004	0,002
Y=-60	0,005	0,007	0,016	0,008	0,007	0,002	0,013	0,004
Y=-40	-0,001	0,002	0,003	0,012	-0,004	0,002	0,003	0,003
Y=-20	-0,006	0,009	0,018	0,005	-0,003	0,006	0,003	0,005
Y=20	-0,006	0,007	0,004	0,007	-0,003	0,001	0,005	0,003
Y=40	0,003	-0,001	0,010	0,005	-0,003	0,016	0,007	0,004
Y=60	-0,002	0,016	0,021	0,006	0,005	0,005	0,013	0,003
Y=80	0,004	0,010	0,005	0,005	0,002	0,006	0,006	0,008
Y=100	0,008	0,009	0,004	0,006	0,008	0,004	0,000	0,002
Average	-0,002	0,007	0,009	0,007	0,004	0,006	0,007	0,004

Table K.3 Abrasion rates along x-axis

Abrasion Rate (mm/km) Along the X-axis				
Product Type	1,5% Basalt Fiber			
Specimen	41.1	41.2	42.1	42.2
Contact Pressure (MPa)	1	1	1	1
Sliding Velocity (cm/s)	16	16	25	25
Y=-100	-0,012	-0,001	-0,001	0,002
Y=-80	0,000	0,002	-0,001	0,002
Y=-60	-0,009	0,002	-0,007	0,004
Y=-40	0,007	0,006	-0,004	0,002
Y=-20	-0,003	0,002	-0,002	0,000
Y=20	0,002	0,005	-0,009	0,004
Y=40	0,001	0,007	-0,008	0,003
Y=60	-0,002	0,008	-0,011	0,003
Y=80	0,009	0,004	-0,007	0,003
Y=100	-0,009	0,007	-0,009	0,004
Average	-0,002	0,005	-0,006	0,003

Appendix L

Wear Profiles Along Y-axis

Method 1

Method 2

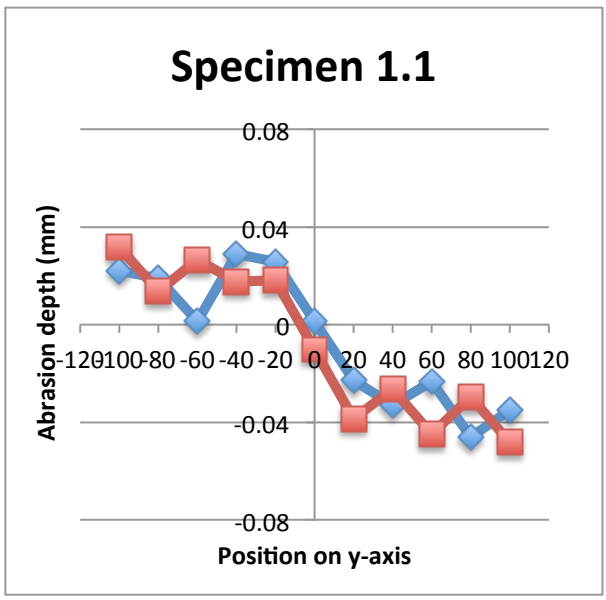

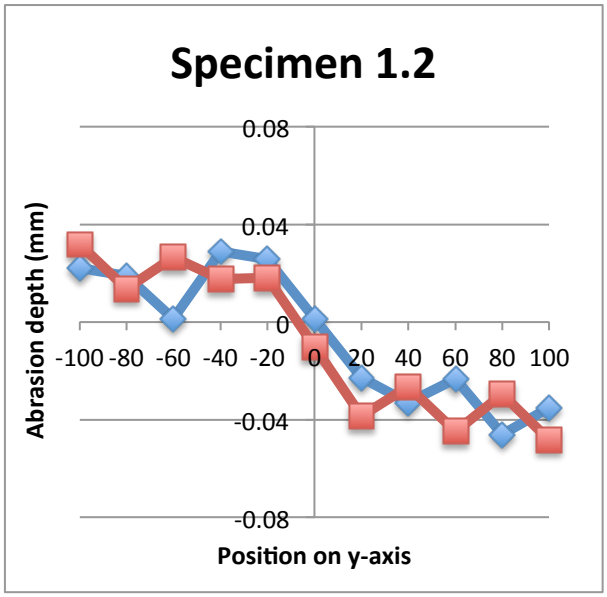

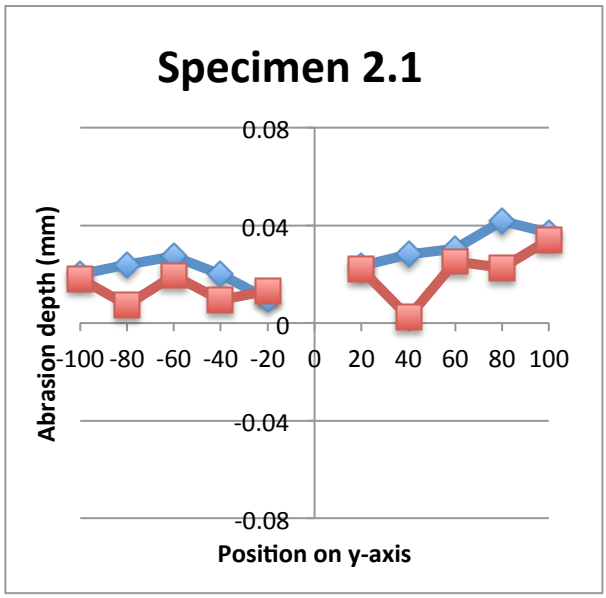

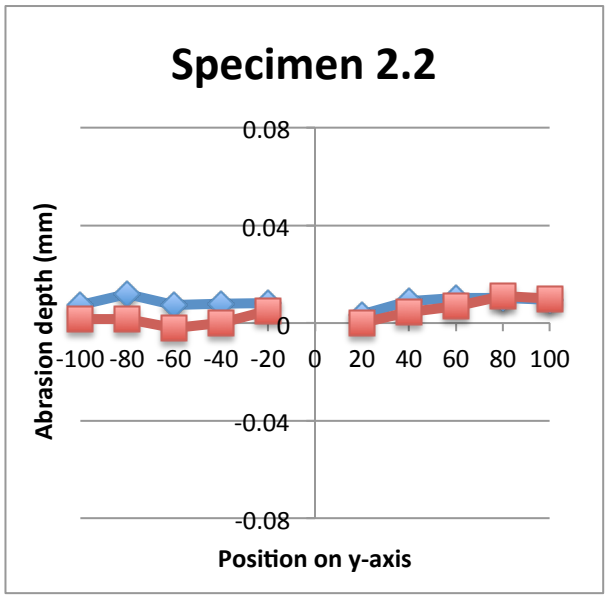

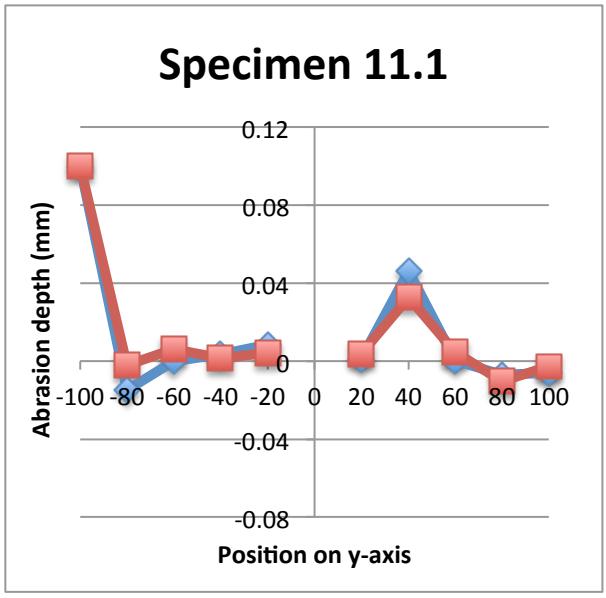
Specimen 11.1
0.12
0.08
0.04
0
-0.04
-0.08
-100 -80 -60 -40 -20 0 20 40 60 80 100
Abrasion depth (mm)
Position on y-axis

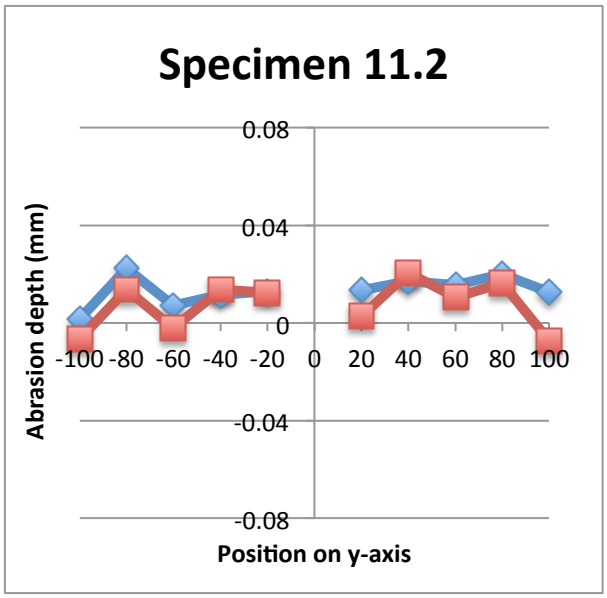
Specimen 11.2
0.08
0.04
0
-0.04
-0.08
-100 -80 -60 -40 -20 0 20 40 60 80 100
Abrasion depth (mm)
Position on y-axis

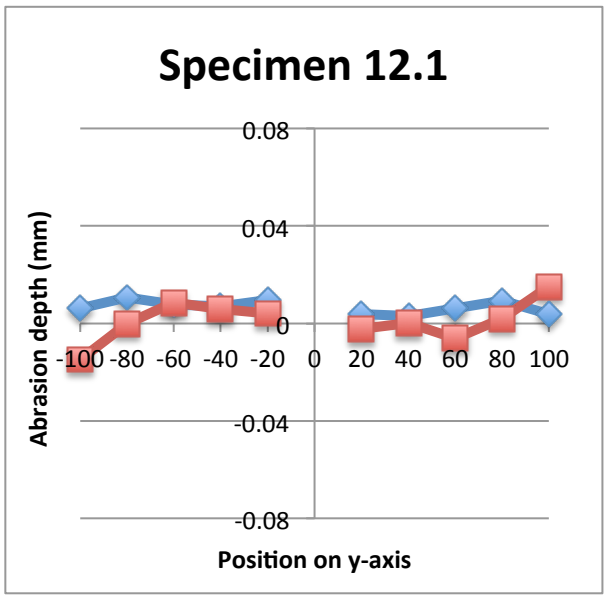
Specimen 12.1
0.08
0.04
0
-0.04
-0.08
-100 -80 -60 -40 -20 0 20 40 60 80 100
Abrasion depth (mm)
Position on y-axis

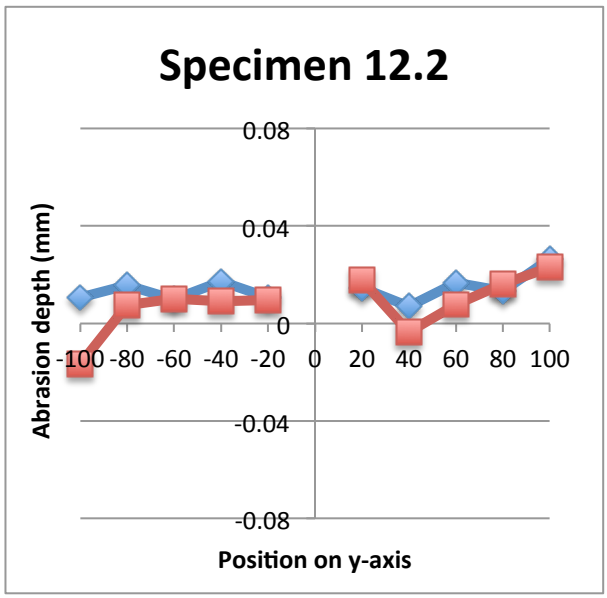
Specimen 12.2
0.08
0.04
0
-0.04
-0.08
-100 -80 -60 -40 -20 0 20 40 60 80 100
Abrasion depth (mm)
Position on y-axis

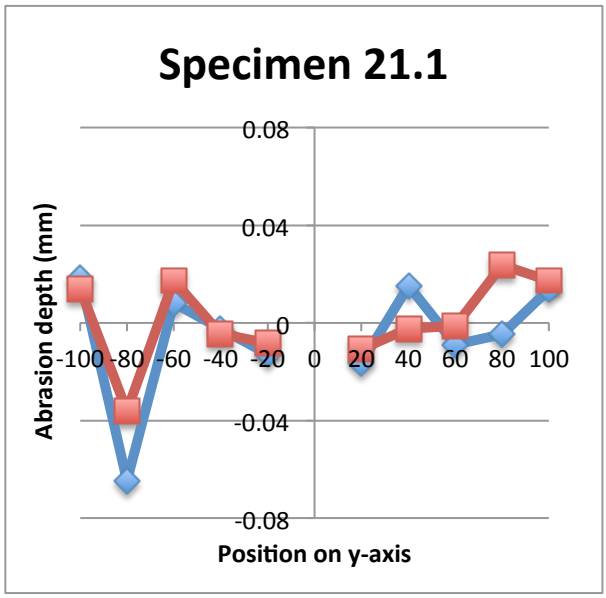
Specimen 21.1
0.08
0.04
0
-0.04
-0.08
-100 -80 -60 -40 -20 0 20 40 60 80 100
Abrasion depth (mm)
Position on y-axis

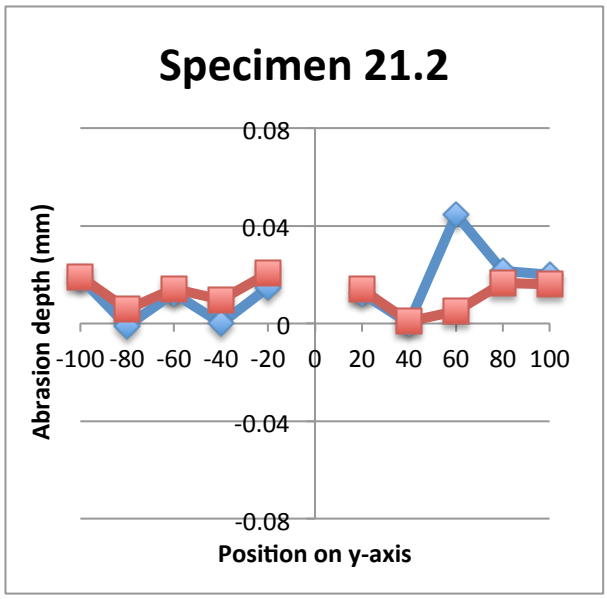
Specimen 21.2
0.08
0.04
0
-0.04
-0.08
-100 -80 -60 -40 -20 0 20 40 60 80 100
Abrasion depth (mm)
Position on y-axis

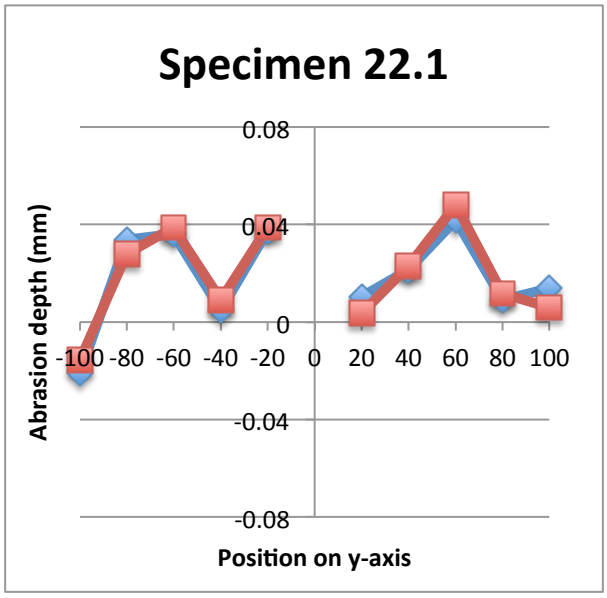
Specimen 22.1
Abrasion depth (mm)
0.08
0.04
0
-0.04
-0.08
-100 -80 -60 -40 -20 0 20 40 60 80 100
Position on y-axis

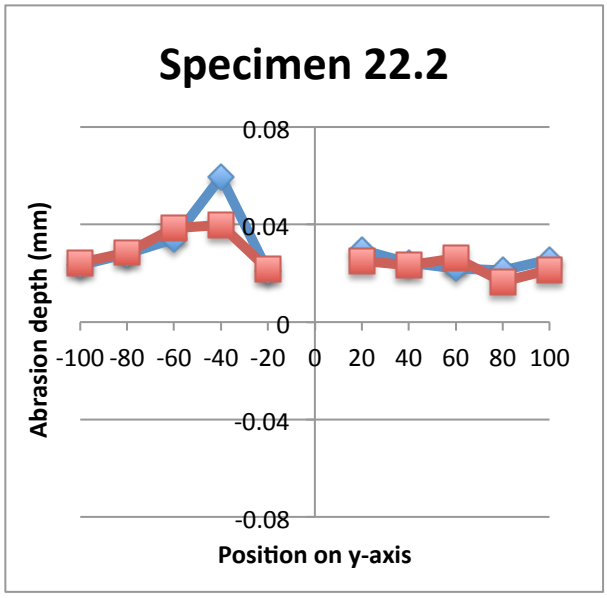
Specimen 22.2
Abrasion depth (mm)
0.08
0.04
0
-0.04
-0.08
-100 -80 -60 -40 -20 0 20 40 60 80 100
Position on y-axis

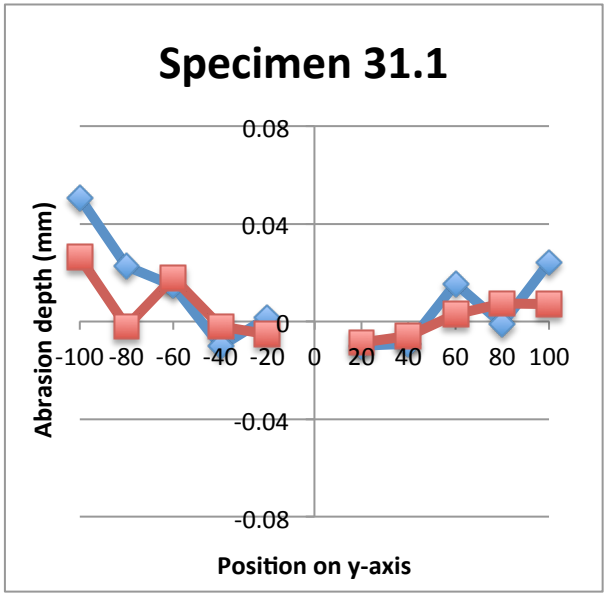
Specimen 31.1
Abrasion depth (mm)
0.08
0.04
0
-0.04
-0.08
-100 -80 -60 -40 -20 0 20 40 60 80 100
Position on y-axis

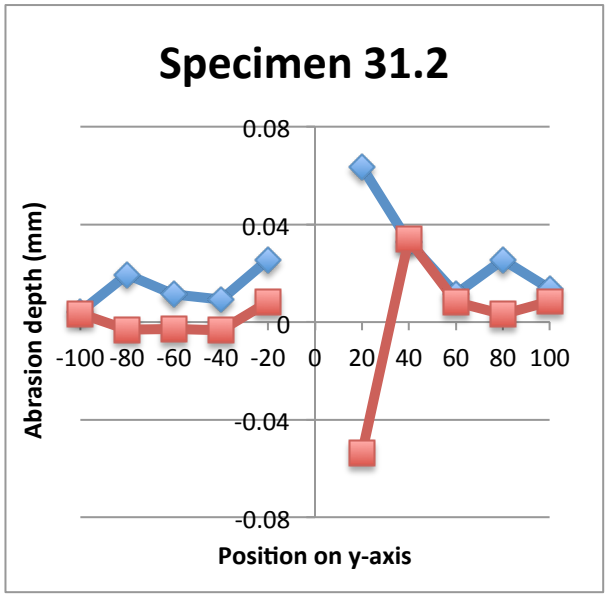
Specimen 31.2
Abrasion depth (mm)
0.08
0.04
0
-0.04
-0.08
-100 -80 -60 -40 -20 0 20 40 60 80 100
Position on y-axis

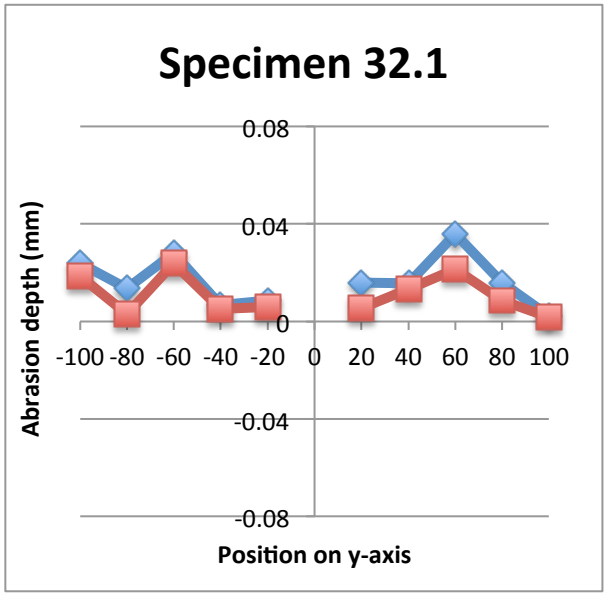
Specimen 32.1
Abrasion depth (mm)
0.08
0.04
0
-0.04
-0.08
-100 -80 -60 -40 -20 0 20 40 60 80 100
Position on y-axis

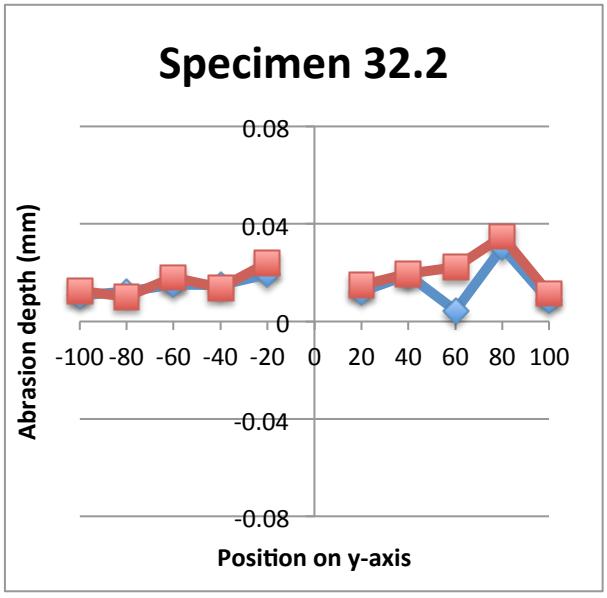
Specimen 32.2
Abrasion depth (mm)
0.08
0.04
0
-0.04
-0.08
-100 -80 -60 -40 -20 0 20 40 60 80 100
Position on y-axis

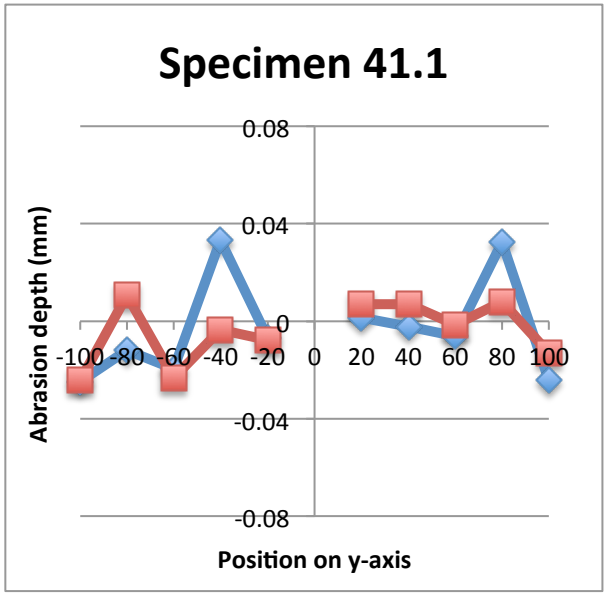
Specimen 41.1
Abrasion depth (mm)
0.08
0.04
0
-0.04
-0.08
-100 -80 -60 -40 -20 0 20 40 60 80 100
Position on y-axis

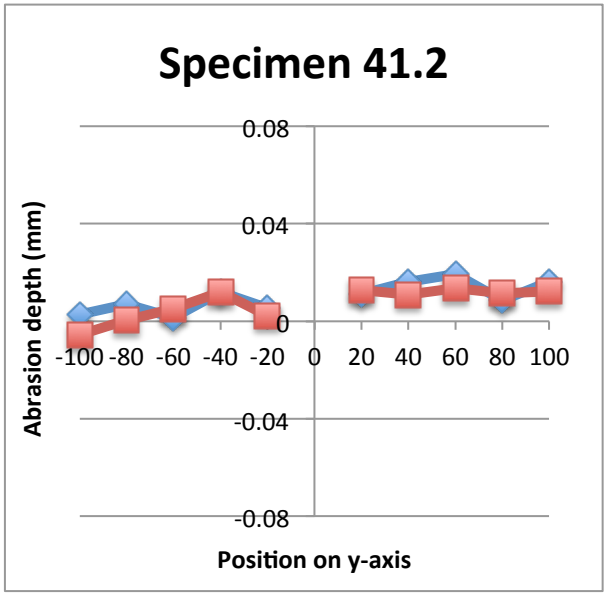
Specimen 41.2
Abrasion depth (mm)
0.08
0.04
0
-0.04
-0.08
-100 -80 -60 -40 -20 0 20 40 60 80 100
Position on y-axis

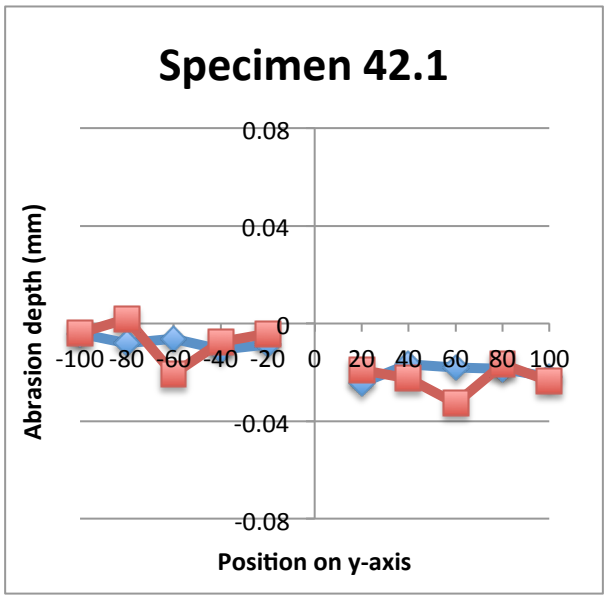
Specimen 42.1
Abrasion depth (mm)
0.08
0.04
0
-0.04
-0.08
-100 -80 -60 -40 -20 0 20 40 60 80 100
Position on y-axis

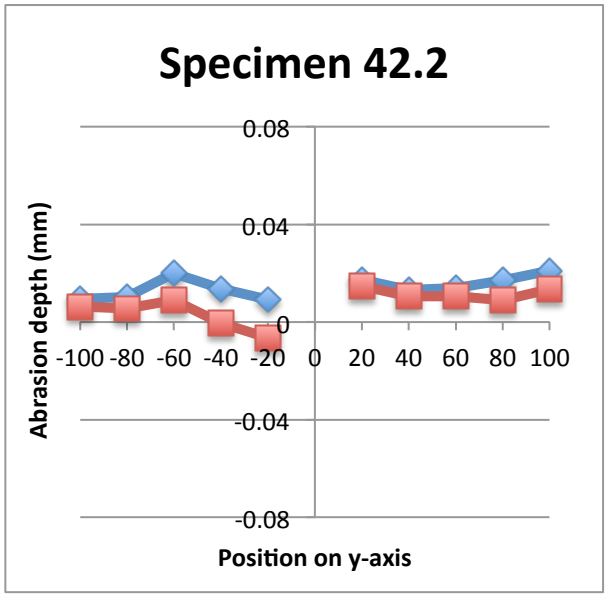
Specimen 42.2
Abrasion depth (mm)
0.08
0.04
0
-0.04
-0.08
-100 -80 -60 -40 -20 0 20 40 60 80 100
Position on y-axis

Appendix M

Abrasion Rates Along Y-axis - Average of Method 1 and 2

Table M.1 Abrasion rates along y-axis

Abrasion Rate (mm/km) Along the Y-axis								
Product Type	B70 Reference				0,5% Steel Fiber			
Specimen	1.1	1.2	2.1	2.2	11.1	11.2	12.1	12.2
Contact Pressure(MPa)	1	1	1	1	1	1	1	1
Sliding Velocity (cm/s)	16	16	25	25	16	16	25	25
X=22	-0,005	0,006	0,011	0,000	0,001	0,000	0,004	0,007
X=32	-0,006	0,003	0,009	0,002	0,011	0,005	0,001	0,005
X=42	-0,004	0,001	0,011	0,001	0,005	0,002	0,003	0,004
X=52	-0,004	0,002	0,010	0,001	0,007	-0,001	0,003	0,004
X=62	-0,002	0,009	0,010	0,003	0,001	0,009	0,002	-0,001
X=72	-0,002	0,008	0,010	0,002	-0,003	0,008	0,000	0,001
X=82	-0,001	0,006	0,015	0,001	-0,015	0,014	0,001	-0,001
Average	-0,004	0,005	0,011	0,002	0,001	0,006	0,002	0,003

Table M.2 Abrasion rates along y-axis

Abrasion Rate (mm/km) Along the Y-axis								
Product Type	1,5% Steel Fiber				1,5% Polypropylene Fiber			
Specimen	21.1	21.2	22.1	22.2	31.1	31.2	32.1	32.2
Contact Pressure (MPa)	1	1	1	1	1	1	1	1
Sliding Velocity (cm/s)	16	16	25	25	16	16	25	25
X=22	-0,001	0,020	0,001	0,008	0,002	0,008	0,007	0,003
X=32	0,004	0,002	0,003	0,008	0,004	0,007	0,008	0,005
X=42	0,003	0,004	0,005	0,007	0,002	0,003	0,002	0,005
X=52	0,006	0,001	0,005	0,009	0,003	0,006	0,006	0,005
X=62	-0,001	0,012	0,029	0,003	0,005	0,010	0,013	0,005
X=72	-0,009	0,008	0,007	0,008	0,004	0,003	0,008	0,002
X=82	-0,015	0,001	0,013	0,002	0,003	-0,002	0,001	0,002
Average	-0,002	0,007	0,009	0,007	0,004	0,006	0,007	0,004

Table M.3 Abrasion rates along y-axis

Abrasion Rate (mm/km) Along the Y-axis				
Product Type	1,5% Basalt Fiber			
Specimen	41.1	41.2	42.1	42.2
Contact Pressure (MPa)	1	1	1	1
Sliding Velocity (cm/s)	16	16	25	25
X=22	-0,001	0,004	-0,027	0,001
X=32	0,001	0,003	-0,028	0,002
X=42	-0,001	0,004	-0,035	0,000
X=52	0,000	0,005	-0,045	0,000
X=62	-0,003	0,004	0,040	0,005
X=72	-0,003	0,005	0,031	0,005
X=82	-0,004	0,005	0,022	0,006
Average	-0,002	0,005	-0,006	0,003